AN ABSTRACT OF THE DISSERTATION OF

Catherine Finkenbiner for the degree of Doctor of Philosophy in Water Resources Science presented on November 30, 2021.

Title: Advancing the Understanding and Representation of Ecohydrological Processes using Tracer-enabled Modeling Approaches

Abstract approved: _____

Stephen P. Good

Climate change impacts everyone's food and water security. Increasing global temperatures accelerate the hydrologic cycle and consequently impact the water resources for billions of people worldwide. Countless models have been developed to represent various components of the hydrologic cycle at various spatial and temporal scales. These are often validated against bulk fluxes and are widely used to predict the response of hydrologic systems to changing stressors. Natural tracers, such as stable water isotopes, can be applied within modeling frameworks to provide additional points of comparison between observed and modelled environmental pools and fluxes. A tracer-enabled modeling approach allows for process-level inferences based not only on the size of fluxes, but also on the spatial and temporal transport and mixing of the geochemical signatures associated with bulk fluxes. These process-level inferences can facilitate improved understanding and a multi-response evaluation of a model's performance.

In this dissertation, I show how natural tracer datasets can be applied to improve our understanding and representation of ecohydrologic processes ranging from fine-scale subsurface flow dynamics to ecosystem scale evapotranspiration (ET) flux partitions. First, I developed a statistical downscaling method which can be applied on coarse resolution time series of geochemical tracers in precipitation. The statistical downscaling

method had low absolute error across the 27 datasets from sites located worldwide. The results suggest coarsely sampled precipitation tracers can be accurately downscaled to daily values.

Next, I tested if isotopic separations occurred within 650 distinct configurations of soil properties, climatologies, and mobile/immobile soil-water domains using an advanced soil physics model. The model simulations showed separations in isotope ratios between storage and drainage waters during periods of high precipitation, soil water content, and drainage. Across soil types and climates, lower saturated hydraulic conductivity and higher rainfall rates amplified isotopic differences, illustrating how mobile and immobile domains interact with local conditions to physically result in subsurface separations. These results exposed how different critical-zone solute fluxes can be generated by representing contrasting transport dynamics in distinct domains across a range of soils and climate conditions.

Lastly, I investigated the uncertainty in total ET for three land surface models (LSMs) in the North American Land Data Assimilation System (NLDAS) configuration using observation datasets of precipitation and ET at 14 sites across the United States from the National Ecological Observatory Network (NEON). The biweekly precipitation collections of stable water isotope ratios were statistically downscaled to correspond with daily NLDAS forcings and used as conservative tracers within a mass balance model built from LSM outputs. The mass balance simulated stable water isotope concentrations (δ) for each ET partition, subsurface drainage, surface runoff, and storage. Simulated δET was directly compared to daily δET observations, which were calibrated from NEON tower measurements of atmospheric water vapor. An inter-model comparison suggested distinct differences exist amongst simulated δET and this can be associated with disparities in the relative contributions of interception, plant transpiration, and soil evaporation to the total ET. These findings can improve the general understanding of land-surface processes influencing the water and carbon cycle from regional to global scales.

Advancing the Understanding and Representation of Ecohydrological Processes using Tracer-enabled Modeling Approaches

by
Catherine Finkenbiner

A DISSERTATION

submitted to

Oregon State University

in partial fulfillment of
the requirements for the
degree of

Doctor of Philosophy

Presented November 30, 2021
Commencement June 2022

Doctor of Philosophy dissertation of Catherine Finkenbiner presented on November 30, 2021

APPROVED:

Major Professor, representing Water Resources Science

Director of the Water Resources Graduates Program

Dean of the Graduate School

I understand that my dissertation will become part of the permanent collection of Oregon State University libraries. My signature below authorizes release of my dissertation to any reader upon request.

Catherine Finkenbiner, Author

ACKNOWLEDGEMENTS

Throughout the writing of this dissertation, I have received a great deal of support and assistance.

I would first like to express my deepest appreciation to my major advisor, Dr. Stephen Good, whose expertise was invaluable in formulating the research questions and methodology. Your insightful feedback pushed me to sharpen my thinking and brought my work to a higher level.

I would like to thank my committee members: Dr. J. Renée Brooks, Dr. Christopher Still, Dr. David Noone, and Dr. Tyler Radniecki. Their knowledge, experience, and recommendations contributed to the success of my research and completion of this dissertation. I am forever grateful to them for their time and commitment to this project.

I would like to acknowledge my colleagues in the Water Resources Graduate Program and Department of Biological and Ecological Engineering. A special thank you is extended to Dr. Bonan Li for his friendship and support.

In addition, I would like to thank my parents, Kevin and Cheryl Finkenbiner, and sister, Emma Finkenbiner, for always supporting my dreams. Thank you to my partner, Subit Chakrabarti, for your love, support, and always believing in me. I am extremely grateful to Hank for never letting me down and always being ready for a walk.

Lastly, I would like to thank all the friends I have made over the years, especially Joseph Arneson, Kyla Semmendinger, Austin Raney, Emily Crampe, Mariah Lundgren, Ellie Smith-Eskridge, and Heather Hansen.

CONTRIBUTION OF AUTHORS

Stephen Good was involved in the conceptualization, methodology, data analysis, and review of Chapters 2 through Chapter 5. Stephen Good, Scott Allen, Richard Fiorella, and Gabriel Bowen provided guidance and were involved in the review of Chapter 2. Stephen Good, J. Renée Brooks, Scott Allen, and Salini Sasidharan provided guidance and were involved in the review of Chapter 3. J. Renée Brooks provided the observation datasets used in Chapter 3. Bonan Li, Lindsey Spencer, Richard Fiorella, Scott Allen, Stephen Good, Gabriel Bowen, and Christopher Still were involved in the review of Chapter 4. Bonan Li and Lindsey Spencer contributed code and helped with data analysis for Chapter 4. Richard Fiorella assisted with data acquisition and data calibration for Chapter 4. Stephen Good, Bonan Li, Richard Fiorella, Scott Allen, Gabriel Bowen, David Noone, and Christopher Still provided guidance and reviewed Chapter 5.

TABLE OF CONTENTS

TABLE OF CONTENTS (Continued)

Page

TABLE OF CONTENTS (Continued)

Page

TABLE OF CONTENTS (Continued)

Page

LIST OF FIGURES

LIST OF FIGURES (Continued)

Figure Page

LIST OF FIGURES (Continued)

Figure Page

LIST OF FIGURES (Continued)

Figure Page

LIST OF FIGURES (Continued)

Figure Page

LIST OF FIGURES (Continued)

Figure Page

LIST OF TABLES

LIST OF TABLES (Continued)

Table Page

Chapter 1. General Introduction

The hydrologic cycle has been intensifying and will continue to intensify with increasing global temperatures (IPCC, 2021; Huntington et al., 2018; Madakumbura et al., 2019; Mitchell et al., 2016). The hydrologic cycle describes the continuous movement of water in the Earth-Atmosphere system. Rising air temperatures increase the amount of moisture an air mass can hold and increase the potential for larger precipitation events. Higher temperatures also accelerate other components of the hydrologic cycle (e.g., evaporation from the land surface and water bodies, snow and ice melt; Huntington et al., 2018; Madakumbura et al., 2019; Mitchell et al., 2016). Climate change has been observed and is projected to impact regions across the globe differently. Rainfall intensities are expected to increase over most land areas, with daily extreme precipitation likely to increase by ~7% for every 1 degree Celsius. However, dry extremes are also expected in regions like the Mediterranean, southwestern Australia, southwestern South America, South Africa, and western North America (IPCC, 2021). Consequently, changes to the hydrologic cycle will impact water resources for billions of people worldwide and we need appropriate models to represent past, present, and current drivers of the hydrologic cycle.

Scientists have developed countless models representing various components of the hydrologic cycle (Overgaard et al., 2006). When developing these models, outputs are usually compared against a predefined objective function (often bulk fluxes). This leads to a common problem in hydrology called equifinality, where many different parameters or parameter sets can yield reasonable values when compared to an objective function (Kelleher et al., 2017; Beven, 2000). Natural tracers can be applied to provide additional points of comparison between observed and modelled environmental pools and fluxes (Abbott et al., 2016) and aid in the evaluating the performance and efficiency of a modelling approach (Krause et al., 2005). Tracer-enabled modeling allows for process-level inferences based not only on the size of fluxes, but also on the spatial and temporal transport and mixing of the geochemical signatures associated with the fluxes, thereby facilitating improved understanding and multi-response model evaluation (Bowen &

Good, 2015; Krause et al., 2005; McGuire & McDonnell, 2006; Sprenger et al., 2019; Turnadge & Smerdon, 2014).

Stable water isotopes are a natural tracer that has been widely applied to add additional evaluation metrics and provide new insights when drawing conclusions from hydrologic models (Chai et al., 2015; Brooks et al., 2014; Good et al., 2015; Gupta et al., 2020; Kanner et al., 2014; Remondi et al., 2018). The stable water isotope ratios of hydrogen ($^{2}H/^{1}H$) and oxygen ($^{18}O/^{16}O$), hereafter expressed as $\delta^{2}H$ and $\delta^{18}O$ (Krause et al., 2005; Bowen et al., 2015; McGuire and McDonnell, 2006; Sprenger et al., 2019; Turnadge and Smerdon, 2014; Fiorella et al., 2021), are commonly used to study land surface processes from local to global scales and provide useful information for partitioning ET into evaporation and transpiration at the ecosystem scales (Good et al., 2015; Xiao et al., 2018). Water isotopes have been used to understand water use efficiency in forests, agricultural, and other ecosystems (Wu et al., 2018; Al-Qaili et al., 2020) and provide insights into underlying principles of water and energy cycling in the soil-vegetation-atmosphere continuum (Good et al., 2015; Xiao et al., 2018; Lu et al., 2017; Wieser et al., 2016).

In many modeling applications, observed and modeled temporal resolutions are different and, in these cases, a downscaling method is required to use observed datasets within a model to evaluate processes with dynamic fluctuations over short temporal intervals (Ebtehaj & Foufoula-Georgiou, 2013). The temporal resolution at which many geochemical tracers are collected, a result of analytical or logistical cost or the need to aggregate them in time to achieve a measurable signal due to low tracer concentrations, contrasts with the time steps typical of many hydrometeorological models (Rosa et al., 2012; Gupta et al., 2020). Statistical downscaling leverages relationships observed in both fine- and coarse-scale measurements to predict fine-scale variations where only coarse-scale data are available (Ebtehaj & Foufoula-Georgiou 2013; Goncu & Albek 2016). Extensive work has focused on downscaling precipitation rate, including through use of temporal neural networks (e.g., Coulibaly et al., 2005), stochastic methods (e.g., Bordoy & Burlando, 2013; D'Onofrio, 2013; Poduje & Haberlandt, 2017), and conditional multivariate statistical models (e.g., Yang et al., 2010). However, past studies

have not temporally downscaled precipitation chemistry data, as is warranted for tracer applications.

Chapter 2 details a downscaling method that uses the statistical structure of observed stable isotope time series to downscale and generate stable isotope time series at finer resolutions. The study used daily observations of precipitation amounts and isotope ratios from 27 monitoring stations across the globe. The daily data were artificially aggregated to weekly, biweekly, and monthly scales, using amount-weighted running means to simulate coarser-scale datasets on which to apply the method. These aggregated time series were evaluated for statistical trends, specifically characterizing how the time-series means, standard deviations and correlation structures changed as the temporal sampling interval increased. Then, the statistical downscaling method was applied on each of the weekly, biweekly, and monthly aggregated tracer time series to generate downscaled tracer values. An ensemble of downscaled realizations was generated at each site, the statistics of which were compared to those of the original daily observations. The objective was to generate downscaled realizations that accurately preserved the observed daily $\delta^{2}H$ and $\delta^{18}O$ means and standard deviations and the correlation structure between precipitation amount, $\delta^{2}H$, and $\delta^{18}O$, so that these realizations could be suitable for various potential modeling applications. This statistical downscaling method was applied to study various aspects of the hydrologic cycle at different spatial and temporal scales in Chapters 3-5 of this dissertation.

In Chapter 3, I configured 650 geochemically enabled soil physics models (HYDRUS-1D; Šimünek et al., 2013; Stumpp et al., 2012) to evaluate soil water transport and mixing across a range of soil types and with simulated precipitation from different climates. This approach explicitly allowed for heterogeneous mixing of solutes at depth via a dual-porosity method. Observations of water from soils, plants, and streamflow are geochemically disparate, as was first shown by Brooks et al. (2010) and further explored in subsequent studies (Radolinski et al., 2021; Sprenger et al., 2019; McDonnell et al., 2014; Stumpp et al., 2009; Sprenger et al., 2016). These results conflict with traditional hydrologic assumptions where soil layers are well-mixed water reservoirs wherein new precipitation completely mixes with previously stored water before seeping

downward or being absorbed by roots for transpiration. Separations (i.e., differences) in tracer concentrations have specifically been reported among water traveling through preferential flow paths, water residing and tightly held within a soil matrix, and water discharged as drainage across various soil types (Radolinski et al., 2021; Barbeta et al., 2020; Berry et al., 2018; Dubbert et al., 2019; Maloszewski et al., 2006; Vargas et al., 2017) and climates (Brooks et al., 2010; Sprenger et al., 2019; Chen et al., 2020; Mueller et al., 2014; Stumpp and Hendry, 2012).

Specifically, the research objective in Chapter 3 was to test how pore heterogeneity alone (i.e., without confounding evaporative or instrumental effects; Stumpp and Hendry, 2012) can give rise to separations in soils across a range of soil types and climates. While the subsurface processes conceptualized in advanced models, such as HYDRUS-1D, represents current mechanistic knowledge within the soil-physics community, the high degree of numerical discretization coupled with the large number of non-linear functions programed into these models, requires an evaluation of these models across an ensemble of configurations to deduce those emergent priorities inherently arising from a chosen set of soil physics. It was hypothesized (1) isotopic separations should arise between water pools if a soil has heterogeneous porosities and (2) the degree of separation between water pools is controlled by soil hydraulic properties and climate conditions. This work extends beyond previous studies by identifying how interactions between climate and porosity heterogeneity within a soil profile drive incomplete mixing in soils. These results help frame how we understand and represent solute transport and mixing in the subsurface.

Chapters 4 and 5 shift to focus on leveraging observation datasets of stable water isotopes to evaluate model uncertainties and estimates of bulk fluxes. Terrestrial evaporation has long been recognized as a driving factor of the hydrologic cycle (Irmak, 2008; Katul and Novick, 2009; Long and Singh, 2012; Miralles et al., 2016) and explains ~70% of total precipitation globally (Good et al., 2015). The evapotranspiration (ET) flux connects the water, carbon, and energy cycles and is critical for understanding linked ecological processes (Jung et al., 2010; Good et al., 2015). ET is responsive to radiative forcing and changes to the atmosphere's chemical composition. As a result,

anthropogenic impacts and global climate change can impact the magnitude of the evaporative flux and influence all components of the hydrologic cycle (Wild and Liepert, 2010; Miralles et al., 2016). Large uncertainties exist in both the magnitude and direction of long-term trends in global ET, with ET increasing by 1.1 mm/year for 26% of earth's land surface and decreasing at a rate of -1.3 mm/year for 7% of earth's land surface (Feng et al., 2017). Uncertainties also exist amongst ET's partitions of 1) evaporation from the bare soil and water bodies, 2) the transfer of water vapor to the atmosphere through plant canopies (transpiration), 3) evaporation from canopy interception (interception loss), and 4) sublimation of snow and ice (Ajami, 2021; Good et al., 2015; Irmak, 2008; Katul and Novick, 2009; Kumar et al., 2018; Miralles et al., 2016). Research has estimated transpiration constitutes anywhere from 50 to 74% of total global ET (Good et al., 2015; Maxwell and Condon, 2016). These large uncertainties call for additional constraints on ET to accurately represent various components of the water and energy cycles across spatial and temporal scales.

The United States National Ecological Observatory Network (NEON) collects long-term ecological data in eco-climatologically diverse field sites across the United States and provisions these data through an open access data portal (https://data.neonscience.org/). These publicly available isotope datasets are part of an important network documenting hydrometeorological tracer patterns throughout North America. The NEON atmospheric gas stable-isotope measurements are collected at approximately hourly intervals (varying by site), enabling robust daily calculations of net-ecosystem-exchange (NEE) and evapotranspiration flux isotope ratios (e.g., via mass balance approaches developed by Keeling (Pataki et al., 2003) and Miller-Tans (Miller & Tans, 2003)). The precipitation isotope data are collected at biweekly intervals, but they can be downscaled to a daily resolution using a validated approach (Finkenbiner et al., 2021a). By conducting those pre-processing steps, we can facilitate subsequent applications using these published daily flux data products. Chapter 4 details the data descriptor associated with an open-access datasets on Hydroshare (Finkenbiner et al., 2021b). The dataset contains daily records of a) δ^2H and $\delta^{18}O$ in precipitation fluxes (F_P) at 16 NEON core sites and 16 NEON relocatable sites, b) δ^2H and $\delta^{18}O$ of ET fluxes

(F_{ET}) at 19 NEON core sites and 2 NEON relocatable sites, and c) carbon isotopes ($\delta^{13}C$) of NEE fluxes (F_{NEE}) at 19 NEON core sites and 28 NEON relocatable sites. These products form daily flux isotope datasets across diverse ecosystems over a multi-year span created using consistent instrumentation and methodology.

Chapter 5 leverages observation datasets (from Chapter 4) of stable water isotopes to evaluate the uncertainties in ET from Noah (version 2.8; Chen et al., 1996; Ek et al., 2003; Xia et al., 2012), Mosaic (Koster and Suarez, 1992, 1996), and Variable Infiltration Capacity (VIC; Liang et al., 1994) land-surface models (LSMs) implemented in the operational North American Land Data Assimilation System Phase 2 (NLDAS-2) configuration (Xia et al., 2012). Noah, Mosaic, and VIC are all validated against observation-based meteorological data (Xia et al., 2012) and provide reasonable estimates of the bulk ET flux (Zhang et al., 2020). Yet, all have striking differences in their partitions of evaporation, transpiration, and interception (Kumar et al., 2018). It was hypothesized that incorporating stable water isotopes as tracers into a mass balance model built from Noah, Mosaic, and VIC output fluxes would allow us to constrain the uncertainty in bulk ET and provide guidance toward model selection. Stable water isotope (δ^2H, $\delta^{18}O$) observation datasets of precipitation and ET fluxes were leveraged from 14 sites across the United States from the National Ecological Observatory Network (NEON). The mass balance simulated stable water isotope concentrations (δ) for input precipitation and outputs of each ET partition (i.e., evaporation from the bare soil, transpiration, interception loss, sublimation), subsurface drainage, surface runoff, and storage. Simulated δET was directly compared to daily δET observations, which were calibrated from NEON tower measurements of atmospheric water vapor. Specific research questions included: 1) Do the different ET partitions assumed by Noah, Mosaic, and VIC LSMs result in distinct differences amongst simulated δET? 2) Can stable water isotopes add additional metrics to evaluate and constrain uncertainties in δET compared to bulk fluxes? 3) Can we use simulations of δET to move toward improved model selection for representing land-surface fluxes from a site-level to global scale?

A STATISTICAL METHOD FOR GENERATING TEMPORALLY DOWNSCALED GEOCHEMICAL TRACERS IN PRECIPITATION

Catherine E. Finkenbiner, Stephen P. Good, Scott T. Allen, Richard P. Fiorella, Gabriel J. Bowen

Journal of Hydrometeorology
45 Beacon Street Boston, MA 02108-3693
Issue 6

Chapter 2. A Statistical Method for Generating Temporally Downscaled Geochemical Tracers in Precipitation

Chapter 2.1 Abstract

Sampling intervals of precipitation geochemistry measurements are often coarser than those required by fine-scale hydrometeorological models. This study presents a statistical method to temporally downscale geochemical tracer signals in precipitation so that they can be used in high-resolution, tracer-enabled applications. In this method, we separated the deterministic component of the time series and the remaining daily stochastic component, which was approximated by a conditional multivariate Gaussian distribution. Specifically, statistics of the stochastic component could be explained from coarser data using a newly identified power-law decay function, which relates data aggregation intervals to changes in tracer concentration variance and correlations with precipitation amounts. These statistics were used within a copula framework to generate synthetic tracer values from the deterministic and stochastic time series components based on daily precipitation amounts. The method was evaluated at 27 sites located worldwide using daily precipitation isotope ratios, which were aggregated in time to provide low resolution testing datasets with known daily values. At each site, the downscaling method was applied on weekly, biweekly, and monthly aggregated series to yield an ensemble of daily tracer realizations. Daily tracer concentrations downscaled from a biweekly series had average (+/- standard deviation) absolute errors of 1.69‰ (1.61‰) for δ^2H and 0.23‰ (0.24‰) for δ^{18}O relative to observations. The results suggest coarsely sampled precipitation tracers can be accurately downscaled to daily values. This method may be extended to other geochemical tracers to generate downscaled datasets needed to drive complex, fine-scale models of hydrometeorological processes.

2.2 Introduction

Naturally occurring chemical signatures in precipitation (e.g. Bailey et al. 2018, Bowen et al. 2019, Gibson et al. 2005, Kendall and McDonnell 2012, Moerman et al. 2013, West et al. 2010, Wiederhold 2015) are frequently used as hydrometeorological tracers, especially when inferring transport or chemical transformations through terrestrial, aquatic, and atmospheric environments (e.g. Abbott et al. 2016, Brooks et al. 2014, Good et al. 2015, Gupta et al. 2020, Kanner et al. 2014, Remondi et al. 2018). Tracer-enabled modeling allows for process-level inference based not only on the size of fluxes, but also on the spatial and temporal transport and mixing of the geochemical signatures associated with the fluxes, thereby facilitating improved understanding and multi-response model evaluation (Bowen and Good 2015, Krause et al. 2005, McGuire and McDonnell 2006, Sprenger et al. 2019, Turnadge and Smerdon 2014). Researchers have used tracers within global climate models to evaluate processes that are challenging to observe (e.g., ageostrophic circulations, convection and turbulence) or are modeled at sub-grid scales and are therefore not explicitly simulated but parameterized (e.g., Gupta et al. 2020, Orbe et al. 2020, Rosa et al. 2012). For instance, isotope-enabled general circulation models (GCMs) have explicitly simulated water isotope ratios within the critical zone on sub-daily time scales (e.g., a version of the Community Earth System Model (iCESM1); Brady et al. 2019, Nusbaumer et al. 2017, Wong et al. 2017) and provide outputs which have been evaluated against observational datasets at various scales (e.g., Hoffmann et al. 2000, Nusbaumer et al. 2017, Risi et al. 2012, Steen-Larsen et al. 2016, Wong et al. 2017).

In many modeling applications, observed and modeled temporal resolutions are different and, in these cases, a downscaling method is required in order to use observed datasets within a model to evaluate processes with dynamic fluctuations over short temporal intervals (Ebtehaj and Foufoula-Georgiou 2013). The temporal resolution at which many geochemical tracers are collected, a result of analytical or logistical cost or the need to aggregate them in time to achieve a measurable signal due to low tracer concentrations, contrasts with the time steps typical of many hydrometeorological models

(Rosa et al. 2012, Gupta et al. 2020). Accordingly, a method is needed to generate higher frequency datasets of precipitation chemistry from low frequency collections. Statistical downscaling leverages relationships observed in both fine- and coarse-scale measurements to predict fine-scale variations where only coarse-scale data are available (Ebtehaj and Foufoula-Georgiou 2013, Goncu and Albek 2016). Extensive work has focused on downscaling precipitation rate, including through use of temporal neural networks (e.g., Coulibaly et al. 2005), stochastic methods (e.g., Bordoy and Burlando 2013, D'Onofrio 2013, Poduje and Haberlandt 2017), and conditional multivariate statistical models (e.g., Yang et al. 2010). However, past studies have not temporally downscaled precipitation chemistry data, as is warranted for tracer applications.

Precipitation stable isotope ratios (δ^2H and $\delta^{18}O$) are an ideal test case for developing a downscaling method that can benefit tracer applications if the downscaling can preserve multi-scale statistical properties (Ebtehaj and Foufoula-Georgiou 2013). Not only is such downscaling in demand, decades of research demonstrate patterns in precipitation isotope ratios that could be leveraged in downscaling; specifically, precipitation amount often covaries with isotopic composition, attributable to the interplay of diverse climatological, physiographical, and meteorological factors in the evaporation, condensation, and transport of atmospheric moisture (e.g., Aggarwal et al. 2016, Aggarwal et al. 2012, Bowen et al. 2019, Ingraham 1998, Konecky et al. 2019, Lee and Fung 2008, Moore et al. 2016, Risi et al. 2008, West et al. 2010). This (typically inverse) covariation between precipitation rates and isotope ratios, often referred to as an "amount effect", represents partially systematic variations at sub-seasonal, monthly, and event time scales (Celle-Jeanton et al. 2001, Conroy et al. 2016, Craig 1961, Craig and Gordon 1965, Gat 1996, Lee and Fung 2008, Moore et al. 2013, Tharammal et al. 2017). If these amount effects share statistical similarities across various time scales, they could support downscaling methods to predict short-term fluctuations. Hypothetically, relationships inferred from sporadic or brief datasets could be used to predict short term variations in precipitation isotopic composition. Those patterns could be superimposed on the longer timescale seasonal patterns, which tend to follow regional patterns (Bowen et

al. 2019, Dansgaard 1964, Feng et al. 2009, Allen et al. 2019), to potentially generate realistic, continuous, high-frequency time series of precipitation isotope ratios.

In this study, we developed and evaluated a downscaling method that uses the statistical structure of observed stable isotope time series to downscale and generate stable isotope time series at finer resolutions. We used daily observations of precipitation amounts and isotope ratios from 27 monitoring stations across the globe. The daily data were artificially aggregated to weekly, biweekly, and monthly scales, using amount-weighted running means to simulate coarser-scale datasets on which to apply the method. These aggregated time series were evaluated for statistical trends, specifically characterizing how the time-series means, standard deviations and correlation structures changed as the temporal sampling interval increased. Then, the statistical downscaling method was applied on each of the weekly, biweekly, and monthly aggregated tracer time series to generate downscaled tracer values. An ensemble of downscaled realizations was generated at each site, the statistics of which were compared to those of the original daily observations. Our objective was to generate downscaled realizations that accurately preserved the observed daily δ^2H and $\delta^{18}O$ means and standard deviations and the correlation structure between precipitation amount, δ^2H, and $\delta^{18}O$, so that these realizations could be suitable for various potential modeling applications.

2.3 Data and Methods

2.3.1 Site Information and Tracer Datasets

Daily precipitation stable water isotope time series were downloaded from the International Atomic Energy's (IAEA) Global Network of Isotopes in Precipitation (GNIP) and Water Isotope System of Data Analysis, Visualization and Electronic Retrieval (WISER) database (IAEA/WMO 2020). Each time series was filtered to ensure precipitation values were greater than zero and had corresponding δ^2H and $\delta^{18}O$ isotope ratios. All time series with greater than one year of observations were selected, resulting in the 27 datasets used in the subsequent analysis; details pertaining to each site are included in Table S1 located in the *Supplementary Materials*. A minimum time series

length of one year was chosen because we wanted to account for site-specific seasonal precipitation patterns in the generated downscaled tracer time series. We acknowledge seasonality is usually characterized over time scales greater than one year, however for this analysis we decided on a minimum of one year so the downscaling method could be applied to as many datasets as possible. In the *Discussion*, the downscaling method's performance was evaluated against the number of years represented in the time series and the frequency of collection, i.e., the number of recorded precipitation events divided by the total number of days represented in the time series. The time series lengths ranged from 1.22 to 15.94 years, with an average of 5.34 years. The total number of samples in a time series ranged from 33 to 1026, with an average of ~210. The site with 33 samples (Barasat, Kolkata; Table S1) was sampled over 1.33 years.

All hydrogen and oxygen isotope ratios of precipitation were denoted as δ^2H and $\delta^{18}O$, defined by

$$\delta\ (‰) = \frac{R_{sample} - R_{std}}{R_{std}}\ 1000 \qquad \text{Eq. 1}$$

where δ was the isotope ratio in delta notation, R_{sample} was the ratio of concentrations between the rare and abundant isotopologues, and R_{std} was the isotopic ratio standard; for this analysis, that standard was the Vienna Standard Mean Ocean Water (VSMOW). The site locations and average stable water isotope observations were represented in Figure 2.1. The 27 sites have an average mean (+/- standard deviation) daily observed precipitation of 22.80 (21.38) mm, δ^2H of -37.77 (24.62) ‰ and $\delta^{18}O$ of -6.03 (3.21) ‰. The maximum recorded total daily precipitation ranged from 43.0 to 317.5 mm across sites. At the 27 sites, the observed isotope ratios ranged from -228.0 to 43.35 ‰ for δ^2H and -30.50 to 8.81 ‰ for $\delta^{18}O$. The site list included geographic locations across different climates and with uniform and seasonally varying precipitation amounts.

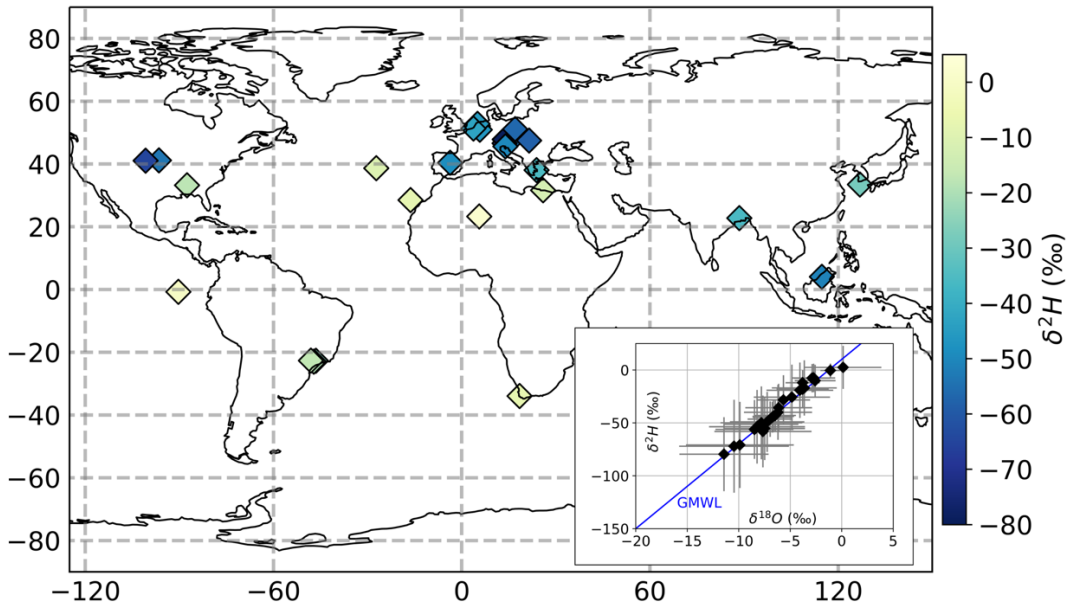

Figure 2.1. The large map displays the 27 GNIP site locations and their average δ^2H precipitation measurements. The smaller figure is a dual isotope plot with the mean and standard deviations of all daily precipitation stable water isotope measurements (δ^2H, δ^{18}O) at the 27 GNIP sites. The Global Meteoric Water Line (GMWL) is included in the subplot. Refer to Table S1 in the *Supplemental Material* for more site-specific characteristics.

Isotope ratios are often evaluated relative to the Global Meteoric Water Line (GMWL), which is defined as $\delta^2\mathrm{H} = 8\delta^{18}\mathrm{O} + 10$ ‰ (Craig, 1961). Deuterium excess (d-excess (‰) $= \delta^2\mathrm{H} - 8\delta^{18}\mathrm{O}$) measures the deviation of a water sample's composition from the GMWL (Dansgaard, 1964) and is a useful secondary tracer in that it varies with respect to the evaporation and mixing history of airmasses (e.g., Benetti et al. 2014, Fröhlich et al. 2002, Pfahl and Sodemann 2014). One can use d-excess to understand both the source of precipitation and the evolution of moisture during transport (Fröhlich et al. 2002, Good et al. 2014). We aimed to preserve a site's d-excess in the downscaled time series because it can be informative for a variety of hydrological and meteorological applications.

2.3.2 Constructing Low-resolution Datasets

We aggregated each of the 27 GNIP site's datasets using a moving, precipitation amount-weighted average (Eq. 2). This provided us with datasets of low-resolution tracer time series on which to apply the downscaling method to generate downscaled daily estimates to compare with the observed daily values. The precipitation amount-weighted average was defined as

$$\overline{\delta^2 H_t} = \frac{\sum_{i=1}^{t} P_i \delta^2 H_i}{\sum_{i=1}^{t} P_i} \quad and \quad \overline{\delta^{18} O_t} = \frac{\sum_{i=1}^{t} P_i \delta^{18} O_i}{\sum_{i=1}^{t} P_i} \qquad \text{Eq. 2}$$

where P was total precipitation (mm), $\delta^2 H$ (‰) and $\delta^{18} O$ (‰) were the daily observed stable water isotope tracer values at time t (days), and $\overline{\delta^2 H_t}$ (‰) and $\overline{\delta^{18} O_t}$ (‰) were the t-day average tracer value within the specified aggregated temporal interval. $\overline{\delta^2 H_t}$ and $\overline{\delta^{18} O_t}$ values populated a time series at t level of aggregation. We focused on downscaling time series aggregated at t values of 7-, 14-, and 28-days (weekly, biweekly, and monthly).

Time series statistics were evaluated across a range of temporal intervals. Moerman et al. (2013) investigated the correlation structure between precipitation amount and δ^{18}O at Mulu Meteo, Sarawak (Table S1) at daily to 12-week (84-days) time scales. Following their approach, we evaluated trends in the mean (μ), standard deviation (σ), and Pearson correlation coefficient (ρ) at different temporal intervals to capture the time series response and prediction accuracy. The ρ measures the linear correlation between two variables and has a value between -1 and 1, where 1 is a total positive linear correlation, 0 is no linear correlation, and -1 is total negative linear correlation. At the daily scale for the 27 GNIP sites, the average (+/- standard deviation) ρ(P, δ^2H) was -0.18 (+/- 0.18), ρ(P, δ^{18}O) was -0.20 (+/- 0.17) and ρ(δ^2H, δ^{18}O) was 0.96 (+/- 0.03).

2.3.3 Statistical Precipitation Tracer Downscaling Method

1) REMOVAL OF THE DETERMINISTIC TIME SERIES COMPONENT

Each aggregated weekly, biweekly, and monthly time series (Eq. 2) was treated as an example of a low-resolution dataset on which to apply the downscaling method. We considered each tracer time series to have a deterministic component and a stochastic component. In the first step, the deterministic component was characterized by the seasonality in the precipitation signal and was removed from each set of observations. Isotope ratios in precipitation frequently have been observed to exhibit distinct seasonal signals. These can be approximated as a combination of sinusoidal functions through Fourier decomposition (Allen et al. 2018, Allen et al. 2019, Dutton et al. 2005, Feng et al. 2009, Halder et al. 2015, Vachon et al. 2007, Wilkinson and Ivany 2002). Sinusoidal functions effectively describe the collinear structure and fluctuations in the covariation of δ^2H and δ^{18}O relative to the GMWL (Figure 2.1; Allen et al. 2018, Craig 1961, Dansgaard 1964). The sine curve parameters (amplitude, phase, and offset) are often predictable in space (Allen et al. 2018, Jasechko et al. 2016) and succinctly represent temporal dynamics because they express continuous, cyclic time series. Allen et al. (2019) used monthly isotopes in precipitation GNIP datasets from across the globe to capture patterns in the precipitation isotope seasonality using sinusoidal functions. When predicting the isotope seasonality, the values of the sine parameters can be described as functions of climate and geography. Additionally, sine curves are useful when describing the propagation of cyclic signals, this has been done to infer catchment-scale mixing processes using the dampening ratio of seasonal isotope amplitudes in streamflow versus precipitation (Kirchner 2016a, 2016b; also see Clow et al. 2018, von Freyberg et al. 2018, Gallart et al. 2020, Jacobs et al. 2018, Jasechko et al. 2016, Lutz et al. 2018, Song et al. 2017).

We fitted sinusoidal functions to each of the site's daily to 12-week aggregated time series to describe the deterministic components using a non-linear, least squares fitting routine, "curve_fit" in Python's (v3.7.6) SciPy Library (v1.2.1), following the methods from Allen et al. (2018). We used a time-weighted fit routine (i.e., not amount

weighted and each daily sample had equal weight) to approximate the parameters of the sinusoidal function (Eq. 3) because our ultimate goal related to predicting daily precipitation variations in isotopic composition, regardless of whether or not they are associated with larger events. The sine functions were defined with a fixed period of one year and

$$Precipitation\ \delta^2H \text{ or } \delta^{18}O(f) = A\,sin(2\pi f - \phi) + b, \quad \text{Eq. 3}$$

where *f* was the fractional year and *b* was an offset parameter (Allen et al. 2018). All fitted amplitudes (*A*) and phases (ϕ) were bounded so the amplitude values were positive, and the phase ranged between $-\pi$ and π. The presence of large seasonal isotope cycles enables the quantification of mixing, transport, and turnover of water in landscape and/or biota. Amplitude dampening reflects mixing processes, phase shifts reflect advective travel times and offset differences reflect proportional contributions of different seasons' precipitation (Kirchner 2016a, 2016b). The defined sinusoidal functions were subtracted from the daily to 12-week aggregated series, thus removing the deterministic time series components.

2) GENERATION OF STOCHASTIC TRACER REALIZATIONS

Next, the daily statistics of the stochastic hydrogen (δ^2H^*) and oxygen ($\delta^{18}O^*$) isotope time series were estimated by using the relationship between the observed daily stochastic statistics and the stochastic signal's statistics across a range of aggregation intervals (t) multiplied by each site's specific precipitation frequency (λ; defined as the number of days with precipitation divided by the total number of days in a time series). The statistics of the stochastic signal at aggregation interval *t* were denoted with * as μ_t^*, σ_t^*, and ρ_t^* and estimates of these at the daily (*t*=1) resolution were denoted as $\hat{\mu}_1^*$, $\hat{\sigma}_1^*$, and $\hat{\rho}_1^*$. After removal of the deterministic component, the stochastic signals had mean isotope values of approximately zero across all ranges of $t\lambda$ (Figure 2.2.a,b). Consequently, we assumed the stochastic signal to behave as a purely random mean zero process ($\hat{\mu}_1^* = 0$),

which was further substantiated using tests for independence, autocorrelation, and normality on the stochastic signal (refer to *Sections 2.d* and *3.d*).

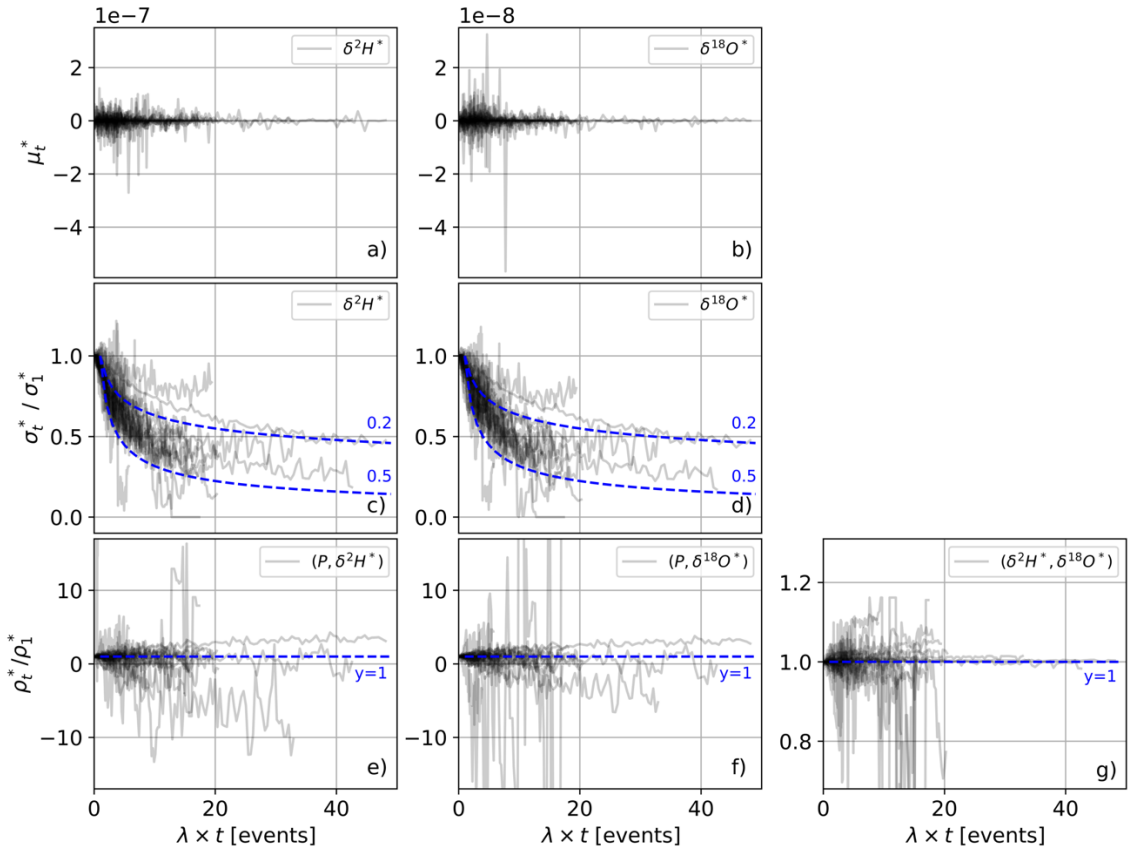

Figure 2.2. The x-axis is $\boldsymbol{\lambda}$ (recorded events / number of days in the time series) multiplied by daily to 12-week aggregation intervals (days) and the y-axes were the deviations for each of the 27 sites in their stochastic time series a,b) means ($\boldsymbol{\mu_t^*}$; note the scale of the y-axis), c,d) standard deviations at *t*-day ($\boldsymbol{\sigma_t^*}$) divided by the daily standard deviation ($\boldsymbol{\sigma_1^*}$) with blue dashed lines at $(\boldsymbol{\lambda n})^{\mathbf{0.5}}$ and $(\boldsymbol{\lambda n})^{\mathbf{0.2}}$, and e-g) Pearson correlation coefficients at *t*-day divided by daily ($\boldsymbol{\rho_t^*/\rho_1^*}$) with blue dashed lines at y-axis = 1. Refer to *Supplemental Materials* (Fig. 2.S1) for larger ranges in y-axis values for ($\boldsymbol{\rho_t^*/\rho_1^*}$).

The time series standard deviations were greatest at daily time scales and decreased with increasing $t\lambda$ as a power law function (Figure 2.2.c,d). This decrease resulted from the averaging and weighting of individual daily tracer concentrations by precipitation amounts over longer temporal intervals. By the Central Limit Theorem and the Law of

Large Numbers, as the sampling size increases, the sampling distribution converges to a normal distribution where the standard deviation decreases at a rate of $1/n^{0.5}$, where *n* is a number of samples. It should be noted, the results from the Central Limit Theorem and the Law of Large Numbers holds as long as the signal is purely stochastic and there are no trends or heteroscedasticity in the time series. It was assumed a similar relationship was held between the daily standard deviation of days with precipitation tracer values (σ_1^*, ‰) and the series of known *t*-day aggregation intervals (days) with their corresponding standard deviations in time (σ_t^*, ‰). $t\lambda$ estimated the expected number of precipitation events in each aggregation level because precipitation does not occur every day (e.g., $n \approx t\lambda$). We expressed this relationship as

$$\sigma_t^* = \frac{\hat{\sigma}_1^*}{(t\lambda)^a}, \qquad \text{Eq. 4}$$

where *a* is a site-specific parameter defining the rate decrease in σ_t^* with increasing *t*. We used the non-linear, least-squares fitting routine, "curve_fit", in Python's (v3.7.6) SciPy Library (v1.2.1) to estimate the *a* and $\hat{\sigma}_1^*$ parameters in Eq. 4. a was constrained between 0.2 and 0.5 in order to bound the curve fitting routine. When $\hat{\sigma}_1^*$ was compared with σ_1^*, a values below 0.2 often underpredicted $\hat{\sigma}_1^*$ and above 0.5 often overpredicted $\hat{\sigma}_1^*$. The initial value predicted for *a* was set at 0.3, however varying this had negligible influence on the final *a* parameter estimates and the *a* parameter estimates were not strongly related to observed standard deviation (for δ^2H^* and $\delta^{18}O^*$ $R^2 < 0.002$ and p-value > 0.75). To estimate the daily standard deviation at a site with a biweekly ($t = 14$) sampling frequency, first λ must be calculated and the time series can be aggregated to 28-, 42-, 56-, 70-, and 84-day intervals (Eq. 2) for 2*t* to 6*t,* giving 6 points to fit Eq. 4. Weekly time series were aggregated from 2*t* to 12*t* (12 points), while monthly time series were aggregated from 2*t* to 3*t* (3 points). This quantified the decrease in σ_t^* from the available data resolution out to 12 weeks (84-days), and allows *a* and $\hat{\sigma}_1^*$ to be estimated.

The ratio of ρ_t^* divided by ρ_1^* across λt was relatively invariant and centered around one (Figure 2.2.e-g). Thus, Pearson correlation coefficients at a *t*-day aggregation interval

(ρ_t^*) were used to describe the daily correlations ($\hat{\rho}_1^*$) between precipitation amount and the stochastic signal's δ^2H^* and $\delta^{18}O^*$ values.

Pseudo-random numbers were generated using a Gaussian copula (Sklar 1959), defined by the estimated daily statistics, $\hat{\mu}_1^*$'s, $\hat{\sigma}_1^*$'s, and $\hat{\rho}_1^*$'s, and conditioned on the observed daily precipitation amounts. Other copula families are possible (e.g. Archimedean copula, Gumbel copula); however, here the Gaussian copula was used because it offered a simple approach for modeling the dependence of multivariate states (Schneider and Ramos 2014). In probability theory and statistics, the marginal distribution of a subset of a collection of random variables is the probability distribution of one random variable without any reference to other random variables. Copula models separate the dependency structure of multiple random variables from their marginal distributions by mapping each variable through its cumulative distribution functions (CDF) to the unit interval (i.e. closed interval [0,1]). This captures the dependence between the variables using a copula or coupling term, allowing a different marginal distribution for each variable while capturing the multivariate dependencies (Schneider and Ramos 2014, Sklar 1959). Here, a copula captured the multivariate dependencies between precipitation amount, δ^2H^* and $\delta^{18}O^*$. Refer to *Supplemental Material* for further detail on the definition of the Gaussian copula used here. Models using copula techniques have captured the spatial and temporal patterns of precipitation characteristics (Kuhn et al. 2007, Gao et al. 2018), temporally downscale precipitation datasets (Gyasi-Agyei 2011, So et al. 2017), to forecast precipitation events (Bárdossy and Pegram 2009, Khedun 2014) and across other hydrological disciplines (e.g. temperature and rainfall dynamics (Cong and Brady 2012, Schölzel and Friederichs 2008), extreme-value stochastic rainfall events (Kuhn et al. 2007, Laux et al. 2011, Huang et al. 2012), drought distributions from monthly rainfall (Laux et al. 2009), hydraulic conductivity of aquifer systems (Haslauer et al. 2012), and groundwater recharge from precipitation events (Jasechko and Taylor 2015).

For each observed precipitation amount, values of δ^2H^* and $\delta^{18}O^*$ (a 2-number sample representing the stochastic signal) were drawn from a multivariate Gaussian distribution using Python's (v3.7.6) SciPy Library (v1.2.1) with parameters described by

$\hat{\rho}_1^*(P, \delta^2H^*)$, $\hat{\rho}_1^*(P, \delta^{18}O^*)$ and $\hat{\rho}_1^*(\delta^2H^*, \delta^{18}O^*)$ (refer to Eq. 9 and 10 in the *Supplemental Material*). The covariates used here were precipitation amount and its isotopic composition, however it should be noted the covariates can change depending on the method's application and data availability. Next, Gaussian CDF values were calculated for each of the generated series. The resulting uniform values were then used to resample from the coarse resolution empirical distribution of isotope ratios for each site, formed by the deseasonalized time series. Each of these values was then rescaled by $\hat{\sigma}_1^*/\sigma_t^*$. The resulting stochastic time series were daily $\delta^2\mathrm{H}^*$ and $\delta^{18}\mathrm{O}^*$ values conditioned on observed precipitation amounts with means of zero, standard deviations of $\hat{\sigma}_1^*$ and Pearson correlation coefficients of $\hat{\rho}_1^*$.

3) FULL SYNTHETIC TIME SERIES GENERATION

The deterministic component, the sinusoidal function from Eq. 3, was added to each generated stochastic time series. The result was a downscaled tracer time series which captured site-specific daily precipitation amount effects, seasonal signals, and stochastic variability. Finally, we applied a residual correction on the downscaled synthetic series to preserve the observed aggregated weighted tracer values. For each synthetic value within each aggregation interval, an interval-specific, single correction factor was subtracted from the downscaled values so that there was no difference between that period's downscaled synthetic values aggregated for that interval and the observed coarse-resolution interval's value. In doing so, the precipitation-weighted values of the synthetic time series then equaled the known aggregated value. This property is particularly important as it closes the tracer mass balance. The statistical downscaling method applied to a dataset with a biweekly sampling frequency was summarized and visualized in *Section (ii)* of the *Supplemental Material*.

2.3.4 Evaluation of Precipitation Tracer Downscaling Methodology

The statistical method was iterated over 100 times generating an ensemble of downscaled isotope time series at each of the 27 GNIP locations. The large number of time

series generated for each ensemble allowed for us to quantify the performance of the downscaling method. Each ensemble was expected to capture the observed site-specific tracer means and standard deviations and the correlation coefficients between precipitation amount, δ^2H and $\delta^{18}O$. The statistical downscaling method was evaluated using multiple techniques, detailed in the subsequent paragraphs.

After removing the deterministic components, the stochastic time series were expected to have means of approximately zero, a predicable decrease in standard deviation (Eq. 4) and Pearson correlation coefficients at low temporal resolutions appropriately defining daily covariate structures. To test this, σ_1^* and ρ_1^* of the observed datasets were compared to $\hat{\sigma}_1^*$ and $\hat{\rho}_1^*$ of downscaled ensembles using root-mean squared error (RMSE), mean bias error (MBE), and R-squared (R^2). Autocorrelations with lags ranging from 1- to 20-days (Figure 2.6, refer to *Section 3.c*) and tests for normality were calculated for the stochastic signal of the observed datasets and downscaled ensembles.

The average of ensemble means ($\overline{\hat{\mu}_1}$) and standard deviations ($\overline{\hat{\sigma}_1}$) for each isotope ratio and the Pearson correlation coefficients ($\overline{\hat{\rho}_1}$) between precipitation amount and each isotope ratio were compared to the observed daily statistics. R^2 values were calculated for the downscaled ensembles and observed daily site statistics. Each site's observed *d*-excess was evaluated against the downscaled ensemble's *d*-excess. Lastly, we compared the absolute error between the downscaled ensemble and observed time series means to various site-specific and time series characteristics.

2.4 Results

2.4.1 Evaluation of Estimated Daily Stochastic Signal Statistics

The estimated daily stochastic signal statistics from weekly, biweekly, and monthly aggregation intervals accurately described the observed statistics (Figure 2.3). The method best predicted $\hat{\sigma}_1^*$ when applied to a weekly series, while the worst approximations of $\hat{\sigma}_1^*$ occurred when it was applied to a monthly series. We expected the weekly time series to

best predict $\hat{\sigma}_1^*$ because it better characterizes the change in tracer concentration variance as more values of *t* were used to fit the $\hat{\sigma}_1^*$ and *a* parameters in Eq. 4. For all 27 GNIP sites, the δ^2H $\hat{\sigma}_1^*$ had RMSEs of 2.73 ‰ (MBE = -1.92 ‰) for a weekly series, 5.21 ‰ (MBE = -3.72 ‰) for a biweekly series, and 7.83 ‰ (MBE = -6.02 ‰) for a monthly series. The δ^{18}O $\hat{\sigma}_1^*$ had RMSEs of 0.35 ‰ (MBE = -0.77 ‰) for a weekly series, 0.64 ‰ (MBE = -0.48 ‰) for a biweekly series, and 0.98 ‰ (MBE = -0.24 ‰) for a monthly series. For weekly, biweekly, and monthly series, $\hat{\rho}_1^*$(P, δ^2H), $\hat{\rho}_1^*$(P, δ^{18}O), and $\hat{\rho}_1^*$(δ^2H, δ^{18}O) had low RMSEs ranging from 0.01 to 0.18 ‰ and MBEs ranging from -0.01 to 0.03 ‰ across all sites. $\hat{\rho}_1^*$(P, δ^2H) and $\hat{\rho}_1^*$(P, δ^{18}O) were more likely to be overestimated for sites with ρ_1^*(P, δ^2H) and ρ_1^*(P, δ^{18}O) near zero, most likely a result of a site's weak amount effect that can become less significant and sometimes positive as a time series is aggregated. More data could improve estimates of $\hat{\rho}_1^*$. The *Discussion* provides further detail on methods for potentially improving statistical estimates at sites where errors were more apparent.

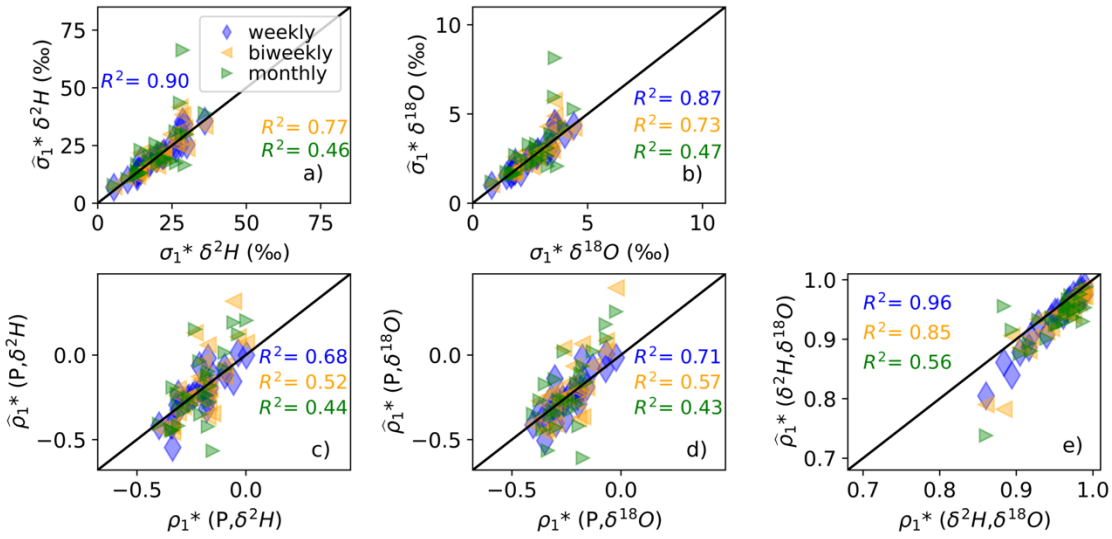

Figure 2.3. The estimated standard deviations (a,b) and Pearson correlation coefficients (c-e) of the stochastic signal from downscaled weekly, biweekly and monthly time series compared to the observed daily stochastic statistics. Each data point is one site location and the black lines are the 1:1 lines. The means were not shown because they are approximately zero (refer to Figure 2.S2.a,b).

2.4.2 Evaluation of the Downscaled Tracer Realizations

The average of each ensemble's means ($\overline{\hat{\mu}_1}$) and standard deviations ($\overline{\hat{\sigma}_1}$) for each isotope ratio and the Pearson correlation coefficients ($\overline{\hat{\rho}_1}$) between precipitation amount and its corresponding isotope ratios were compared to the observed daily statistics at each site before applying the residual correction (Figure 2.4). The downscaled time series with the most accurate $\overline{\hat{\rho}_1}$ were calculated when the method was applied to a weekly time series. After applying a residual correction on each realization in an ensemble, the residual corrected downscaled series accurately captured the μ_1, σ_1, and ρ_1 (Figure 2.5), though slightly altered R^2 values. The R^2 between $\mu_1$and $\overline{\hat{\mu}_1}$ and σ_1 and $\overline{\hat{\sigma}_1}$ were similar for the original downscaled (Figure 2.4.a-d) and residual corrected ensembles (Figure 2.5.a-d). The residual correction increases the R^2 between ρ_1 and $\overline{\hat{\rho}_1}$ (Figure 2.4.e-g, Figure 2.5.e-g), especially when it is applied on a downscaled weekly series. For a downscaled weekly series, the R^2 of $\rho_1(P, \delta^2H)$ and $\overline{\hat{\rho}_1}(P, \delta^2H)$ and $\rho_1(P, \delta^{18}O)$ and $\overline{\hat{\rho}_1}(P, \delta^{18}O)$ increased from 0.88 to 0.93 with a residual correction. For applications where model outputs are directly compared to observation datasets, a residual correction should be applied to generate tracer ensembles which are comparable to the coarser resolution observed values. The average bias between the downscaled and observed time series means and standard deviations were summarized in Table 1. The residual correction on the downscaled ensembles reduced bias in the standard deviations but had little effect on the means. The *Discussion* provides further detail on potential methods for adding informative covariates (e.g. air temperature) to the downscaled time series estimates at sites where errors were more apparent.

Table 2.1. Average bias (predicted - observed statistic) (+/- standard deviation) for downscaled and *residual corrected downscaled* ensembles

	Bias in the Means (‰)				**Bias in the Standard Deviations (‰)**			
	δ^2H	***δ^2H***	**δ^{18}O**	***$\delta^{18}O$***	**δ^2H**	***δ^2H***	**δ^{18}O**	***$\delta^{18}O$***
Weekly	-0.10 (1.39)	*0.01 (1.79)*	-0.02 (0.20)	*-0.03 (0.26)*	0.02 (2.38)	*1.95 (3.30)*	0.004 (0.34)	*0.25 (0.46)*
Biweekly	-1.00 (2.20)	*-0.68 (3.50)*	-0.16 (0.30)	*-0.12 (0.46)*	1.04 (3.95)	*2.76 (4.14)*	0.17 (0.56)	*0.39 (0.59)*
Monthly	-1.43 (3.08)	*-0.13 (5.86)*	-0.23 (0.43)	*-0.05 (0.74)*	2.20 (8.75)	*3.28 (8.81)*	0.28 (1.12)	*0.43 (1.12)*

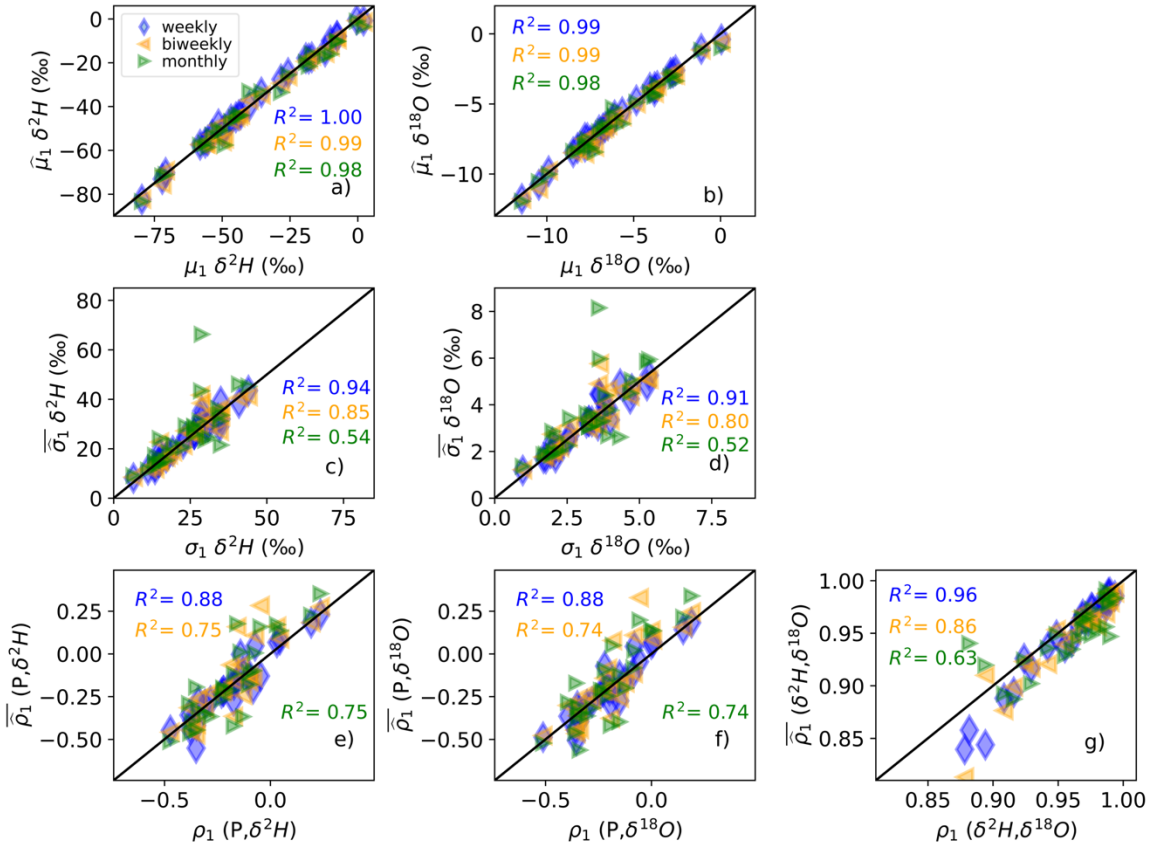

Figure 2.4. The average means (a,b), standard deviations (c,d) and Pearson correlation coefficients (e-g) of the downscaled ensembles from the weekly, biweekly and monthly time series compared to the observed daily site statistics. Each data point is one location and the black lines are the 1:1 lines.

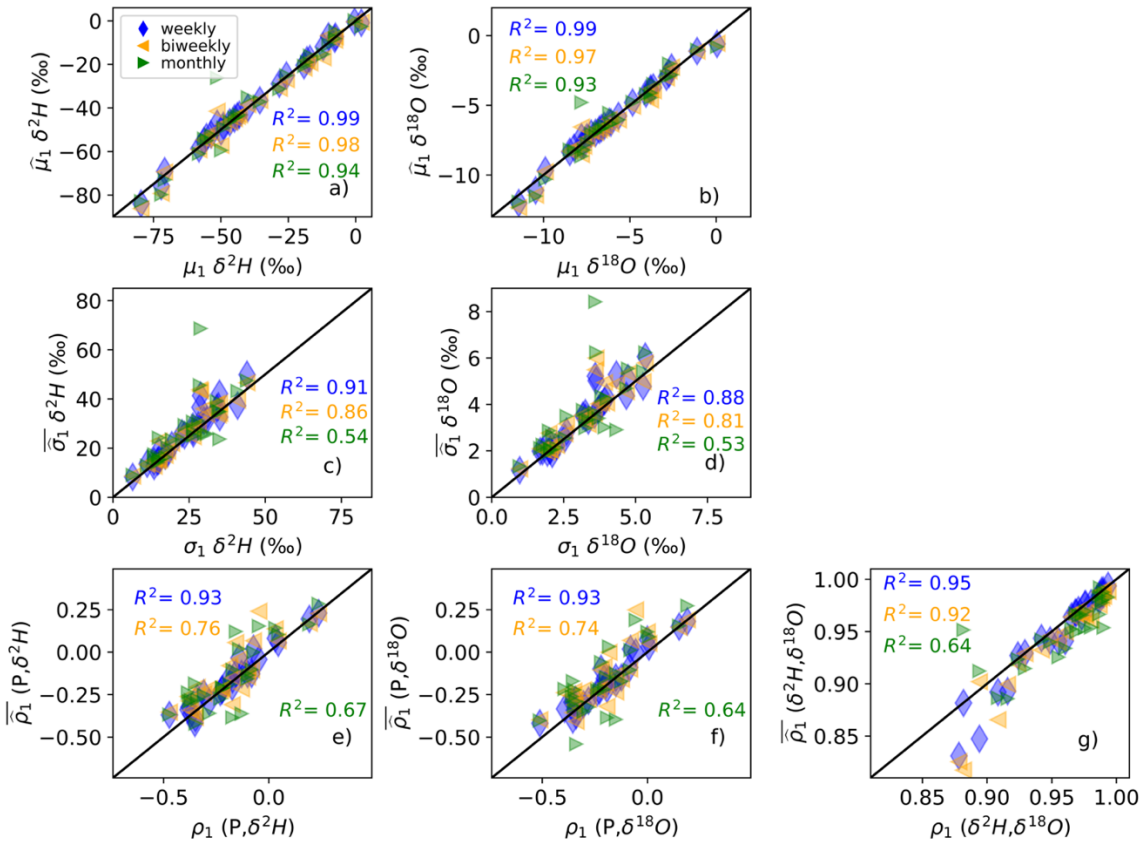

Figure 2.5. The average means (a,b), standard deviations (c,d) and Pearson correlation coefficients (e-g) of the residual corrected downscaled ensembles from the weekly, biweekly and monthly time series compared to the observed daily site statistics. Each data point is one location and the black lines are the 1:1 lines.

2.4.3 Conserved Processes with the Method

An analysis of the observed time series demonstrates strong autocorrelation; when the seasonal signal is removed, the observed autocorrelation is nearly all removed (Figure 2.6). In fact, the median autocorrelation of the observed time series stochastic signals falls below 5 % after 3-day lags and are approximately zero at 4-day lags, supporting the assumption that the sinusoidal function adequately described the deterministic component, and the residual was stationary (i.e., white noise). The Shapiro-Wilk and the D'Agostino's K^2 normality tests suggest that we could not reject the assumption of normality in the weekly, biweekly, and monthly time series (p-value > 0.05). Histograms of the stochastic

signals for both isotope ratios across all 27 sites are provided in the *Supplemental Materials* (Figure 2.S3). Next, we calculated autocorrelations from 1- to 20-day lags of the residual corrected downscaled ensembles. The autocorrelations mimicked the observed temporal trends and memory of the daily time series. Autocorrelations for δ^2H and δ^2H^* (Figure 2.6) and are highly correlated with trends observed in the autocorrelations for $\delta^{18}O$ and $\delta^{18}O^*$ (refer to *Supplemental Materials,* Figure 2.S4). Based on the results from the autocorrelation analysis and normality tests, we concluded the addition of the seasonal signal to the generated stochastic time series captured most of the observed tracer memory in the system.

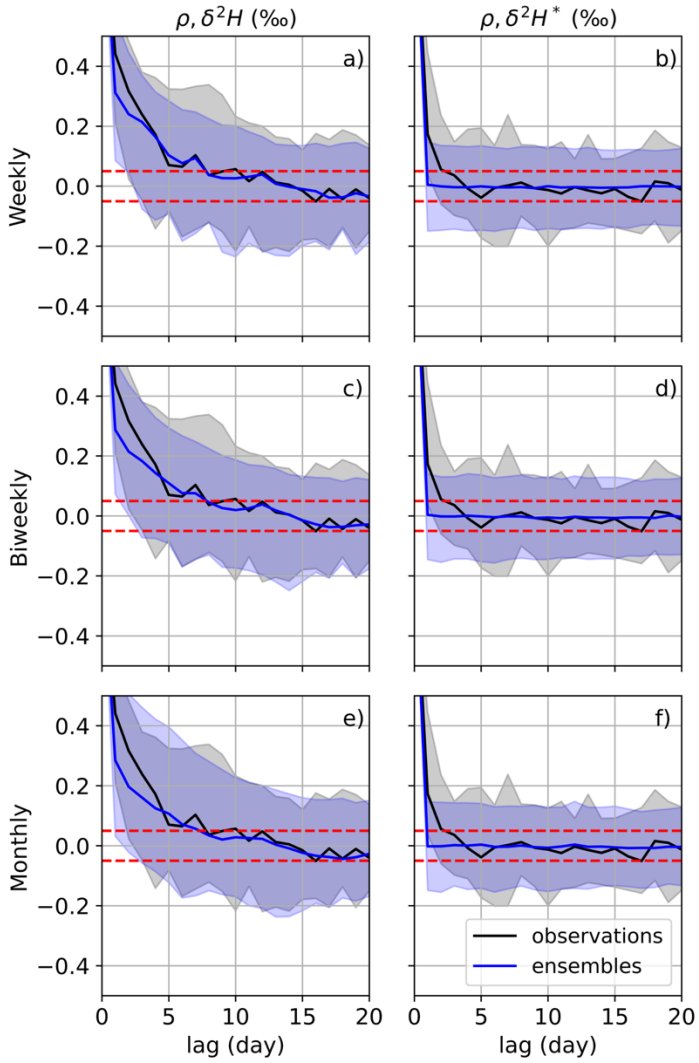

Figure 2.6. a,c,e) Median autocorrelation of the observed daily δ^2H datasets and the daily residual corrected ensembles (solid lines). b,d,f) Median autocorrelations of the δ^2H^* stochastic signals for the observations and the downscaled ensembles. The 5th to 95th percentiles of the observed and ensemble autocorrelations are represented as shaded regions. Horizontal red dashed line indicates where ρ is +/-5%.

The means and standard deviations in *d*-excess were accurately captured in the resulting downscaled time series (Figure 2.7). At each site, *d*-excess was calculated for the observed daily series and each ensemble from the downscaled weekly, biweekly, and monthly time scales. The downscaled *d*-excess was over-estimated for the three sites with lowest observed *d*-excess, indicating potential effects to the downscaling method's

performance when precipitation is predominantly composed of evaporated waters. These *d*-excess estimates provide a metric for evaluating the downscaled series relative to the GMWL and increases the applicability of this method for tracing meteorological forcing variables and their constituents through modeling environments. Alternative downscaling approaches that independently model δ^2H and $\delta^{18}O$ may not preserve *d*-excess signals and thus would provide precipitation predictions that should not be used in simulations that leverage the information provided by dual-isotope analyses.

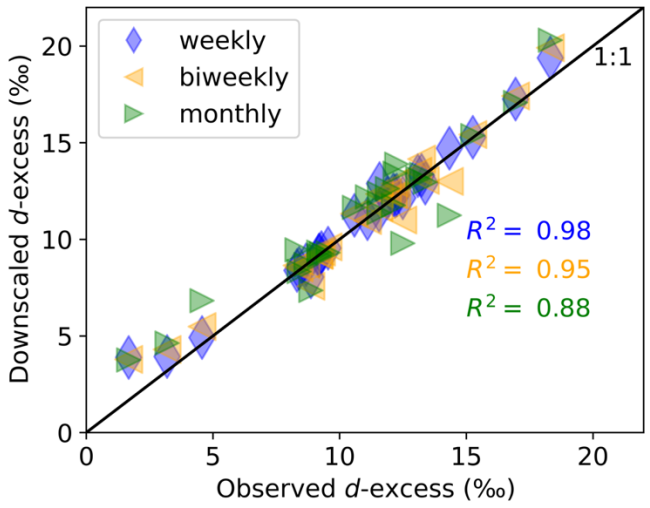

Figure 2.7. The average *d*-excess of the residual corrected downscaled ensemble at each site location compared to the average observed *d*-excess. Each data point is one site location, and the black line is the 1:1 line.

2.5 Discussion

2.5.1 Method Evaluation for Select Site Characteristics

We compared the absolute error, calculated by taking the absolute value of the mean of the downscaled ensembles minus the observed mean, to the site's latitude, calculated rainfall frequency (λ), and total length of the time series in years (Figure 2.8). The largest absolute errors of the mean resulted from downscaling calculations that used monthly aggregated data, yielding average (+/- standard deviation) absolute errors of 2.26

‰ (2.54 ‰) for δ^2H and 0.33 ‰ (0.35 ‰) for $\delta^{18}O$. Linear regressions between site latitude and absolute errors in the means (derived from monthly, biweekly, and weekly ensembles) showed no strong correlations, suggesting that performance may be partially climate independent (Figure 2.8). Absolute errors were also not related to the strength of the seasonal isotopic variation, nor were they related to the overall variability in isotopic composition (as quantified by the standard deviation; Figure 2.9). Alternatively, a weak, but significant relationship was observed between absolute error and λ ($R^2 = 0.25$ and p-value = 0.0001 for δ^2H, $R^2 = 0.23$ and p-value = 0.0002 for $\delta^{18}O$) and average recorded precipitation amount ($R^2 = 0.12$ and p-value = 0.009 for δ^2H, $R^2 = 0.13$ and p-value = 0.0003 for $\delta^{18}O$) for downscaled weekly ensembles, but not for downscaled biweekly or monthly ensembles (Figures 2.8 and 2.9). Although not a site characteristic, time-series length significantly influenced absolute errors of downscaled biweekly and monthly ensembles. Longer time series spanning many years support better accounting for interannual variability and removing potential biases towards certain seasons. Nonlinear effects (e.g., continentality (Dansgaard 1964, Rozanski et al., 1993)) may be contributing to relatively high absolute errors, especially at the subtropics and mid-latitudes (Figure 2.8.a-b). When applying the downscaling method to datasets from these regions, one can adapt the copula framework to account for other influential site-specific characteristics (refer to *Section 2.b)*.

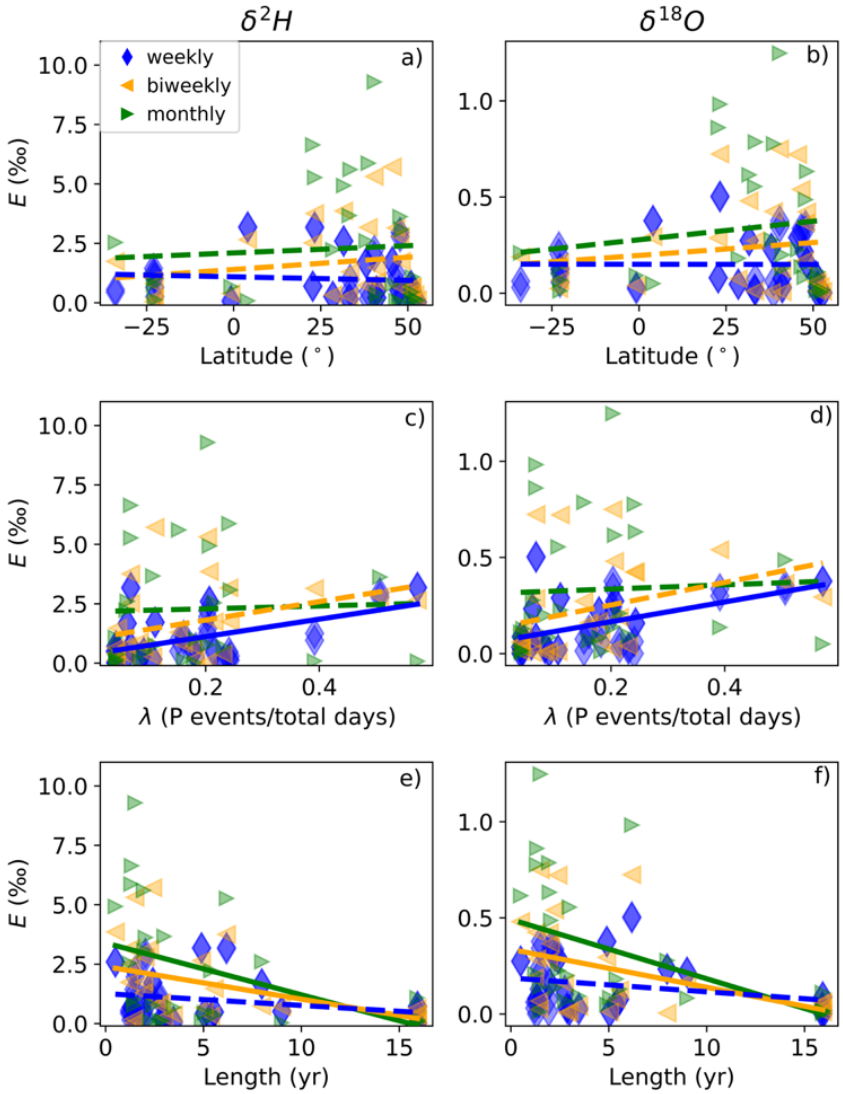

Figure 2.8. Absolute error (E) of the residual corrected ensemble means compared to various site-specific characteristics: a,b) latitude, c,d) λ, and e,f) total length of the time series. Each data point is one site location, dashed lines represent p-values > 0.05, and solid lines represent p-values < 0.05.

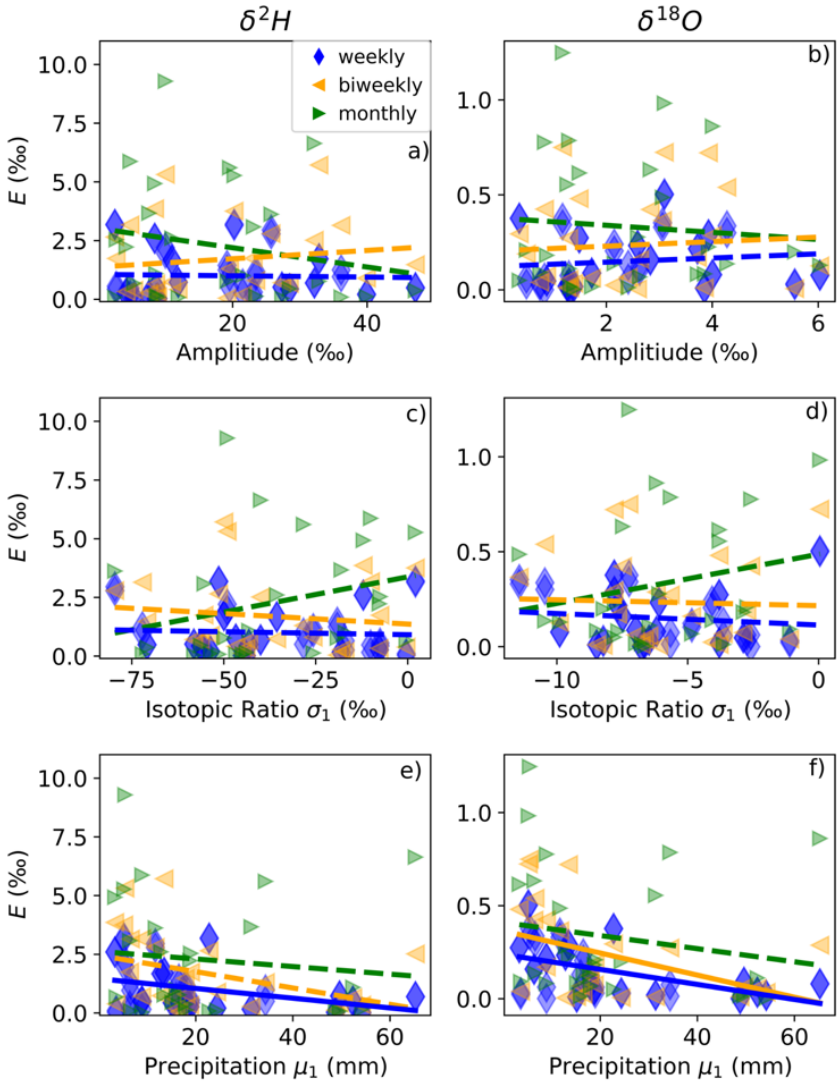

Figure 2.9. Absolute error (E) of the residual corrected ensemble means compared to various site-specific characteristics: a,b) the sinusoidal function's estimated amplitude, c,d) standard deviation of each isotope ratio and e,f) average daily precipitation. Each data point is one site location, dashed lines represent p-values > 0.05, and solid lines represent p-values < 0.05.

2.5.2 Method Adaptation for Broader Applications

In this study, weekly, biweekly, and monthly data were used to generate daily observations, but more sophisticated applications could potentially be supported by different datasets. Generally, the deterministic time series component can be more

accurately estimated with increased tracer sampling frequencies (Figure 2.8.c-d) and samples collected over longer time frames (Figure 2.8.e-f). Accurately representing the deterministic component increases the likelihood of a downscaled synthetic time series effectively representing the underlying seasonal patterns and interannual variability at a site. Depending on the application, one may increase or decrease the temporal downscaling intervals beyond daily or 12-week timescales. While not evaluated in this study, one could predict sub-daily datasets with appropriate observation datasets or known statistical properties (i.e., mean, standard deviation, covariance structure of precipitation and its tracer composition) of a site at sub-daily scales (e.g., diurnal cycle).

Theoretically, the downscaling methods used in this study can be expanded to higher dimensions and account for other tracer covariates including site conditions such as air temperature and relative humidity. At sites where the method under or overestimates the site statistics, other meteorological variables, such as air temperature, may correlate more strongly with isotope signals than precipitation amount. To do this, one needs to increase the number of covariates accounted for and the matrix dimensions within the copula framework (refer to *Supplemental Materials (i) Definition of a Gaussian Copula).* In these instances, adding more known dimensions to Equations 6 and 7 will incorporate additive information into the generated downscaled time series. Including additional known covariates within the copula framework may improve the representation of nonlinear effects at sites in the subtropics and mid-latitudes if meteorological variables (e.g., relative humidity, air temperature) are highly correlated with changes in tracer concentrations (Figures 2.8.a-b).

Not only would a downscaled time series facilitate running more detailed models that improve process understanding, but they also allow for better tracking of uncertainties associated with inferences drawn from those models. We compared the mean of the observed biweekly series and the mean of the downscaled biweekly ensemble aggregated to biweekly time scales using Eq. 2. The absolute error of the mean across all sites was 0.90 ‰ for δ^2H and 0.14 ‰ for $\delta^{18}O$. This suggests models using downscaled tracers would mimic temporal trends observed at biweekly time scales, while also tracking processes and uncertainties only discernible at finer time scales. As expected, when the

residual corrected downscaled biweekly ensemble was aggregated to biweekly time scales, the absolute error of the mean was approximately zero. To evaluate how the downscaling method compared to a naive downscale with no high-frequency statistical information, we created a daily time series where all precipitation events that occurred within each 14-day interval had the same isotopic composition equal to the observed biweekly values. The absolute error of the mean across all sites (+/- standard deviation) was 2.74 ‰ (2.24 ‰) for δ^2H and 0.39 ‰ (0.31 ‰) for $\delta^{18}O$, which was higher than the absolute error of the mean calculated for all the downscaled biweekly ensembles (1.69 ‰ (1.61 ‰) for δ^2H and 0.23 ‰ (0.24 ‰) for $\delta^{18}O$).

Due to limited data, all the above analyses used the entire dataset to calculate the statistics, fit the models and apply the downscaling method. At sites with more than 5 years of data, we used the first 4 years to build a downscaling model to apply on the 5th year's precipitation time series. We generated an ensemble of 100 downscaled δ^2H and $\delta^{18}O$ time series at each site and compared it to the observed δ^2H and $\delta^{18}O$ from the 5th year of the time series. Based on training and testing sizes, eight sites were used in this analysis and the absolute error of the mean (+/- standard deviation) for δ^2H was 4.80 ‰ (3.17 ‰), 4.89 ‰ (3.26 ‰) and 5.52 ‰ (3.50 ‰) downscaled from weekly, biweekly, and monthly series, respectively. The absolute error of the mean (+/- standard deviation) for $\delta^{18}O$ was 0.79 ‰ (0.59 ‰), 0.78 ‰ (0.63 ‰) and 0.85 ‰ (0.67 ‰) downscaled from weekly, biweekly, and monthly series, respectively. Based on these promising results, our downscaling method could be built using several years of precipitation data with a known concentration and then applied to years where only precipitation amount is available.

This method can be broadly applied to produce ensembles of downscaled datasets for various geochemical modeling applications. Ensembles decrease the risk of tying conclusions to one specific time series. The downscaled ensembles can be generated using the same statistics (like shown here) or multiple ensembles can be generated with varying statistical properties. Examples of different ensembles include time series generated from downscaled statistics estimated from different aggregation intervals (e.g., weekly and biweekly), employing a non-Gaussian copula framework (e.g., Gumbel copula, Extreme-

value copula) to populate a conditioned stochastic signal's time series, and increasing dimensions of the copula framework by including additive meteorological variables (e.g., air temperature). Correspondingly, the geochemical tracer ensembles could be used for model selection and with numerous model and parameter sensitivity and uncertainty analyses. Ensembles could be useful in developing frameworks for model-data fusion by merging observational data with model outputs to improve model quality and characterize its uncertainty.

This downscaling approach could be extended across large spatial extents for use in global isotopic models or empirically based geographic simulations to represent sites with limited or no high-frequency observations available. To do this, one could generate downscaled geochemical tracers correlating with precipitation inputs at the grid-scale. Lastly, the methodology can be applied to other geochemical tracers for understanding site-specific dynamics (e.g., chemical leaching, sediment transport and loading) or climatological applications (e.g., nitrogen deposition, carbon sequestration).

2.6 Conclusions

This statistical downscaling method generates datasets that maintain informative site-specific correlation structures between covariates and the geochemical tracer and retains the statistical properties of underlying processes (e.g., *d*-excess, amount effects). By modeling hydrologic dynamics using downscaled tracers, researchers can enhance understanding of physical processes without collecting fine temporal in-situ data. While an individual realization of this downscaling approach may generate reasonable estimates of true high-frequency values, iterating analyses using an ensemble of realizations allows for uncertainties in generated time series to be propagated through subsequent modeling and tracer-based analyses. The method is sufficiently general and can be applied for a variety of applications to generate downscaled ensembles for use in meteorological and hydrometeorological models to evaluate model performance, investigate system processes across spatial scales and is additive to model-data fusion frameworks.

2.7 Acknowledgements

The authors acknowledge the support of the United States National Science Foundation (DEB-1802885, DEB-1802880 and AGS-1954660) and thank the anonymous reviewers for their time and effort spent reviewing this manuscript. The authors state no conflict of interest.

2.8 Data Availability Statement

Python code is provided in the *Supplemental Material* to generate geochemical synthetic time series based on the user's site-specific time series statistics. The code is intended to be easily adaptable to higher dimensions or other user specific applications. Additional materials can be made available upon request.

2.9 References

Abbott, B. W., V. Baranov, C. Mendoza-Lera, M. Nikolakopoulou, A. Harjung, T. Kolbe, M. N. Balasubramanian, T. N. Vaessen, F. Ciocca, A. Campeau, M. B. Wallin, P. Romeijn, M. Antonelli, J. Gonçalves, T. Datry, A. M. Laverman, J. de Dreuzy, D. M. Hannah, S. Krause, C. Oldham, and G. Pinay, 2016: Using multi-tracer inference to move beyond single catchment ecohydrology. *Earth-Sci. Rev.*, **160**, 19-42, https://doi.org/10.1016/j.earscirev.2016.06.014.

Aggarwal, P. K., O. A. Alduchov, K. O. Froehlich, L. J. Araguas-Araguas, N. C. Sturchio, and N. Kurita, 2012: Stable isotopes in global precipitation: a unified interpretation based on atmospheric moisture residence time. *Geophys. Res. Lett.,* **39***,* 1-6, https://doi.org/10.1029/2012GL051937.

Aggarwal, P. K., U. Romatschke, L. Araguas-Araguas, D. Belachew, F. J. Longstaffe, P. Berg, C. Schumacher, and A. Funk, 2016: Proportions of convective and stratiform precipitation revealed in water isotope ratios. *Nat. Geosci.*, **9**, 624-629, https://doi.org/10.1038/ngeo2739.

Allen, S. T., Jasechko, S., Berghuijs, W. R., Welker, J. M., Goldsmith, G. R., and Kirchner, J. W., 2019: Global sinusoidal seasonality in precipitation isotopes, *Hydrol. Earth Syst. Sci.*, **23**, 3423–3436, https://doi.org/10.5194/hess-23-3423-2019.

Allen, S. T., Kirchner, J. W., & Goldsmith, G. R., 2018. Predicting spatial patterns in precipitation isotope (δ2H and δ18O) seasonality using sinusoidal isoscapes. *Geophys. Res.*, **45**, 4859–4868, https://doi.org/10.1029/2018GL077458.

Bailey, A., E. Posmentier, and X. Feng, 2018: Patterns of Evaporation and Precipitation Drive Global Isotopic Changes in Atmospheric Moisture. *Geophy. Res. Lett.*, **45**, 7093-7101, https://doi.org/10.1029/2018GL078254.

Bárdossy, A. and G. G. S. Pegram, 2009: Copula based multisite model for daily precipitation simulation. *Hydrol. Earth Syst. Sci.,* **13***,* 2299-2314.

Benetti, M., G. Reverdin, C. Pierre, L. Merlivat, C. Risi, H. C. Steen-Larsen, and F. Vimeux, 2014: Deuterium excess in marine water vapor: Dependency on relative humidity and surface wind speed during evaporation. *J. Geophys. Res-Atmos.*, **119**, 583-593, https://doi.org/10.1002/2013JD020535.

Brady, E., Stevenson, S., Bailey, D., Liu, Z., Noone, D., Nusbaumer, J., Otto-Bliesner, B. L., Tabor, C., Tomas, R., Wong, T., et al., 2019: The Connected Isotopic Water Cycle in the Community Earth System Model Version 1. *J. Adv. Model. Earth Syst.*, **11**, 2547– 2566, https://doi.org/10.1029/2019MS001663.

Brooks, J. R., J. J. Gibson, S. J. Birks, M. H. Weber, K. D. Rodecap, and J. L. Stoddard, 2014: Stable isotope estimates of evaporation: inflow and water residence time for lakes across the United States as a tool for national lake water quality assessments. *Limnol. Oceanogr.,* **59**, 2150-2165, https://doi.org/10.4319/lo.2014.59.6.2150.

Bordoy, R. and P. Burlando, 2013: Stochastic downscaling of climate model precipitation outputs in orographically complex regions: 2. Downscaling methodology. *Water Resour. Res.,* **50***,* 562-579, https://doi.org/10.1002/wrcr.20443.

Bowen, G. J., Z. Cai, R. P. Fiorella, and A. L. Putman, 2019: Isotopes in the water cycle: Regional- to global-scale patterns and applications. *Annu. Rev. Earth Planet Sci.*, **47**, 453-479, https://doi.org/10.1146/annurev-earth-053018-060220.

Bowen, G. J. and S. P. Good, 2015: Incorporating water isotopes in hydrological and water resource investigations. *WIREs. Water*, **2**, *2*, 107-119. https://doi.org/10.1002/wat2.1069.

Celle-Jeanton, H. Y. Travi, and B. Blavoux, 2001: Isotopic typology of the precipitation in the Western Mediterranean region at three different time scales. *Geophys. Res. Lett.*, **28**, *7*, 1215-1218, https://doi.org/10.1029/2000GL012407.

Clow, D. W., M. A. Mast, and J. O. Sickman, 2018: Linking transit times to catchment sensitivity to atmospheric deposition of acidity and nitrogen in mountains of the western United States, *Hydrol. Process*, **32**, *16*, 2456–2470, https://doi.org/10.1002/hyp.13183.

Cong, R. and M. Brady, 2012: The interdependence between rainfall and temperature: copula analysis. *The Scientific World Journal,* **2012**, 1-11, https://doi.org/10.1100/2012/405675.

Conroy, J. L., Noone, D., Cobb, K. M., Moerman, J. W., and Konecky, B. L. (2016), Paired stable isotopologues in precipitation and vapor: A case study of the amount effect within western tropical Pacific storms, *J. Geophys. Res. Atmos.*, **121**, 3290– 3303, https://doi.org/10.1002/2015JD023844.

Coulibaly, P., Y. B. Dibike, and F. Anctil, 2005: Downscaling precipitation and temperature with temporal neutral networks. *J. Hydrometeor.,* **6***,* 483-496, https://doi.org/10.1175/JHM409.1.

Craig, H., 1961: Isotopic variations in meteoric waters. *Science*, **133**, 1702-1703.

Craig, H. and L. I. Gordon, 1965: Deuterium and oxygen-18 variations in the ocean and the marine atmosphere. *In E. Tongiorgi, ed*, Proceedings of a Conference on Stable Isotopes in Oceanographic Studies and Paleotemperatures, Spoleto, Italy, pp 9-130.

Dansgaard, W., 1964: Stable isotopes in precipitation. *Tellus*, **16**, 436–468, https://doi.org/10.1111/j.2153-3490.1964.tb00181.x.

D'Onofrio, D. 2014: Stochastic rainfall downscaling of climate models. *J. Hydrometeor.,***15**, 830-843, https://doi.org/10.1175/JHM-D-13-096.1.

Dutton, A., B. H. Wilkinson, J. M. Welker, G. J. Bowen, and K. C. Lohmann, 2005: Spatial distribution and seasonal variation in 18O/16O of modern precipitation and river water across the conterminous USA, *Hydrol. Process.*, **19**, *20*, 4121–4146, https://doi.org/10.1002/hyp.5876.

Ebtehaj, A. M., and E. Foufoula-Georgiou, 2013: On variational downscaling, fusion, and assimilation of hydrometeorological states: A unified framework via regularization. *Water Resour. Res.*, **49**, 5944– 5963, https://doi.org/10.1002/wrcr.20424.

Fekete, B. M., J. J. Gibson, P. Aggarwal, C. J. Vörösmarty, 2006: Application of isotopic tracers in continental scale hydrological modeling. *J. Hydrol.*, **330**, *3-4*, 444-456, https://doi.org/10.1016/j.jhydrol.2006.04.029.

Feng, X., A. M. Faiia, and E. S. Posmentier, 2009: Seasonality of isotopes in precipitation: A global perspective. *J. Geophys. Res-Atmos*, **114**, *D8*, https://doi.org/10.1029/2008JD011279.

v. Freyberg, J., S. T. Allen, S. Seeger, M. Weiler, and J. W. Kirchner, 2018: Sensitivity of young water fractions to hydroclimatic forcing and landscape properties across 22 Swiss catchments, *Hydrol. Earth Syst. Sci.*, 22, *7*, 3841–3861, https://doi.org/10.5194/hess-22-3841-2018.

Fröehlich K., J. J. Gibson, and P. K. Aggarwal, 2002: Deuterium excess in precipitation and its climatological significance. Study of environmental change using isotope techniques. *C&S Papers Series*, **13**, 54-65. International Atomic Energy Agency: Vienna, Austria.

Gallart, F., M. Valiente, P. Llorens, C. Cayuela, M. Sprenger, and J. Latron, 2020: Investigating young water fractions in a small Mediterranean mountain catchment: both precipitation forcing and sampling frequency matter. *Hydrol. Processes*, https://doi.org/10.1002/hyp.13806.

Gao, C., Y. Xu, Q. Zhu, Z. Bai, and L. Liu, 2018: Stochastic generation of daily rainfall events: a single-site rainfall model with copula-based joint simulation of rainfall characteristics and classification and simulation of rainfall patterns. *J. Hydrol,* **564**, 41-58, https://doi.org/10.1016/j.jhydrol.2018.06.073.

Gat, J. R., 1996: Oxygen and hydrogen isotopes in the hydrologic cycle. *Annu. Rev. Earth Planet Sci.*, **24**, 225-262, https://doi.org/10.1146/annurev.earth.24.1.225.

Gibson, J. J., T. W. D. Edwards, S. J. Birks, N. A. St Amour, W. M. Buhay, P. McEachern, B. B. Wolfe, and D. L. Peters, 2005: Progress in isotope tracer hydrology in Canada. *Hydrol. Process.*, **19***, 1*, 303-327, https://doi.org/10.1002/hyp.5766.

Goncu, S., and E. Albek, 2016: Statistical downscaling of meteorological time series and climatic projections in a watershed in Turkey. Theoretical and Applied Climatology, **126,** 1-2, https://link.gale.com/apps/doc/A470736525/AONE?u=s8405248&sid=AONE&xid=e894de9e.

Good S. P., D. V. Mallia, J. C. Lin, and G. J. Bowen, 2014: Stable isotope analysis of precipitation samples obtained via crowdsourcing reveals the spatiotemporal evolution of superstorm sandy. PLOS ONE **9**, *3*, e91117, https://doi.org/10.1371/journal.pone.0091117.

Good, S. P., D. Noone, and G. Bowen, 2015: Hydrologic connectivity constrains partitioning of global terrestrial water fluxes. *Science,* **349***,* 175-177, https://doi.org/10.1126/science.aaa5931.

Gupta, A., E. P. Gerber, and P. H. Lauritzen, 2020: Numerical impacts on tracer transport: A proposed intercomparison test of Atmospheric General Circulation Models. *Q. J. R. Meteorol. Soc.*, **146**, 3937– 3964, https://doi.org/10.1002/qj.3881.

Gyasi-Agyei, Y., 2011: Copula-based daily rainfall disaggregation model. *Water Resour. Res.,* **47***,* W07535, https://doi.org/10.1029/2011WR010519.

Halder, J., S. Terzer, L. I. Wassenaar, L. J. Araguás-Araguás, and P. K. Aggarwal, 2015: The Global Network of Isotopes in Rivers (GNIR): integration of water isotopes in watershed observation and riverine research. *Hydrol. Earth Syst. Sci.*, **19**, *8*, 3419–3431, https://doi.org/10.5194/hess-19-3419-2015.

Haslauer, C. P., P. Guthke, A. Bádossy, and E. A. Sudicky, 2012: Effects of non-gaussian copula-based hydraulic conductivity fields on macrodispersion. *Water Resour. Res.,* **48***,* 1-18, https://doi.org/10.1029/2011WR011425.

Hoffmann, G., J. Jouzel and V. Masson, 2000: Stable water isotopes in atmospheric general circulation models. *Hydrol. Processes,* **14**, 1385-1406, https://doi.org/10.1002/1099-1085(20000615)14:8<1385::AID-HYP989>3.0.CO2-1.

Huang, J., J. Zhang, Z. Zhang, S. Sun and J. Yao, 2012: Simulation of extreme precipitation indices in the Yangtze River basin by using statistical downscaling method (SDSM). *Theor. Appl. Climatol.* **108**, 325–343, https://doi.org/10.1007/s00704-011-0536-3.

IAEA/WMO (2020). Global Network of Isotopes in Precipitation. The GNIP Database. Accessible at: http://www.iaea.org/water.

Ingraham, N. L., 1998: Isotopic variations in precipitation. In C. Kendall & J. J. McDonnell (Eds.), Isotope Tracers in Catchment Hydrology (pp. 87–118). Amsterdam: Elsevier Science, https://doi.org/10.1016/B978-0-444-81546-0.50010-0.

Jacobs, S. R., E. Timbe, B. Weeser, M. C. Rufino, K. Butterbach-Bahl, and L. Breuer, 2018: Assessment of hydrological pathways in East African montane catchments under different land use. *Hydrol. Earth Syst. Sci.*, **22**, 4981-5000, https://doi.org/10.5194/hess-22-4981-2018.

Jasechko, S. and R. Taylor, 2015: Intensive rainfall recharges tropical groundwaters. *Environ. Res. Lett.,* **10***,* https://doi.org/10.1088/1748-9326/10/12/124015.

Jasechko, S., J. W. Kirchner, J. M. Welker, and J. J. McDonnell, 2016: Substantial proportion of global streamflow less than three months old. *Nat. Geosci.*, **9**, *2*, 126–129, https://doi.org/10.1038/ngeo2636.

Kanner, L. C., N. H. Buenning, L. D. Stott, A. Timmermann, and D. Noone, 2014: The role of soil processes in $\delta^{18}O$ terrestrial climate proxies. *Global Biogeochem. Cycles,* **28**, 239-252, https://doi.org/10.1002/2013GB004742.

Kendall, C. and J. J. McDonnell, 2012: *Isotope tracers in catchment hydrology*. Elsevier, 870pp.

Khedun, C. P., A. K. Mishra, V. P. Singh and J. R. Giardino, 2014: A copula-based precipitation forecasting model: investigating the interdecadal modulation of ENSO's impacts on monthly precipitation. *Water Resour. Res.,* **50***,* 580-600, https://doi.org/10.1002/2013WR013763.

Kirchner, J. W., 2016a: Aggregation in environmental systems—Part 1: Seasonal tracer cycles quantify young water fractions, but not mean transit times, in spatially heterogeneous catchments. *Hydrol. Earth Syst. Sci.*, 20, *1*, 279–297, https://doi.org/10.5194/hess-20-279-2016.

Kirchner, J. W., 2016b: Aggregation in environmental systems—Part 2: Catchment mean transit times and young water fractions under hydrologic nonstationarity. *Hydrol. Earth Syst. Sci.*, **20**, *1*, 299–328, https://doi.org/10.5194/hess-20-299-2016.

Konecky, B. L., D. C. Noone, and K. M. Cobb, 2019: The influence of competing hydroclimate processes on stable isotope ratios in tropical rainfall. *Geophys. Res. Lett.*, **46**, 1622-1633, https://doi.org/10.1029/2018GL080188.

Krause, P., D. P. Boyle, and F. Bäse, 2005: Comparison of different efficiency criteria for hydrological model assessment. *Adv. in Geosci.,* **5***,* 89-97, https://doi.org/1680-7359/adgeo/2005-5-89.

Kuhn, G., S. Khan, A. R. Ganguly, and M. L. Branstetter, 2007: Geospatial-temporal dependence among weekly precipitation extremes with applications to observations and climate model simulations in South America. *Adv. Water Resour.,* **30***,* 2401-2423, https://doi.org/10.1016/j.advwatres.2007.05.006.

Laux, P., S. Vogl, W. Qiu, H. R. Knoche, and H. Kunstmann, 2011: Copula-based statistical refinement of precipitation in RCM simulations over complex terrain. *Hydrol. Earth Sys. Sci.,* **15***,* 2401-2419, https://doi.org/10.5194/hess-15-2401-2011.

Laux, P., S. Wagner, A. Wagner, J. Jacobeit, A. Bárdossy, and H. Kunstmann, 2009: Modelling daily precipitation features in the Volta Basin of West Africa. *International Journal of Climatology,* **29***,* 937-954, https://doi.org/10.1002/joc.1852.

Lee, J. E. and I. Fung, 2008: "Amount effect" of water isotopes and quantitative analysis of post-condensation processes. *Hydrol. Process*., **22**, 1-8, https://doi.org/10.1002/hyp.6637.

Lutz, S. R., R. Krieg, C. Müller, M. Zink, K. Knöller, L. Samaniego, and R. Merz, 2018: Spatial patterns of water age: Using young water fractions to improve the characterization of transit times in contrasting catchments. *Water Resour. Res.*, **54**, *7*, 4767–4784, https://doi.org/10.1029/2017WR022216.

McGuire, K. J. and J. J. McDonnell, 2006: A review and evaluation of catchment transit time modeling. *J. Hydrol.,* **330***,* 543-563, https://doi.org/10.1016/j.jhydrol.2006.04.020.

Moerman, J. W., K. M. Cobb, J. F., Adkins, H. Sodemann, B. Clark, and A. A. Tuen, 2013: Diurnal to interannual rainfall $\delta^{18}O$ variations in northern Borneo driven by regional hydrology. *Earth Planet. Sci. Lett.,* **369-370***,* 108-109, https://doi.org/10.1016/j.epsl.2013.03.014.

Moore, M., Kuang, Z., and Blossey, P. N., 2014: A moisture budget perspective of the amount effect, *Geophys. Res. Lett*., **41**, 1329– 1335, https://doi.org/10.1002/2013GL058302.

Moore, M., P. N. Blossey, A. Muhlbauer, and Z. Kuang, 2016: Microphysical controls on the isotopic composition of wintertime orographic precipitation. *J. Geophys. Res. Atmos.*, **121**, 7235- 7253, https://doi.org/10.1002/2015JD023763.

Nusbaumer, J., T. E. Wong, C. Bardeen, and D. Noone, 2017: Evaluating hydrological processes in the Community Atmosphere Model Version 5 (CAM5) using stable isotope ratios of water. *J. Adv. Model Earth Sy.*, **9**, *2*, 949-977, https://doi.org/10.1002/2016MS000839.

Orbe, C., D. Rind, J. Jonas, L. Nazarenko, G. Faluvegi, L. T. Murray, D. T. Shindell, K. Tsigaridis, T. Zhou, M. Kelley, and G. A. Schmidt, 2020: GISS Model E2.2: A climate model optimized for the middle atmosphere—2. Validation of large-scale transport and evaluation of climate response. *J. Geophys. Res. Atmos*., **125**, https://doi-org.ezproxy.proxy.library.oregonstate.edu/10.1029/2020JD033151.

Pfahl, S. and H. Sodemann, 2014: What controls deuterium excess in global precipitation?. *Clim. Past*, **10**, 771–781, https://doi.org/10.5194/cp-10-771-2014.

Poduje, A. C. C. and U. Haberlandt, 2017: Short time step continuous rainfall modeling and simulation of extreme events. *J. Hydrol.,* **552***,* 182-197, https://doi.org/10.1016/j.jhydrol.2017.06.036.

Remondi, F., J. W. Kircher, P. Burlando, and S. Fatichi, 2018: Water flux tracking with a distributed hydrologic model to quantify controls on the spatio-temporal variability of transit time distributions. *Water Resour. Res.*, **54**, *4*, 3081-3099, https://doi.org/10.1002/2017WR021689.

Risi, C., D. Noone, J. Worden, C. Frankenberg, G. Stiller, M. Kiefer, B. Funke, K. Walker, P. Bernath, M. Schneider, D. Wunch, V. Sherlock, N. Deutscher, D. Griffith, P. O. Wennberg, K. Strong, D. Smale, E. Mahieu, S. Barthlott, F. Hase, O. García, J. Notholt, T. Warneke, G. Toon, D. Sayres, S. Bony, J. Lee, D. Brown, R. Uemura, C. Sturm, 2012: Process-evaluation of tropospheric humidity simulated by general circulation models using water vapor isotopic observations: 2. Using isotopic diagnostics to understand the mid and upper tropospheric moist bias in the tropics and subtropics, *J. Geophys. Res.*, **117**, *D05304*, https://doi.org/10.1029/2011JD016623.

Risi, C., S. Bony, S., and F. Vimeux, 2008: Influence of convective processes on the isotopic composition (δ18O and δD) of precipitation and water vapor in the tropics: 2. Physical interpretation of the amount effect. *J. Geophys. Res.*, **113**, D19306, https://doi.org/10.1029/2008JD009943.

Rosa, D., Lamarque, J. F., and Collins, W. D. 2012: Global transport of passive tracers in conventional and superparameterized climate models: Evaluation of multi-scale methods, *J. Adv. Model. Earth Syst.*, **4**, https://doi.org/10.1029/2012MS000206.

Rozanski, K., Araguás-Araguás, L. and Gonfiantini, R. 1993: Isotopic Patterns in Modern Global Precipitation. *In Climate Change in Continental Isotopic Records* (eds P.K. Swart, K.C. Lohmann, J. Mckenzie and S. Savin). https://doi.org/10.1029/GM078p0001.

Schölzel, C. and P. Friederichs, 2008: Multivariate non-normally distributed random variables in climate research- introduction to the copula approach. *Nonlinear Processes in Geophysics,* **15***,* 761-772. https://doi.org/10.5194/npg-15-761-2008.

Schneider, M. and F. Ramos, 2014: Transductive learning for multi-task copula processes. *Technical Report*, 1-8, http://www-personal.usyd.edu.au/~framos/Publications_files/TransductiveCopulas.pdf.

Sklar, A., 1959: Fonctions de répartition à n dimensions et leurs marges. *Publ. Inst. Stat. Univ. Paris,* **8**, 229–231.

So, B., J. Kim, H. Kwon, and C. H. R. Lima, 2017: Stochastic extreme downscaling model for an assessment of changes in rainfall intensity-duration-frequency curves over South Korea using multiple regional climate models. *J. Hydrol.,* **553**, 321-337, https://doi.org/10.1016/j.hydrol.2017.07.061.

Soderberg, K., S. P. Good, L. Wang, and K. Caylor, 2012: Stable isotopes of water vapor in the vadose zone: a review of measurement and modeling techniques. *Vadose Zone J*, https://doi.org/10.2136/vzj2011.0165.

Song, C., G. Wang, G. Liu, T. Mao, X. Sun, and X. Chen, 2016: Stable isotope variations of precipitation and streamflow reveal the young water fraction of a permafrost watershed. *Hydrol. Processes*, **31**, *4*, 935–947, doi:10.1002/hyp.11077.

Sprenger, M., C. Stumpp, M. Weiler, W. Aeschbach, S. T. Allen, P. Benettin, M. Dubbert, A. Hartmann, M. Hrachowitz, J. W. Kirchner, J. J. McDonnell, N. Orlowski, D. Penna, S. Pfahl, M. Rinderer, N. Rodriquez, M. Schmidt, and C. Werner, 2019: The demographics of water: A review of water ages in the critical zone. *Rev. of Geophysics*, **57**, 800-834, https://doi.org/10.1029/2018RG000633.

Steen-Larsen, H. C., C. Risi, M. Werner, K. Yoshimura, and V. Masson-Delmotte, 2017: Evaluating the skills of isotope-enabled general circulation models against in situ atmospheric water vapor isotope observations, *J. Geophys. Res. Atmos.*, **122**, 246–263, https://doi.org/10.1002/2016JD025443.

Stumpp, C., J. Klaus, and W. Stichler, 2014: Analysis of long-term stable isotopic composition in German precipitation. *J. Hydrol.,* **517**, 351-361, https://doi.org/10.1016/j.jhydrol.2014.05.034.

Stumpp, C., W. Stichler, M. Kandolf, and J. Šimunek, 2012: Effects of land cover and fertilization method on water flow and solute transport in five lysimeters: a long-term study using stable water isotopes. *Vadose Zone J.,* https://doi.org/10.2136/vzj2011.0075.

Tharammal, T., Bala, G., and Noone, D., 2017: Impact of deep convection on the isotopic amount effect in tropical precipitation, *J. Geophys. Res. Atmos.*, **122**, 1505– 1523, http://dx.doi.org/10.1002/2016JD025555.

Turnadge, C. and B. D. Smerdon, 2014: A review of methods for modelling environmental tracers in groundwater: Advantages of tracer concentration simulation. *J. Hydrol.*, **519**, http://dx.doi.org/10.1016/j.jhydrol.2014.10.056.

Vachon, R. W., J. W. C. White, E. Gutmann, and J. M. Welker, 2007: Amount-weighted annual isotopic (δ18O) values are affected by the seasonality of precipitation: A

sensitivity study. *Geophys. Res. Lett.*, **34**, *21*, L21707, doi:10.1029/2007GL030547.

West, J. B., G. J. Bowen, T. E. Dawson, and K. P. Tu, 2010: *Isoscapes: Understanding movement, pattern, and process on Earth through isotope mapping*. Springer, 487pp.

Wiederhold, J. G., 2015: Metal stable isotope signatures as tracers in environmental geochemistry. *Environ. Sci. Technol.*, **49**, 2606-2624, https://doi.org/10.1021/es504683e.

Wilkinson, B. H. and L. C. Ivany, 2002: Paleoclimatic inference from stable isotope profiles of accretionary biogenic hardparts – a quantitative approach to the evaluation of incomplete data, *Palaeogeogr. Palaeoclimatol. Palaeoecol.*, **185**, *1*, 95–114, https://doi.org/10.1016/S0031-0182(02)00279-1.

Wong, T. E., J. Nusbaumer, and D. C. Noone, 2017: Evaluation of modeled land-atmosphere exchanges with a comprehensive water isotope fractionation scheme in version 4 of the Community Land Model. *J. Adv. Model Earth Sy.*, **9**, *2*, 978-1001, https://doi.org/10.1002/2016MS000842.

Yang, W., A. Bárdossy, and H. J. Caspary, 2010: Downscaling daily precipitation time series using a combined circulation- and regression-based approach. *Theor. Appl. Climatol*, **102**, 439-454, https://doi.org/10.1007/s00704-010-0272-0.

2.10 Supplemental Material

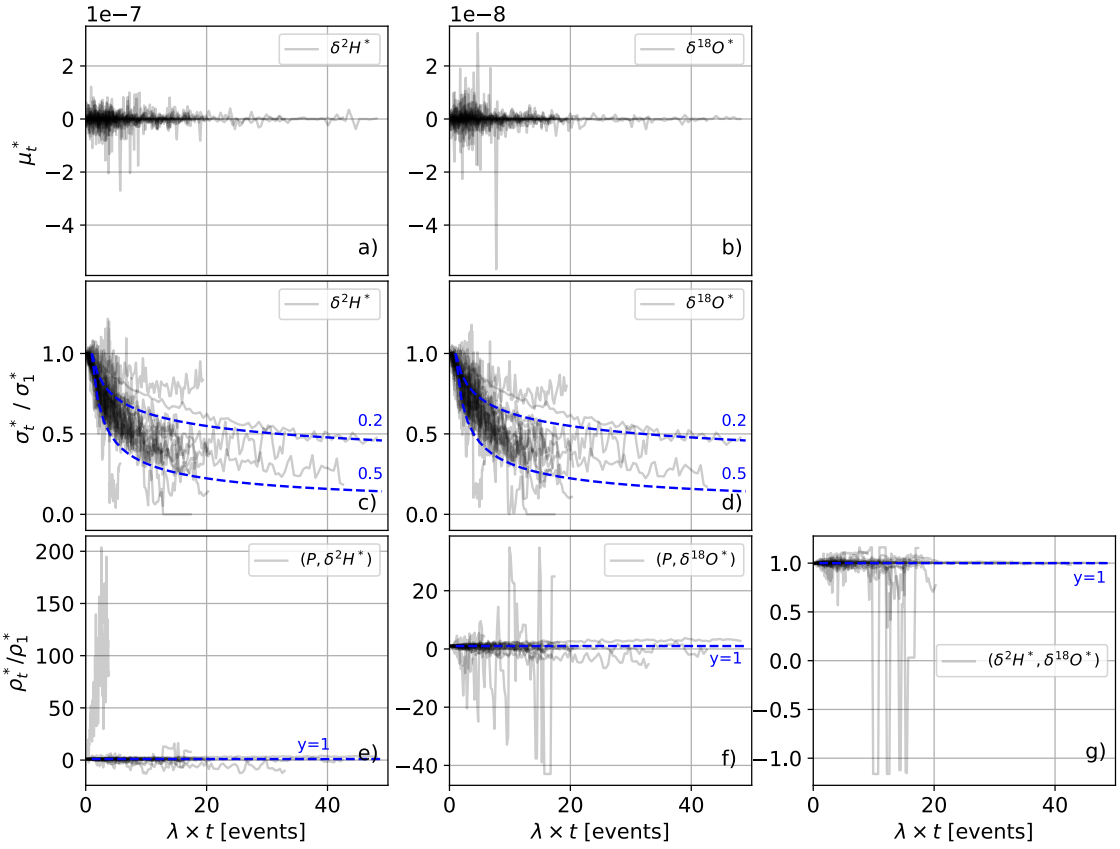

Figure 2.S1. The x-axis is $\boldsymbol{\lambda}$ (recorded precipitation events / number of days in the time series) multiplied by daily to 12-week aggregation intervals (days) and the y-axes were the deviations for each of the 27 sites in their stochastic time series a,b) means ($\boldsymbol{\mu_t^*}$; note the scale of the y-axis), c,d) standard deviations at *t*-day ($\boldsymbol{\sigma_t^*}$) divided by the daily standard deviation ($\boldsymbol{\sigma_1^*}$) with blue dashed lines at $(\boldsymbol{\lambda n})^{\mathbf{0.5}}$ and $(\boldsymbol{\lambda n})^{\mathbf{0.2}}$, and e-g) Pearson correlation coefficients at *t*-day divided by daily ($\boldsymbol{\rho_t^*/\rho_1^*}$) with blue dashed lines at y-axis = 1. This figure corresponds to Figure 2 in the text.

(i) Definition of a Gaussian Copula

To define a copula for a random vector $(X_1, X_2, \ldots, X_z)$, the marginal CDFs $F_i(x) = \Pr[X_z \leq x]$ are assumed to be continuous functions. The probability integral transform can be applied to each vector component and the resulting random vector $(U_1, U_2, \ldots, U_z) = (F_1(X_1), F_2(X_2), \ldots, F_z(X_z))$ has uniformly distributed marginals. The copula of

$(X_1, X_2, \dots, X_z)$ is defined by the joint cumulative distribution function of $(U_1, U_2, \dots, U_z)$. The copula fully describes the dependence structure between the components of $(X_1, X_2, \dots, X_z)$ and the marginal CDFs, F_z, describe the marginal distributions. By applying the inverse to the above process, pseudo-random samples can be generated from general classes of multivariate probability distributions. Explicitly, a sample $(\boldsymbol{x} = x_1, x_2, \dots, x_i)$ is constructed from a uniformly distributed marginal vector $(\boldsymbol{u} = u_1, u_2, \dots, u_i)$ as

$$(x_1, x_2, \dots, x_i) = (F_1^{-1}(u_1), F_2^{-1}(u_2), \dots, F_i^{-1}(u_i)). \qquad \text{Eq. 5}$$

F_i^{-1} are the inverses of the CDFs of each variable, which are unproblematic because the F_i are assumed to be continuous and known. The copula relates the multivariate CDFs of *i* variables to their principal univariate distributions and provides the flexibility of using different probability distribution functions for each variable. Since the copula reflects the original data's dependency structure, its construction is solely related to the relationship between the variables, thus providing freedom in the choice of univariate marginal distributions. For more information on copulas and their utility, refer to Gyasi-Agyei 2011, Khedun et al. 2014, Renard and Lang 2006, and Bárdossy and Pegram 2009, among others. Assuming a Gaussian copula and a three-variable case (here precipitation amount (P), δ^2H^* and $\delta^{18}O^*$), the mean ($\boldsymbol{\mu}$) and covariance matrices ($\boldsymbol{\Sigma}$) of the unconditioned Gaussian copula are specified as

$$\boldsymbol{\mu} = \begin{bmatrix} 0 \\ 0 \\ 0 \end{bmatrix}$$

with size *n*=3 by 1, and

$$\boldsymbol{\Sigma} = \begin{bmatrix} 1 & \rho_{12} & \rho_{13} \\ \rho_{21} & 1 & \rho_{23} \\ \rho_{31} & \rho_{32} & 1 \end{bmatrix}$$

with size 3 by 3 where the values of ρ are the site-specific estimated daily correlation coefficients ($\hat{\rho}_1^*$). A conditional Gaussian can be defined within the generic Gaussian copula framework above. If a *i*-dimensional matrix, **x**, is partitioned conditioned on

knowledge of $i - q$ pieces of information, where q is the dimension of the unknown information, then

$$\mathbf{x} = \begin{bmatrix} \mathbf{x}_1 \\ \mathbf{x}_2 \end{bmatrix} \text{ with sizes } \begin{bmatrix} q \times 1 \\ (i-q) \times 1 \end{bmatrix} \qquad \text{Eq. 6}$$

, where $\mathbf{x_1}$ is the unknown values (here isotope ratios) and $\mathbf{x_2}$ is the known values (here precipitation). Then, $\boldsymbol{\mu}$ and $\boldsymbol{\Sigma}$ are partitioned as

$$\boldsymbol{\mu} = \begin{bmatrix} \boldsymbol{\mu}_1 \\ \boldsymbol{\mu}_2 \end{bmatrix} \text{ with sizes } \begin{bmatrix} q \times 1 \\ (i-q) \times 1 \end{bmatrix} \qquad \text{Eq. 7a}$$

$$\boldsymbol{\Sigma} = \begin{bmatrix} \boldsymbol{\Sigma}_{11} & \boldsymbol{\Sigma}_{12} \\ \boldsymbol{\Sigma}_{21} & \boldsymbol{\Sigma}_{22} \end{bmatrix} \text{ with sizes } \begin{bmatrix} q \times q & q \times (i-q) \\ (i-q) \times q & (i-q) \times (i-q) \end{bmatrix}, \qquad \text{Eq. 8a}$$

where $\boldsymbol{\mu}$ are the means and $\boldsymbol{\Sigma}$ are the standard deviations. When a multivariate Gaussian copula is used, the distribution of $\mathbf{x_1}$, conditional on $\mathbf{x_2} = j$ is also a multivariate Gaussian $(\mathbf{x_1} \mid \mathbf{x_2} = j) \sim N(\bar{\boldsymbol{\mu}}, \bar{\boldsymbol{\Sigma}})$ where

$$\bar{\boldsymbol{\mu}} = \boldsymbol{\Sigma}_{12}\boldsymbol{\Sigma}_{22}^{-1} \cdot j. \qquad \text{Eq. 7b}$$

Above, j is equal to the conditioned values and the covariance matrix is

$$\bar{\boldsymbol{\Sigma}} = \boldsymbol{\Sigma}_{11} - \boldsymbol{\Sigma}_{12}\,\boldsymbol{\Sigma}_{22}^{-1}\,\boldsymbol{\Sigma}_{21}. \qquad \text{Eq. 8b}$$

In our three-variable case, when conditioning on precipitation amount (P) this simplifies to:

$$\bar{\boldsymbol{\mu}}_{\boldsymbol{i}} = \begin{bmatrix} \hat{\rho}_1^*(P, \delta^2 H^*)\, j_i \\ \hat{\rho}_1^*(P, \delta^{18} O^*)\, j_i \end{bmatrix} \qquad \text{Eq. 9}$$

and

$$\bar{\boldsymbol{\Sigma}}_{\boldsymbol{\iota}} = \begin{bmatrix} 1 - \hat{\rho}_1^*(P, \delta^2H^*)\hat{\rho}_1^*(P, \delta^2H^*) & \hat{\rho}_1^*(\delta^2H^*, \delta^{18}O^*) - \hat{\rho}_1^*(P, \delta^2H^*)\hat{\rho}_1^*(P, \delta^{18}O^*) \\ \hat{\rho}_1^*(\delta^2H^*, \delta^{18}O^*) - \hat{\rho}_1^*(P, \delta^{18}O^*)\widehat{\rho_1^*}(P, \delta^2H^*) & 1 - \hat{\rho}_1^*(P, \delta^{18}O^*)\hat{\rho}_1^*(P, \delta^{18}O^*) \end{bmatrix}$$

, Eq. 10

where j_i is equal to a daily precipitation value p_i minus the precipitation mean (μ_p) divided by its standard deviation (σ_p) as $j_i = (p_i - \mu_p)/\sigma_p$.

For each observed precipitation amount, a 2-number sample (c_i) representing the stochastic signal was drawn from a multivariate Gaussian (MG) distribution using Python's (v3.7.6) SciPy Library (v1.2.1) with parameters of $\bar{\mu}_\iota$ and $\bar{\Sigma}_\iota$ (i.e. $c_i \sim N(\bar{\mu}_\iota, \bar{\Sigma}_\iota)$; Eq. 9 and 10). Next, Gaussian CDF values (u_i) were calculated for each of the generated series, as $u_i = F(c_i)$. Note, each sample of u_i consists of two numbers which are uniformly distributed between 0 and 1 with a specified covariance and conditioned on that day's precipitation. Next, each uniform value (u_i) was used to resample from the *n*-day empirical distribution of isotope ratios for each site, formed by the deseasonalized time series values of δ^2H^* and $\delta^{18}O^*$. Each of these values was then rescaled by $\hat{\sigma}_1^*/\sigma_t^*$. The resulting stochastic time series were site-specific synthetic daily δ^2H^* and $\delta^{18}O^*$ values conditioned on observed precipitation amounts with means of zero, standard deviations of $\hat{\sigma}_1^*$ and Pearson correlation coefficients of $\hat{\rho}_1^*$.

(ii) Downscaling Methodology Applied to a Biweekly Precipitation, δ^2H, and $\delta^{18}O$ Time Series

Below is an overview of the methodology and its application for generating downscaled tracer time series. The daily dataset from Piracicaba, Brazil (Table S1) was aggregated to biweekly time scales and the downscaling method was applied to generate a daily time series conditioned on known daily precipitation amounts.

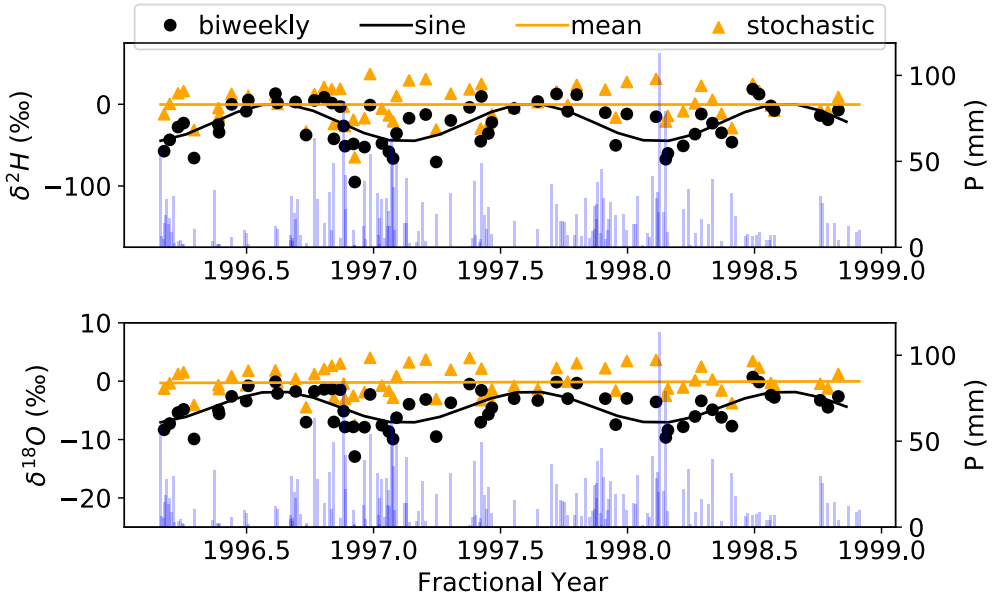

Figure 2.S2a. Step 1) Define and remove the deterministic (seasonal) time series component from the observed biweekly tracer time series (*Section 2.c.1* in the text). Here the biweekly observations, estimated sinusoidal function, stochastic time series and the mean of the stochastic time series are shown.

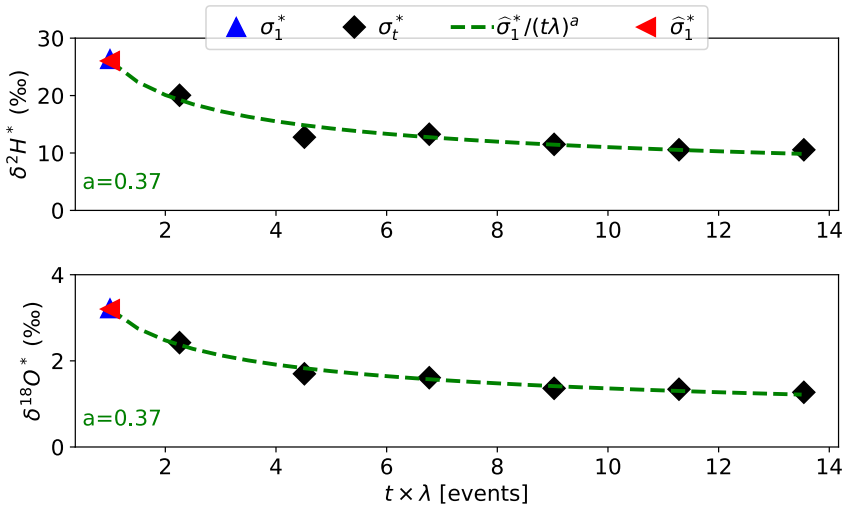

Figure 2.S2b. Step 2) Estimate the daily stochastic signal statistics by utilizing a power law relationship and the observed correlation structures (*Section 2.c.2* in the text). Here the observed stochastic daily standard deviation (σ_1^*), observed *t*-day standard deviations (σ_t^*), the power-law function (Eq. 4) and the estimated daily standard deviation ($\hat{\sigma}_1^*$) are shown.

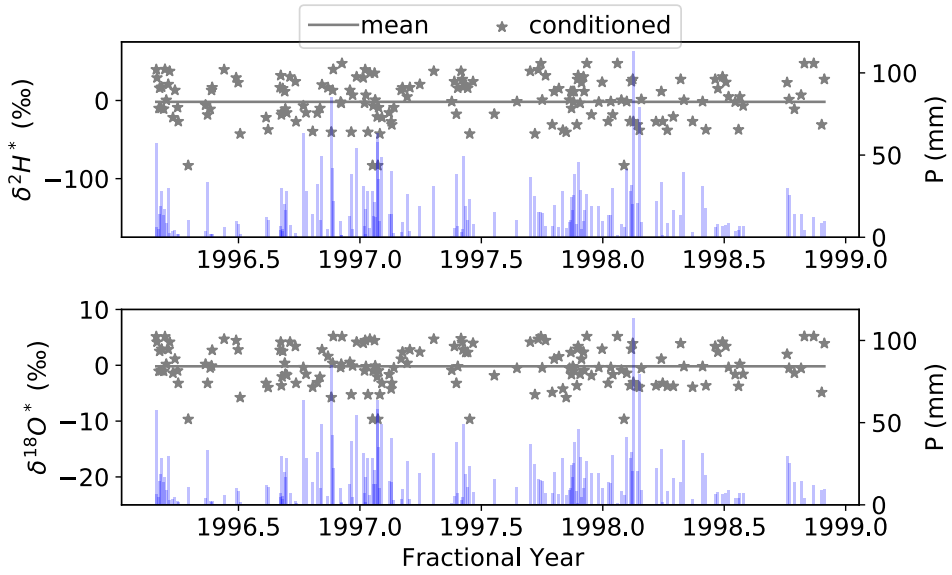

Figure 2.S2c. Step 3) Generate conditioned values using relevant covariates and the estimated daily stochastic signal statistics from Step 2 (*Section 2.c.2* in the text). The downscaled stochastic time series conditioned on daily precipitation amounts and its mean are shown.

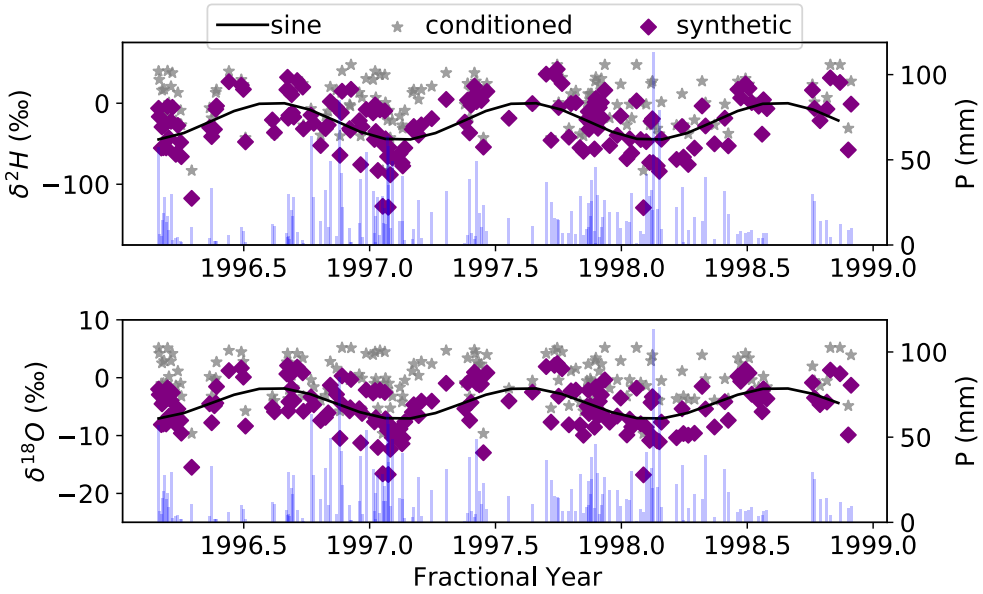

Figure 2.S2d. Step 4a) Produce final synthetic time series by adding the deterministic component from Step 1 to the stochastic realizations from Step 3 (*Section 2.c.3* in the text). Here the sinusoidal function, downscaled stochastic time series conditioned on daily precipitation amounts, and downscaled synthetic time series, which is the stochastic series plus the sinusoidal function, are shown.

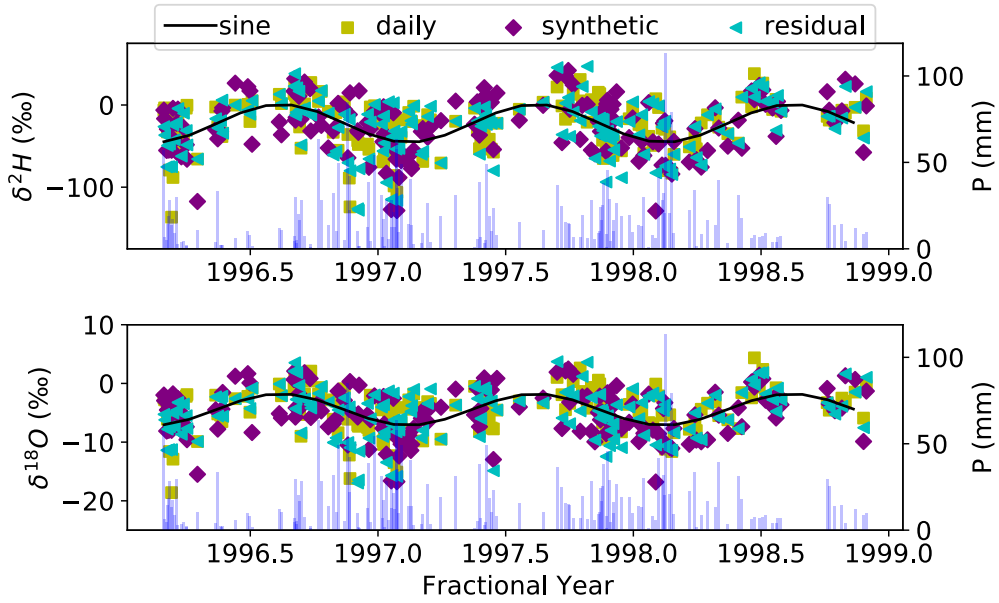

Figure 2.S2e. Step 4b) Apply a residual correction on the final synthetic time series (*Section 2.c.3* in the text). Here the sinusoidal function, observed daily time series, downscaled synthetic time series and residual corrected downscaled synthetic time series are shown.

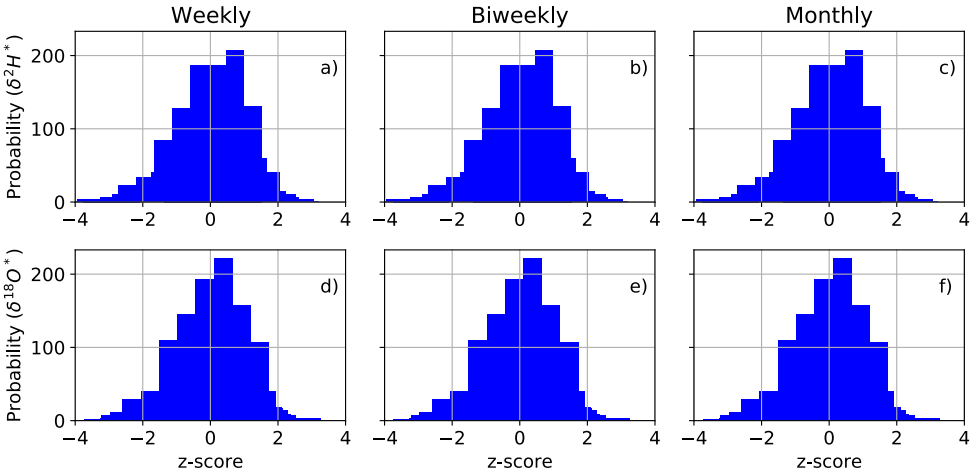

Figure 2.S3. Histograms of all 27 site's stochastic signal z-scores ($= \frac{\boldsymbol{x-\mu}}{\boldsymbol{\sigma}}$; where x is δ^2H^* or $\delta^{18}O^*$, $\boldsymbol{\mu}$ is the mean, and $\boldsymbol{\sigma}$ is the standard deviation) at weekly (a,b), biweekly (b,e) and monthly (c,f) time scales. The Shapiro-Wilk and the D'Agostino's K2 normality tests suggest that we could not reject the assumption of normality in the weekly, biweekly and monthly time series (p-value > 0.05).

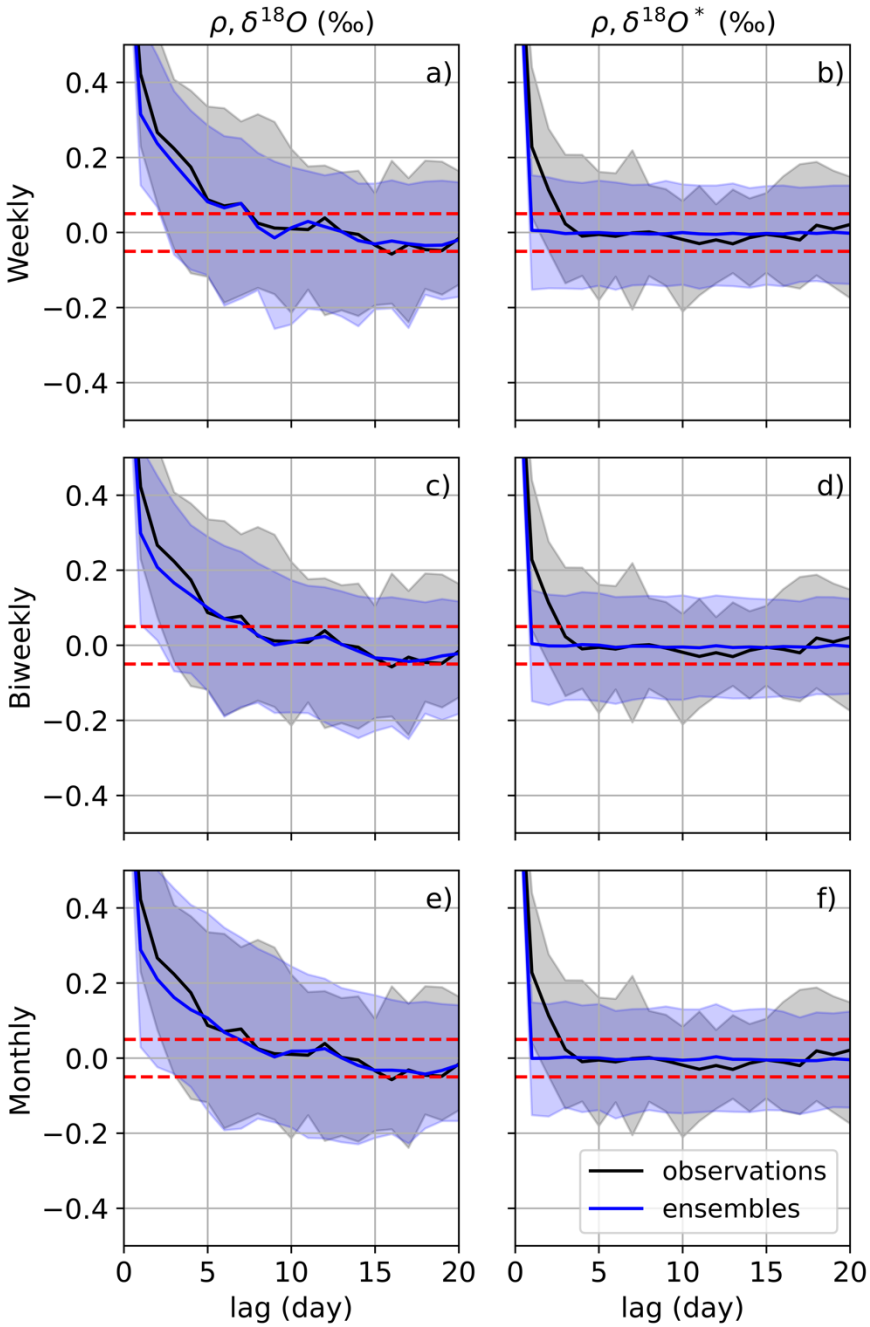

Figure 2.S4. a,c,e) Median autocorrelation of the observed daily $\delta^{18}O$ datasets and the daily residual corrected ensembles (solid lines). b,d,f) Median autocorrelations of the $\delta^{18}O^*$ stochastic signals for the observations and the downscaled ensembles. The 5th to 95th percentiles of the observed and ensemble correlations are represented as shaded regions. Horizontal red dashed line indicates where ρ is +/-5%.

Python Code:

```
#!/usr/bin/env python3
# -*- coding: utf-8 -*-
"""
@author: Catie Finkenbiner
"""
import numpy as np
import scipy as sp


## Use prediction to create conditional copula generated
values
def main(tsP,xday_stats,H_scale,O_scale):

    '''
    See Section 2.c of Manuscript

    tsP: observed precipitation time series
    xday_stats: n-day statistics matrix
        [[P_mean, H_mean, O_mean],
        [P_std, H_std, O_std],
        [rho_PH, rho_PO, rho_HO]]
```

```
    H_scale: sorted d2H stochastic time series component
multiplied by the estimated
        1-day standard deviation and divided by the standard
deviation of the n-day
        d2H stochastic series (hat{sigma_1}/sigma_n)

    O_scale: sorted d18O stochastic time series component
multiplied by the estimated
        1-day standard deviation and divided by the standard
deviation of the n-day
        d18O stochastic series (hat{sigma_1}/sigma_n)

    returns an isotope time series conditioned on tsP
    '''

    # Observed P statistics
    Pmu = np.mean(tsP)
    Psig = np.std(tsP)

    # Correlation Coefficients
    xday_rho1 = xday_stats[2,0] ; xday_rho2 = xday_stats[2,1]
; xday_rho3 = xday_stats[2,2]
```

```
    # Calculate Sigma_bar
    sigma_bar = [[1 - xday_rho1*xday_rho1, xday_rho3 -
xday_rho1*xday_rho2],
                 [xday_rho3 - xday_rho1*xday_rho2, 1 -
xday_rho2*xday_rho2]]

    series = []
    for i in np.arange(len(tsP)):
        a = (tsP[i] - Pmu) / Psig
        H2mu_bar = xday_rho1 * a
        O18mu_bar = xday_rho2 * a
        mu_bar = np.array([H2mu_bar,O18mu_bar])

        X      =      sp.stats.multivariate_normal.rvs(mean=
mu_bar,cov= sigma_bar)
        X2 = sp.stats.norm.cdf(X[0],loc=0,scale=1)
        X3 = sp.stats.norm.cdf(X[1],loc=0,scale=1)

        index = int(np.floor(X2 * len(H_scale)))
        newH = H_scale[index]

        index = int(np.floor(X3 * len(O_scale)))
        newO = O_scale[index]
```

```
            series.append([newH,newO])
        return series


if __name__ == '__main__':
    main(tsP,xday_stats,H_scale,O_scale)
```

Chapter 3. A Physical Basis for Ecohydrological Separation: The roles of soil hydraulics and climate

3.1 Abstract

The degree of water mixing in the critical zone is under intense debate. Field measurements of isotope ratios indicate varying degrees of separation between pools of water that supply streams and vegetation. The exact physical mechanisms behind ecohydrologic separation are unknown, but local conditions such as soil heterogeneities likely influence the extent of mixing and separation of subsurface water pools. Using a well-established soil physics model, we simulated if isotopic separations occur within 650 distinct configurations of soil properties, climatologies, and mobile/immobile soil-water domains. Simulations demonstrated separations in isotope ratios between storage and drainage waters during periods of high precipitation, soil water content, and drainage. Separations grew with larger immobile domains and, to a lesser extent, higher mobile-immobile transfer rates. Across soil types and climates, lower saturated hydraulic conductivity and higher rainfall rates amplified isotopic differences, illustrating how mobile and immobile domains interact with local conditions to physically result in subsurface separations. These results show how different critical-zone solute fluxes can be generated by representing contrasting transport dynamics in distinct domains across a range of soils and climate conditions.

3.2 Introduction

Observations of water from soils, plants, and streamflow are geochemically disparate, as was first shown by Brooks et al. (2010) and further explored in subsequent studies (Radolinski et al., 2021; Sprenger et al., 2019; McDonnell et al., 2014; Stumpp et al., 2009; Sprenger et al., 2016). These results conflict with traditional hydrologic assumptions where soil layers are well-mixed water reservoirs wherein new precipitation completely mixes with previously stored water before seeping downward or being

absorbed by roots for transpiration. Separations (i.e., differences) in tracer concentrations have specifically been reported among water traveling through preferential flow paths, water residing and tightly held within a soil matrix, and water discharged as drainage across various soil types (Radolinski et al., 2021; Barbeta et al., 2020; Berry et al., 2018; Dubbert et al., 2019; Maloszewski et al., 2006; Vargas et al., 2017) and climates (Brooks et al., 2010; Sprenger et al., 2019; Chen et al., 2020; Mueller et al., 2014; Stumpp and Hendry, 2012). Stable water isotopes ratios of hydrogen ($^{2}H/^{1}H$) and oxygen ($^{18}O/^{16}O$), hereafter communicated as $\delta^{2}H$ and $\delta^{18}O$, in precipitation, soil water, and plant root extracts have been utilized as tracers to investigate transport and so-called ecohydrological separations in soils (Radolinski et al., 2021; Sprenger et al., 2019; McDonnell 2014; Stumpp et al., 2009; Sprenger et al., 2016). Separate from those observational studies of isotopic differences between pools, new theoretical frameworks have shown how flow through systems composed of contrasting conductivities will support transport dynamics that lead to separations between storages and fluxes (McDonnell, 2014; Sprenger and Allen, 2020; Berghuijs and Kirchner, 2017). We expand on these frameworks previously applied to individual sites and case studies to explore, more generally, how ecohydrological separation caused by transport heterogeneity in soils can be expected to vary across soils and climates.

One of the difficulties of modeling observed separations is that traditional hydrologic modeling approaches fail to account for heterogeneous mixing and transport processes by assuming incoming precipitation enters the soil matrix and mixes fully with pre-existing soil water. Several numerical modeling studies have attempted to represent separations arising in soils (e.g., Cain et al., 2019; Knighton et al., 2020; Stumpp and Maloszewski, 2010; Sprenger et al., 2015; Sprenger et al., 2016; Sprenger et al., 2018; Hu et al., 2018), with these studies advancing understanding of subsurface mixing by quantifying flow heterogeneities in the unsaturated zone and the spatiotemporal variability of water and solute transport. Sprenger et al. (2018) investigated separations between soil water pools using a one-dimensional flow model at three long-term northern latitude research sites and found modeling with two pore domains improved the representation of soil water isotope dynamics when compared to field measurements. We

expand on this work by utilizing a fully mechanistic modeling approach to examine how separation phenomena arise across a wide range of soil hydraulic parameters or climate conditions to address which environmental conditions do (or do not) lead to the separation phenomena that have been observed (Brooks et al., 2010; Berghuijs and Kirchner, 2017; Evaristo et al., 2015) to be intrinsic to soil-water flow.

We configured 650 geochemically enabled soil physics models (HYDRUS-1D; Šimünek et al., 2013; Stumpp et al., 2012) to evaluate soil water transport and mixing across a range of soil types and with simulated precipitation from different climates. This approach explicitly allowed for heterogeneous mixing of solutes at depth via a dual-porosity method. Specifically, our research objective was to test how pore heterogeneity alone (i.e., without confounding evaporative or instrumental effects; Stumpp and Hendry, 2012) can give rise to separations in soils across a range of soil types and climates. While the subsurface processes conceptualized in advanced models, such as HYDRUS-1D, represents current mechanistic knowledge within the soil-physics community, the high degree of numerical discretization coupled with the large number of non-linear functions programed into these models, requires an evaluation of these models across an ensemble of configurations to deduce those emergent priorities inherently arising from a chosen set of soil physics. We hypothesized (1) isotopic separations should arise between water pools if a soil has heterogeneous porosities and (2) the degree of separation between water pools is controlled by soil hydraulic properties and climate conditions. This work extends beyond previous studies by identifying how interactions between climate and porosity heterogeneity within a soil profile drive incomplete mixing in soils. These results help frame how we understand and represent solute transport and mixing in the subsurface.

3.3 Understanding Dual-Porosity Isotope Separation in Soils

Isotopic separations were simulated across different hypothetical conceptualizations of water transport for a single soil type with high, low, and zero immobile water fractions and high and low mass-transfer rates between the mobile and

immobile domains (Figure 3.1). Across the range of fractions (*f*) of pore space in the immobile domain and mass transfer coefficients (ω) between the mobile and immobile domains, soils with immobile fractions exhibited distinct transport processes that were not apparent with a single porosity soil configuration (Figure 3.1c-e). Given that these models were driven with the same inputs and all other model parameters were held constant, the temporal patterns which arose were attributable to differences in simulated pore heterogeneities. Immobile soil water has limited δ^2H variability regardless of precipitation driven changes in volumetric water content (*VWC*) or drainage rates (Figure 3.1d). This contrasts with mobile-soil and drainage waters, of which δ^2H varied considerably during wetter and drier simulations periods. When parameterizations included large fractions of immobile soil water, vertical water transport reduced, matrix holding capacities increased, and mobile water fractions decreased; however, this manifested in more rapid breakthrough curves that preceded the low-*f* breakthrough curves (see days 250-260, Figure 3.1e). These differences in tracer breakthrough curves occurred because vertical movement within the soil column and mixing of precipitation inputs was limited to the mobile domain, and thus smaller *f* values implied more mixing within the column. Varying ω did not influence the breakthrough curve response. While the separations between pools were distinct, overall differences in δ^2H from each domain and model configuration were relatively small (all δ^2H ratios ranged from -70.5 to -65.3 ‰).

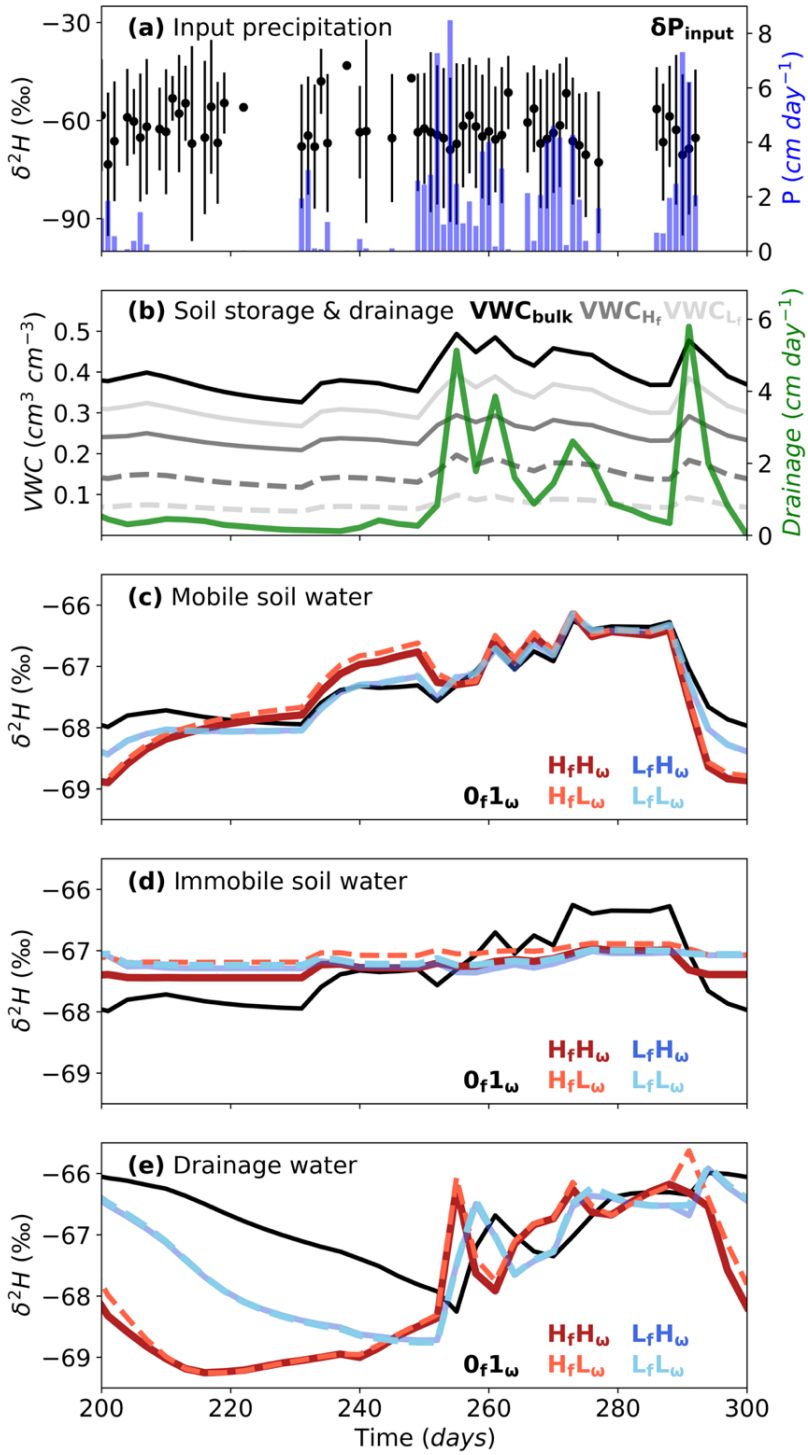

Figure 3.1 Time series of simulated precipitation, soil water pools, and drainage isotope ratios. (a) Averaged (+/- std from the 10 simulations) downscaled precipitation's stable water isotope flux-weighted concentration (δP_{input}) and the daily input precipitation.

Averaged time series of the 10 simulated (b) volumetric water contents (*VWC*) of a single porosity soil (VWC_{bulk}), the mobile (solid lines) and immobile (dashed lines) soil domains for high (H_f, dark grey, 40% of VWC_{sat}) and low (L_f, light grey, 20% of VWC_{sat}) immobile fractions, and the drainage from the column (green), (c) isotope ratio of the mobile soil water domain, (d) isotope ratio of the immobile soil water domain, and (e) isotope ratio of the column's drainage for the soils simulated with a single pore domain model (0_f1_ω, black), high immobile fraction, *f*, models with high(0.75)/low(0.25) transfer rates, ω (H_fH_ω, red; H_fL_ω, orange) and low immobile fractions with high/low transfer rates (L_fH_ω, purple; L_fL_ω, blue).

Consistently across soil configurations, as the VWC_{bulk} (mobile + immobile *VWC*) and drainage increased, the separation between water pools shifted so the drainage water more closely reflected the mobile and immobile water (i.e., the difference between drainage and mobile or mobile water ≅ 0 ‰; Figure 3.2b,c). During drier periods, stronger separations were observed between soil water pools and the drainage water (Figure 3.2b,c). This difference was likely a function of the incomplete mixing of the soil column with new incoming precipitation and the time-lag between the drained and mobile soil water pools. As VWC_{bulk} and drainage increased, models with a higher immobile fraction had the largest increase in isotopic separation (i.e. more positive slopes in Figure 3.2b,c; Supplemental Tables 3.S1, 3.S3). All dual-porosity models had positive slopes (most had significant p-values < 0.05; Supplemental Table 3.S1) and models with higher immobile fractions had steeper slopes. Interestingly, the separation between the soil and drainage water simulated by a single porosity model had a negative slope as VWC_{bulk} increased, this was distinctly different from all other models (Figure 3.2b). Within model variability in these positive and negative slopes arises as a function of the ten stochastically simulated isotope precipitation time series which served as input for each of the modeled porosity heterogeneities. Changing the incoming precipitation would likely change the slopes, however differences among modeled separations should still be apparent across soils with smaller or larger immobile fractions. Supplemental Tables 3.S1, 3.S2, and 3.S3 summarize the linear regression, p-value, Pearson correlation coefficient, and Spearman correlation coefficient calculated between isotopic separations and VWC_{bulk}, daily accumulated precipitation, and drainage. In summary, periods with

drier soil water contents will have larger separations between soil water pools and this relationship is amplified for soils with larger immobile fractions.

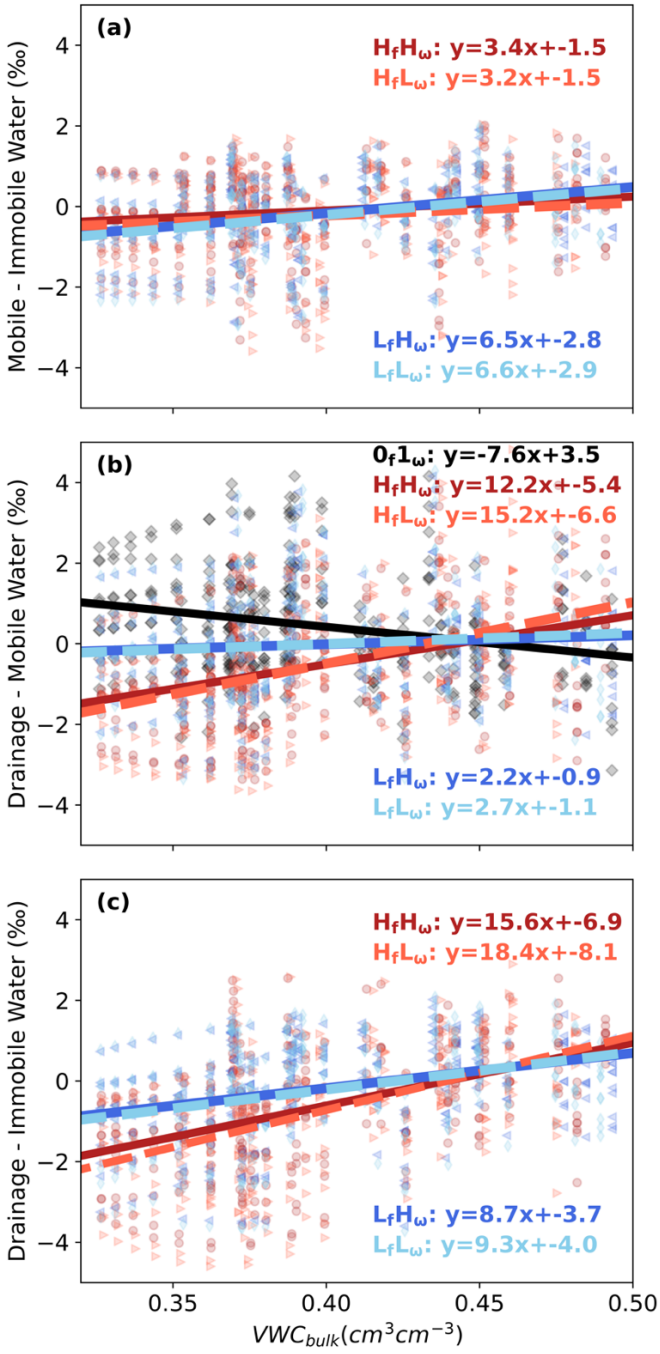

Figure 3.2 Instantaneous δ^2H differences between soil pools and fluxes during different soil moisture conditions. The separation for 10 simulations in (a) isotopic concentration of the mobile and immobile soil water at different volumetric water contents (VWC_{Bulk})

for models with high and low immobile fractions (H_f and L_f) and transfer rates (H_ω and L_ω). The separation in isotopic concentration of the drainage from the column and (b) mobile soil water and (c) immobile water at different water contents. Refer to Figure S1 in the Supplemental Information for (a-c) evaluated against depth of precipitation into and drainage from the soil column.

3.4 Dual-Porosity Isotope Separation Across Soils and Climates

Moving beyond a representation of one soil type, we explored a wide range of soil and climate characteristics with varying immobile fractions and transfer rates. Changing a soil's total saturated water content (VWC_{sat}) and saturated hydraulic conductivity (K_s) influenced the transport and mixing of soil water, thus producing different degrees of separation between mobile, immobile and drainage pools (Figure 3.3a-d). Separations between the mobile and immobile pools were more pronounced with lower VWC_{sat} and K_s (Supplemental Figure 3.S1). Lowering the VWC_{sat} produced the largest separations in soils with high f and ω (Supplemental Figure 3.S1a), accordingly large tightly bound water pools and low VWC_{sat} drive these larger separations. Furthermore, soils with large tightly bound water pools and low VWC_{sat} demonstrated decreases in the degree of separation between drainage and mobile water, and this decrease was not observed for models with smaller tightly bound pools (Figure 3.3a). Lowering VWC_{sat} and increasing the strength of transfer (ω) between the mobile and immobile domains increased the separation between drainage and immobile water (Figure 3.3b). Changing K_s influenced the separation between soil water pools as well, wherein soils with lower K_s exhibited larger separations between drainage and tightly bound water (Figure 3.3d). Varying the K_s of the soil had a minimal effect on the difference between drainage and mobile water (Figure 3.3c). Based on the 2-sample t-test, none of the dual-porosity models were statistically different compared to the single pore model (p-values > 0.5; Figure 3.3). It is worth mentioning that all simulated differences in Fig. 3a-c varied by approximately 0.5 ‰ and this difference would be difficult to observe from field observations given typical instrumental accuracy. Nevertheless, we demonstrated that appropriately representing

mobile and immobile pools is especially important for soils with low VWC_{sat} and K_s (such as with clays) when representing subsurface transport processes and drainage.

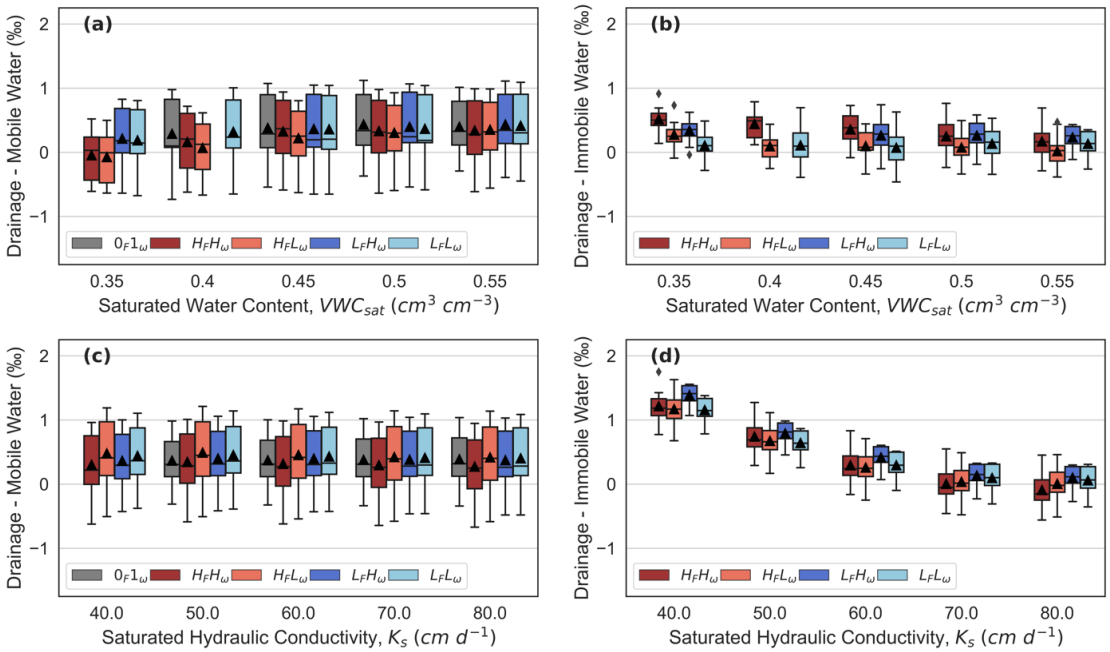

Figure 3.3 The influence of modeled soil hydraulic parameters on average δ^2H difference between drainage and (a, c) mobile or (b, d) immobile soil water. Each boxplot represents flux and volumetrically weighted averaged differences, the black triangles indicate the mean calculated from 10 simulations, and the diamonds are outliers. Missing boxplots at 0.35 cm^3cm^{-3} (a-b), 0.40 cm^3cm^{-3} (a-b), and 40 cm day^{-1} (c-d) indicate where Hydrus model configurations failed to converge. Refer to Fig. S1 in the *Supplemental Information* for the average isotopic difference between mobile and immobile soil water evaluated against the soil hydraulic parameters in (a-d).

Next, we showed that precipitation input amounts can drive the degree of separation between mobile, immobile, and drainage pools (Figure 3.4). We both increased and decreased the total input precipitation in simulations, since precipitation drove increases in *VWC* and drainage in the previous H.J. Andrews soil results. Soils receiving less precipitation yielded lower variances in the separations between drainage, mobile, and immobile pools (Figure 3.4a,b, Supplemental Figure 3.S2a). For these simulations, the soil had a high K_s (65.64 cm d^{-1}) and therefore smaller precipitation events were less likely to saturate the soil column. This influenced the rate of mass

transfer between mobile and immobile regions, which was driven by a pressure head gradient, thus decreasing the separations simulated at lower precipitation rates.

Given that precipitation amount controls both separation (as discussed in the previous paragraph) and stable isotope ratios (McDonnell, 2014; Cain et al., 2019; Kirchner, 2016; Sprenger et al., 2017), we posit that the interaction between these two relationships could be a significant factor contributing to the ecohydrologic separation phenomena. We tested if precipitation driven separations were disparate between single and heterogeneous porosity landscapes. We show that varying the strength of the amount effect on precipitation isotopic concentrations, which describes the often negative correlation (ρ) between precipitation amount and its isotopic concentration, influences separations between water pools (Figure 3.4). A large amount effect (more negative ρ) means higher intensity rainfall will have much lower δ^2H ratios than low intensity rainfall. ρ can vary depending on source precipitation (e.g., oceanic versus continental precipitation), latitude, and seasonal temperatures or precipitation patterns (Gat, 1996). Observed daily values of ρ can range from +0.24 to -0.47 (Finkenbiner et al., 2021) and an amount effect of zero removes any correlation between precipitation intensity and its isotopic composition. The most negative precipitation events were simulated when the amount effect was -0.4 and the input precipitation amount was large. Consequently, when ρ = -0.4, we simulated the largest separations between mobile and immobile soil water (Supplemental Figure 3.S2b) and the drainage and mobile soil water (Figure 3.3c). The larger separations can be attributed to the large, negative precipitation events entering the mobile soil domain later in the time series when precipitation intensity was the largest. These large, negative precipitation events also shifted the degree of separation between drainage and immobile pools (Figure 3.4d). Thus, regions with large storm events and large amount effects (i.e., rain-out effects), seasonal precipitation which transitions from snow to rain, or intense temperature changes between seasons are more likely to exhibit larger separations between pools and fluxes.

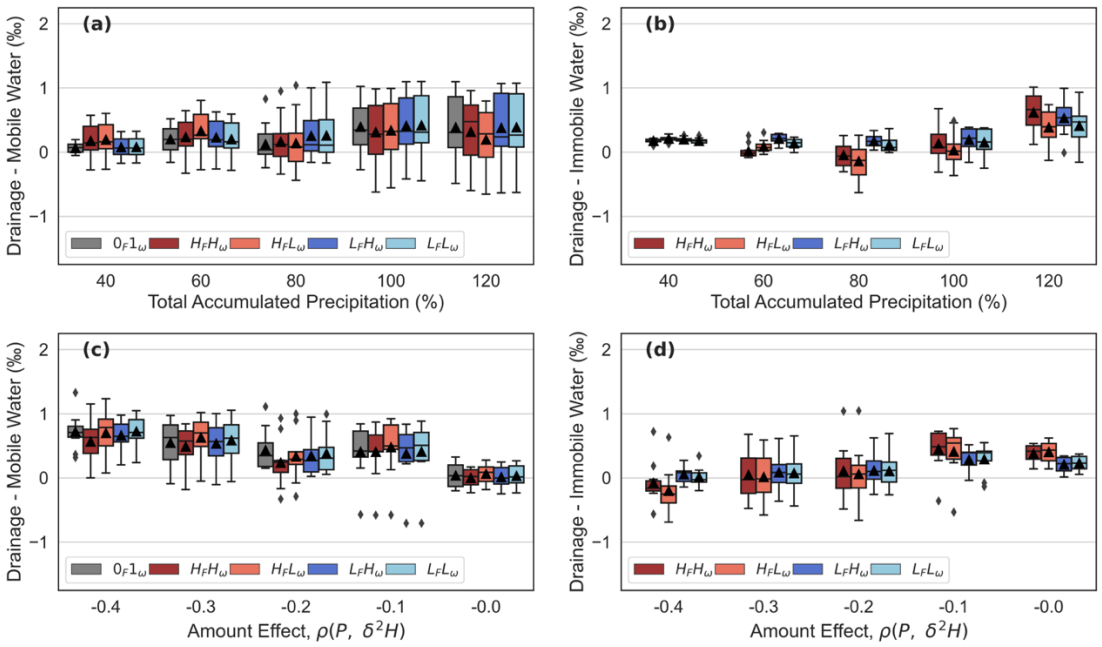

Figure 3.4 The influence of modeled climate parameters on average δ^2H difference between drainage and (a, c) mobile or (b, d) immobile soil water. (a, b) illustrates the effects of increasing or decreasing the total input precipitation (=101.5 cm) and (c, d) demonstrates the influence of strengthening the amount effect's negative correlation represented by the Pearson correlation coefficient (ρ) between precipitation amount (P) and its δ^2H concentration. Each boxplot represents flux and volumetrically weighted averaged differences, the black triangles indicate the mean calculated from 10 simulations, and the diamonds are outliers. Refer to Fig. S2 in the *Supplemental Information* for the average isotopic difference between mobile and immobile soil water evaluated against the modeled climate parameters in (a-d).

3.5 Ecohydrologic Implications

Many research studies have studied the effects of ecohydrologic separations (Brooks et al., 2010; Radolinski et al., 2021; Sprenger et al., 2019; McDonnell et al., 2014; Sprenger et al., 2016; Sprenger and Allen, 2020; Sprenger et al., 2015; Sprenger et al., 2016; Sprenger et al., 2018) and suggest different storage pools supply plant transpiration (immobile) and groundwater recharge and streamflow (mobile) (Brooks et al., 2010; Evaristo et al., 2015). Here, we demonstrate how soil properties such as a low VWC_{sat} and high f can drive larger separations between pools supplying plants and other

water pools. Our results showed the largest separations between drainage and mobile or immobile water were ~4‰ in δ^2H (Figure 3.2a) and when averaged over time, were ~1-2‰ in δ^2H (Figure 3.3a-d, 3.4a-d). We acknowledge only a few soil physical properties were investigated, and other factors which were not simulated in this study could also drive separations. Literature has cited varying degrees of separation between soils and streams, often far exceeding 4 ‰ (Brooks et al., 2010; Rodriguez et al., 2018). However, recent literature has shown that these separations are likely overestimated (Barbeta et al., 2020; Chen et al., 2020; also refer to Allen and Kirchner (2020)). Moreover, our simulated values cannot be directly compared to previous studies since streamflow is largely composed of temporally integrated groundwater at any given time and there are much longer time lags involved in streamflow generation (Berghuijs et al., 2017; Allen and Kirchner, 2021). Regardless, our results show that soils represented with heterogeneous porosities are likely to produce larger separations between soil and drainage water, and thus such soils are likely to manifest in previously described isotopic differences between soil water and streamflow.

The implications of varying of the size and influence of f and ω for tracer transport and mixing have not been explicitly investigated. Prior work by Hu et al. (2018) used the simple assumption that half of the total storage was mobile water and no mass transfer occurred between regions, nevertheless they found improved transit time estimates when compared to a complete mixing model. Here we clarify how increases in f increased the proportion of the soil matrix characterized by porous flow media, thus decreasing the amount of incoming precipitation likely to bypass the matrix and decreasing a soil's hydrologic connectivity. The largest separations between drainage and mobile or immobile water were simulated with large f values (Figure 3.2b,c). Lowering ω decreases the exchange between the matrix and preferential flow, further limiting mixing and transfer between domains especially under dry soil conditions. A high ω often increased the separation between drainage and immobile pools (Figure 3.3b,d). Based on our findings and previous work, we hypothesize that soil representations accounting for both f and ω will better characterize transport and mixing, as well as prescribing some subsurface water to reside longer (e.g., increase in f will increase the time water travels

through the matrix), while other configurations will result in more water transported through preferential flow paths.

While not explored here, other factors could drive separations quoted in previous studies. These include accounting for evaporation and the corresponding isotopic fractionation mechanisms (Zhou et al., 2021) or root water uptake from the mobile or immobile domains. It also should be noted, plant and soil water extraction techniques can introduce biases and uncertainties in stable water isotope analyses (Barbeta et al., 2020; Chen et al., 2020; Allen and Kirchner, 2021; Jasechko et al., 2016; Ellsworth et al., 2007), and many reported simulated differences are 1-2 ‰, which is approximately the precision of many laser-based systems when measuring water samples for δ^2H concentration. Consequently, the simulated differences between domains would not be able to be detected in nature.

We provided the first comprehensive evaluation of transport in the subsurface under different soil porosity heterogeneities across a range of fine to coarse soils and wet, dry, and seasonally varying climate conditions. Future research should build on this analysis and investigate other mechanisms (e.g., evaporation, root water uptake) that might drive larger separations between soils, plants, and streamflow. Regardless, we have demonstrated that separations can be explained by heterogeneous mixing in soils alone and how these separations are expected to vary with local ecohydrologic characteristics. Thus, any models aiming to realistically represent transport processes, especially those characterized through tracer observations, must represent the heterogeneity of soil pores within a soil column and the exchanges among them. This analysis demonstrated that the coexistence of both finer and coarser pores within a single soil profile by itself can manifest in real, complex tracer phenomena that have otherwise been attributed to myriad ecophysiological and hydrological processes.

3.6 Methods

The one-dimensional HYDRUS-1D dual-porosity numerical model (Šimünek et al., 2013) with modifications for stable water isotope transport (Stumpp et al., 2012) was

configured to represent 650 different porosity heterogenies across soils with different hydraulic properties and climate conditions. HYDRUS (Šimünek et al., 2013) is one of the most widely used numerical models for simulating the movement of water, heat, and solutes in various soil conditions and has been used in other isotope studies in a single porosity configuration (Stumpp and Hendry, 2012; Sprenger et al., 2016; Sprenger et al., 2018; Stumpp et al., 2012; Allen and Kirchner, 2021; Groh et al., 2018). We first configured a dual-porosity HYDRUS-1D model with parameters based on observed soil hydraulic properties from Watershed 10, H.J. Andrews Experimental Forest, Oregon, USA (Brooks et al., 2010) and simulations of VWC_{bulk} were compared against observed VWC_{bulk} from September 14, 2006 to December 23, 2006. These 100 days were selected for our analysis because precipitation events during this period were sampled for their isotopic concentration in 5 mm increments, making this a unique dataset on which to test our hypothesis since many other sampling approaches integrate precipitation sampling over a week or longer time scales. The observed precipitation samples were used within a statistical downscaling method (Finkenbiner et al., 2021) to simulate realizations of possible precipitation inputs corresponding with observed precipitation amounts. The model represented the top 100 cm of the soil profile, no evaporative effects were considered from the surface, and no root water uptake was simulated within the column. All pore water heterogeneities were driven by model parameterization of the soil physical properties. Refer to the *Supplemental Material* for further details on model configuration, parameterization, and initial conditions and the simulated input precipitation datasets.

The modeled "mobile" soil water domain represented regions of the soil matrix such as preferential flow paths or large pore-spaces and the modeled "immobile" soil water domain represented tightly bound water held at water potentials below what can drain by gravity. Water was only transported vertically in the mobile region and water movement into or out of the immobile region was controlled by the pressure head gradient and a mass transfer coefficient (ω; Šimünek et al., 2013). We investigated five model configurations characterizing different heterogeneous mixing and transport: 1) a model representing a single-pore domain with no f and the ω equaling 1 (0_f1_ω), 2) a model with a high f representing 40% of the total saturated water content (VWC_{sat}) and

high ω equaling 0.75 (H_fH_ω), 3) a model with a low *f* representing 20% of the VWC_{sat} and high ω equaling 0.75 (L_fH_ω), and 4) a model with a high *f* representing 40% of the VWC_{sat} and low ω equaling 0.25 (H_fL_ω), and 5) a model with a low *f* representing 20% of the VWC_{sat} and low ω equaling 0.25 (L_fL_ω). These five model configurations were tested across a range of different precipitation inputs and soil hydraulic properties, which were varied in relation to the original soil column configured from observed datasets from Watershed 10, H.J. Andrews Experimental Forest.

In total, we present 650 simulations of HYDRUS-1D with varying *f*, ω, VWC_{sat}, K_s, total accumulated precipitation, and amount effects describing the correlation between precipitation amount and its isotopic composition. When varying soil hydraulic parameters across model configurations, all other parameters were held constant and VWC_{sat} or K_s was altered. We increased or decreased the total accumulated precipitation by multiplying each precipitation event in the input time series by a specific percentage. New precipitation isotope ratios were generated (refer to the *Supplemental Material*) with stronger or weaker negative correlations between precipitation depth and its isotopic ratio. All model simulations had relatively low mass balance errors (average relative error = 0.09 %) and solute balance errors (average relative error = 0.001 ‰) calculated by HYDRUS-1D during the numerical computations (Šimünek et al., 2013).

This study represented 100 days in a Pacific Northwest winter wet season (Brooks et al., 2010; Rodriguez et al., 2018) and not a full year with dry periods, large evaporative effects, or high transpiration rates. The 100-day time series was repeated three times to remove the effects of the initial condition of the soil's stable water isotope signature, and the final 100 days (days 200-300) were analyzed in the presented results. We chose this approach to reduce the confounding effects of evaporation and we were constrained by the computation limitations imposed by running HYDRUS-1D with many configurations. The observation dataset from Brooks et al. (2010) was used to calibrate our modeled soil properties, however our objective was not to exactly simulate the observed water isotope datasets. The simulated stable water isotopes in precipitation are not equal to the actual precipitation during the period and we did not know the initial soil water's isotopic

concentration. Our focus was to test the dual-porosity approach across 650 representations of transport dynamics across soils and climates.

3.7 Acknowledgements

The authors acknowledge the support of the United States National Science Foundation (DEB-1802885). This manuscript has been subjected to Agency review and has been approved for publication. The views expressed in this paper are those of the author(s) and do not necessarily reflect the views or policies of the U.S. Environmental Protection Agency. Mention of trade names or commercial products does not constitute endorsement or recommendation for use.

3.8 References

Allen, S. T. and Kirchner, J. W. Potential effects of cryogenic extraction biases on inferences drawn from xylem water deuterium isotope ratios: case studies using stable isotopes to infer plant water sources. *Hydrol Earth Syst Sci Discuss* [preprint] https://doi.org/10.5194/hess-2020-683, in review (2021).

Barbeta, A., Gimeno, T.E., Clavé, L., et al. An explanation for the isotopic offset between soil and stem water in a temperate tree species. *New Phytol* 227, 766-779 (2020). https://doi.org/10.1111/nph.16564

Berghuijs, W.R. and Kirchner, J.W. The relationship between contrasting ages of groundwater and streamflow. *Geophys Res Lett* 44, 8925-8935 (2017). https://doi.org/10.1002/2017GL074962.

Berry, Z.C., Evaristo, J., Moore, G., et al. The two water worlds hypothesis: Addressing multiple working hypotheses and proposing a way forward. *Ecohydrology* 11, e1843 (2018). https://doi.org/10.1002/eco.1843

Brooks, J. R., Barnard, H., Coulombe, R. et al. Ecohydrologic separation of water between trees and streams in a Mediterranean climate. *Nature Geosci* 3, 100–104 (2010). https://doi.org/10.1038/ngeo722

Cain, M.R., Ward, A.S., and Hrachowitz, M. Ecohydrologic separation alters interpreted hydrologic stores and fluxes in a headwater mountain catchment. *Hydrol Process* 33, 2658-2675 (2019). https://doi.org/10.1002/hyp.13518

Chen, Y., Helliker, B.R., Tang, X., Li, F., Zhou, Y., and Song, X. Stem water cryogenic extraction biases estimation in deuterium isotope composition of plant source water. *Proc Natl Acad Sci USA* 52, 33345-33350 (2020). https://doi.org/10.1073/pnas.2014422117

Dubbert, M., Caldeira, M.C., Dubbert, D. and Werner, C. A pool-weighted perspective on the two-water-worlds hypothesis. *New Phytol* 222, 1271-1283 (2019). https://doi.org/10.1111/nph.15670

Ellsworth, P.Z., and Williams, D.G. Hydrogen isotope fractionation during water uptake by woody xerophytes. *Plant Soil* 291, 93-107 (2007). https://doi.org/10.1007/s11104-006-9177-1

Evaristo, J., Jasechko, S. and McDonnell, J. Global separation of plant transpiration from groundwater and streamflow. *Nature* 525, 91-94 (2015). https://doi.org/10.1038/nature14983

Finkenbiner, C.E., Good, S.P., Allen, S.T., Fiorella, R.P., and Bowen, G.J. A statistical method for generating temporally downscaled geochemical tracers in precipitation. *J Hydrometerol* 22, 1473-1486 (2021). https://doi.org/10.1175/JHM-D-20-0142.1

Gat, J. R. Oxygen and hydrogen isotopes in the hydrologic cycle. *Annu. Rev. Earth Planet Sci*. 24, 225–262 (1996). https://doi.org/10.1146/annurev.earth.24.1.225.

Groh, J., Stumpp, C., Lücke, A., Pütz, T., Vanderborght, J., and Vereecken, H. Inverse estimation of soil hydraulic and transport parameters of layered soils from water stable isotope and lysimeter data. *Vadose Zone J* 17, 170168 (2018). https://doi.org/10.2136/vzj2017.09.0168

Hu, H., Dominguez, F., Kumar, P., McDonnell, J., and Gochis, D. A numerical water tracer model for understanding event-scale hydrometeorological phenomena. *J Hydrometeorol* 19, 947-967 (2018). https://doi.org/10.1175/JHM-D-17-0202.1

Jasechko, S., Kirchner, J.W., Welker, J.M., and McDonnell, J.J. Substantial proportion of global streamflow less than three months old. *Nat Geosci*, 9, 126-129 (2016).

Kirchner, J. W. Aggregation in environmental systems – Part 2: Catchment mean transit times and young water fractions under hydrologic nonstationarity, *Hydrol Earth Syst Sci* 20, 299-328 (2016). https://doi.org/10.5194/hess-20-299-2016

Knighton, J., Kuppel, S., Smith, A., et al. Using isotopes to incorporate tree water storage and mixing dynamics into a distributed ecohydrologic modelling framework. *Ecohydrol* 13, e2201 (2020). https://doi.org/10.1002/eco.2201

Małoszewski, P., Maciejewski, S., Stumpp, C., Stichler, W., Trimborn, P., and Klotz, D. Modelling of water flow through typical Bavarian soils: 2. Environmental deuterium transport. *Hydrol Sci J* 51, 298-313 (2006). https://doi.org/10.1623/hysj.51.2.298

McDonnell, J.J. The two water worlds hypothesis: ecohydrological separation of water between streams and trees? *WIREs Water* 1, 323-329 (2014). https://doi.org/10.1002/wat2.1027

Mueller, M.H., Alaoui, A., Kuells, C. et al. Tracking water pathways in steep hillslopes by $\delta^{18}O$ depth profiles of soil water. *J Hydrol* 519, 340-352 (2014). https://doi.org/10.1016/j.jhydrol.2014.07.031

Radolinski, J., Pangle, L., Klaus, J., and Stewart, R.D. Testing the 'two water worlds' hypothesis under variable preferential flow conditions. *Hydrol Process* 35, e14252 (2021). https://doi.org/10.1002/hyp.14252

Rodriguez, N. B., McGuire, K. J., & Klaus, J. Time-varying storage–Water age relationships in a catchment with a Mediterranean climate. *Water Resour. Res.* 54, 3988–4008 (2018). https://doi.org/10.1029/2017WR021964

Šimünek, J., Šejna, M., Saito, H., Sakai, M., and van Genuchten, M.Th. The HYDRUS-1D software package for simulating the one-dimensional movement of water, heat, and multiple solutes in variably-saturated media – version 4.17, HYDRUS software series 1. Department of Environmental Sciences, University of California Riverside, Riverside, CA, 2013, pp. 308 pp.

Sprenger, M., and Allen, S. T. Commentary: What ecohydrologic separation is and where we can go with it. *Water Resour Res* 56, e2020WR027238 (2020). https://doi.org/10.1029/2020WR027238

Sprenger, M., Leistert, H., Gimbel, K., and Weiler, M. Illuminating hydrological processes at the soil-vegetation-atmosphere interface with water stable isotopes. *Rev Geophys* 54, 674– 704 (2016). https://doi.org/10.1002/2015RG000515

Sprenger, M., Llorens, P., Cayuela, C., Gallart, F., and Latron, J. Mechanisms of consistently disjunct soil water pools over (pore) space and time, *Hydrol Earth Syst Sci* 23, 2751–2762 (2019). https://doi.org/10.5194/hess-23-2751-2019

Sprenger, M., Seeger, S., Blume, T., and Weiler, M. Travel times in the vadose zone: Variability in space and time. *Water Resour Res* 52, 5727-5754 (2016). https://doi.org/10.1002/2015WR018077

Sprenger, M., Tetzlaff, D., Buttle, J., et al. Measuring and modeling stable isotopes of mobile and bulk soil water. *Vadose Zone J* 17,170149 (2018). https://doi.org/10.2136/vzj2017.08.0149

Sprenger, M., Tetzlaff, D., and Soulsby, C. Soil water stable isotopes reveal evaporation dynamics at the soil–plant–atmosphere interface of the critical zone. *Hydrol Earth Syst Sci* 21, 3839–3858 (2017). https://doi.org/10.5194/hess-21-3839-2017

Sprenger, M., Volkmann, T.H.M., Blume, T., and Weiler, M. Estimating flow and transport parameters in the unsaturated zone with pore water stable isotopes. *Hydrol Earth Syst Sci* 19, 2617–2635 (2015). https://doi.org/10.5194/hess-19-2617-2015

Stumpp, C. and Hendry, M.J. Spatial and temporal dynamics of water flow and solute transport in a heterogeneous glacial till: The application of high-resolution profiles of $\delta^{18}O$ and $\delta^{2}H$ in pore waters. *J Hydrol* 438-439, 203-214 (2012). https://doi.org/10.1016/j.jhydrol.2012.03.024

Stumpp, C. and Maloszewski, P. Quantification of preferential flow and flow heterogeneities in an unsaturated soil planted with different crops using the environmental isotope $\delta^{18}O$. *J Hydrol* 394, 407-415 (2010). https://doi.org/10.1016/j.jhydrol.2010.09.014

Stumpp, C., Nützmann, G., Maciejewski, S., and Maloszewski, P. A comparative modeling study of a dual tracer experiment in a large lysimeter under atmospheric conditions. *J Hydrol* 375, 566-577 (2009). https://doi.org/10.1016/j.jhydrol.2009.07.010

Stumpp, C., Stichler, W., Kandolf, M., and Šimůnek, J. Effects of land cover and fertilization method on water flow and solute transport in five lysimeters: A long-term study using stable water isotopes. *Vadose Zone J* 11, vzj2011.0075 (2012). https://doi.org/10.2136/vzj2011.0075

Vargas, A.I., Schaffer, B., Yuhong, L., and Sternberg, L.D.S.L. Testing plant use of mobile vs immobile soil water sources using stable isotope experiments. *New Phytol* 215, 582-594 (2017). https://doi.org/10.1111/nph.14616. Epub 2017 May 30. PMID: 28556977

Zhou, T., Simunek, J., and Braund I Adapting HYDRUS-1D to simulate the transport of soil water isotopes with evaporation fractionation. *Environ Model Softw* 143, 105118 (2021). https://doi.org/10.1016/j.envsoft.2021.105118

Chapter 3.9 Supplemental Material

3.9.1 Modeled Soil Configuration and Parameterization

Soil hydraulic properties for the soil at H.J. Andrews was approximated with the HYDRUS-1D built-in ROSETTA DLL (Dynamically Linked Library) software which implements pedotransfer functions that predict van Genuchten (1980) water retention parameters and the saturated hydraulic conductivity (K_s). The values used within the pedotransfer function where 27, 35, and 38% sand, silt, and clay, respectively, and a porosity of 60% (these are the same values cited in Brooks et al., (2010)). The estimated VWC_{sat} was 0.55 cm^3cm^{-3} and K_s was 65.64 cm d^{-1}. The root-mean-square error (RMSE) of the observed and modeled VWC_{bulk} was 0.06 cm^3cm^{-3}. We used multiple techniques to estimate the soil hydraulic parameters based on observed hydraulic properties at H.J. Andrews and the *VWC* time series from Brooks et al. (2010), this included inverse modeling and a large Monte Carlo analysis. Based on RMSE, ROSETTA DLL outperformed all techniques and was computationally efficient. It is important to note the objective was not to replicate the observed time series perfectly. No soil evaporation or root water uptake was simulated, as to drive all isotopic differences between soil domains from the parameterized soil physics.

3.9.2 Modeled Input Precipitation Datasets

We generated precipitation isotope time-series which reflected the average and variance of the δ^2H ratio and its correlation with precipitation depth over time. Observed δ^2H in precipitation was sampled in 5 mm increments over the study period (2010), but the model required input data on 15-minute increments. Accordingly, the observed time series was downscaled, using the statistical downscaling method described by Finkenbiner et al. (2021), to correspond with the observed 15-minute precipitation data (H.J. Andrews PRIMNET database (Daly and McKee, 2019), Figure 3.1a). The total input precipitation amount for the 100 days was 101.5 cm. The statistical downscaling method decomposed the observed precipitation isotope ratio time series into its deterministic and stochastic components. δ^2H ratios were simulated from a Gaussian

distribution using the observed mean of -66.7 ‰, standard deviation of 21.5 ‰, and Pearson correlation coefficient (ρ), ρ(precipitation (cm), δ^2H ratio (‰)), of -0.16. The generated precipitation isotope time series had seasonality effects removed as to drive separations strictly from soil properties or amount effects. Ten unique 15-minute δ^2H time series were generated for each model configuration and each time series captured the statistics of the sampled precipitation (Figure 3.1a). We chose to simulate ten time series of δ^2H ratios as to not tie results to one specific input time series. Additionally, an ensemble size of ten time series was chosen due to the lengthy computational time of each model (~5 min), the amount of time required to process, manipulate, and analyze the output files, and the size of the HYDRUS-1D input/output files (~100-150 MB).

3.9.3 Modeled Initial Conditions

The soil water's initial δ^2H concentration was unknown and we decided to set it equal the average weighted precipitation. The 100-day time series was repeated three times to remove the effects of the initial condition of the soil's isotopic concentration, and the final 100 days (days 200-300) were analyzed in the presented results. To explore the effects of changing the initial condition of the isotopic concentration of the soil water, we changed the soil's initial condition to a very high δ^2H value of +200 ‰. The mobile soil water decreases to average soil water concentrations observed in other model configurations presented in this paper within the 200-day period. Immobile soil water takes much longer, most likely a function of the mass transfer rate between the mobile and immobile domains, and eventually decreases to the average soil water concentrations observed in other model configurations. Therefore, we concluded that changing the initial condition would have minimal impact on the presented results.

Table 3.S1 The linear regression, p-value, Pearson correlation coefficient, and Spearman correlation coefficient for the isotopic separation between water pools and VWC_{bulk}.

	Linear Regression	**p-value**	**Pearson**	**Spearman**
	Mobile - Immobile Water v. VWC_{bulk} (cm^3cm^{-3})			
$\mathbf{H_fH_\omega}$	y = 3.4x - 1.5	5.00E-03	0.15	0.13
$\mathbf{L_fH_\omega}$	y = 6.5x - 2.8	1.69E-08	0.30	0.28
$\mathbf{H_fL_\omega}$	y = 3.2x - 1.5	2.00E-02	0.13	0.09
$\mathbf{L_fL_\omega}$	y = 6.6x - 2.9	3.60E-08	0.30	0.27
	Drainage - Mobile Water v. VWC_{bulk} (cm^3cm^{-3})			
$\mathbf{0_f1_\omega}$	y = -7.6x + 3.5	2.06E-06	-0.26	-0.23
$\mathbf{H_fH_\omega}$	y = 12.2x - 5.4	1.61E-12	0.38	0.37
$\mathbf{L_fH_\omega}$	y = 2.2x - 0.9	1.90E-01	0.07	0.11
$\mathbf{H_fL_\omega}$	y = 15.2x - 6.6	7.97E-15	0.41	0.42
$\mathbf{L_fL_\omega}$	y = 2.7x - 1.1	1.20E-01	0.09	0.12
	Drainage - Immobile Water v. VWC_{bulk} (cm^3cm^{-3})			
$\mathbf{H_fH_\omega}$	y = 15.6x - 6.9	3.60E-20	0.48	0.47
$\mathbf{L_fH_\omega}$	y = 8.7x - 3.7	1.25E-09	0.33	0.35
$\mathbf{H_fL_\omega}$	y = 18.4x - 8.1	5.53E-22	0.50	0.50
$\mathbf{L_fL_\omega}$	y = 9.3x - 4.0	9.21E-10	0.33	0.35

Table 3.S2 The linear regression, p-value, Pearson correlation coefficient, and Spearman correlation coefficient for the isotopic separation between water pools at the end of a day and daily accumulated precipitation.

	Linear Regression	**p-value**	**Pearson**	**Spearman**
	Mobile - Immobile Water v. Precipitation (cm)			
$\mathbf{H_f H_\omega}$	y = -0.001x - 0.1	8.89E-01	-0.03	-0.21
$\mathbf{L_f H_\omega}$	y = 0.01x - 0.2	4.03E-01	0.15	0.33
$\mathbf{H_f L_\omega}$	y = -0.002 - 0.2	7.75E-01	-0.05	0.17
$\mathbf{L_f L_\omega}$	y = 0.004 - 0.3	4.32E-01	0.14	0.33
	Drainage - Mobile Water v. Precipitation (cm)			
$\mathbf{0_f 1_\omega}$	y = -0.01x + 0.5	5.25E-01	-0.12	-0.34
$\mathbf{H_f H_\omega}$	y = 0.02x - 0.8	1.48E-02	0.42	0.36
$\mathbf{L_f H_\omega}$	y = 0.01x - 0.2	1.22E-01	0.28	0.06
$\mathbf{H_f L_\omega}$	y = 0.02x - 0.8	1.48E-02	0.42	0.43
$\mathbf{L_f L_\omega}$	y = 0.01x - 0.2	1.23E-01	0.27	0.07
	Drainage - Immobile Water v. Precipitation (cm)			
$\mathbf{H_f H_\omega}$	y = 0.02x - 0.9	2.00E-02	0.40	0.54
$\mathbf{L_f H_\omega}$	y = 0.02x - 0.4	1.00E-02	0.44	0.37
$\mathbf{H_f L_\omega}$	y = 0.02x - 1.0	2.00E-02	0.40	0.54
$\mathbf{L_f L_\omega}$	y = 0.02x - 0.4	1.40E-02	0.42	0.37

Table 3.S3 The linear regression, p-value, Pearson correlation coefficient, and Spearman correlation coefficient for the isotopic separation between water pools and drainage.

	Linear Regression	**p-value**	**Pearson**	**Spearman**
	Mobile - Immobile Water v. Drainage (cm)			
$\mathbf{H_fH_\omega}$	y = 0.1x - 0.2	2.20E-02	0.13	0.18
$\mathbf{L_fH_\omega}$	y = 0.2x - 0.4	3.54E-05	0.23	0.34
$\mathbf{H_fL_\omega}$	y = 0.2x - 0.4	6.00E-02	0.10	0.14
$\mathbf{L_fL_\omega}$	y = 0.1x - 0.3	3.19E-05	0.23	0.33
	Drainage - Mobile Water v. Drainage (cm)			
$\mathbf{0_f1_\omega}$	y = -0.2x + 0.7	2.50E-04	-0.20	-0.25
$\mathbf{H_fH_\omega}$	y = 0.4x -1.0	5.21E-12	0.37	0.40
$\mathbf{L_fH_\omega}$	y = 0.1x - 0.1	5.70E-02	0.06	0.09
$\mathbf{H_fL_\omega}$	y = 0.5x -1.1	2.25E-12	0.37	0.39
$\mathbf{L_fL_\omega}$	y = 0.1x - 0.1	3.05E-01	0.57	0.11
	Drainage - Immobile Water v. Drainage (cm)			
$\mathbf{H_fH_\omega}$	y = 0.5x - 1.2	7.41E-18	0.45	0.56
$\mathbf{L_fH_\omega}$	y = 0.2x - 0.4	6.73E-06	0.25	0.36
$\mathbf{H_fL_\omega}$	y = 0.6x - 1.4	1.83E-17	0.45	0.52
$\mathbf{L_fL_\omega}$	y = 0.2x - 0.5	9.35E-06	0.24	0.37

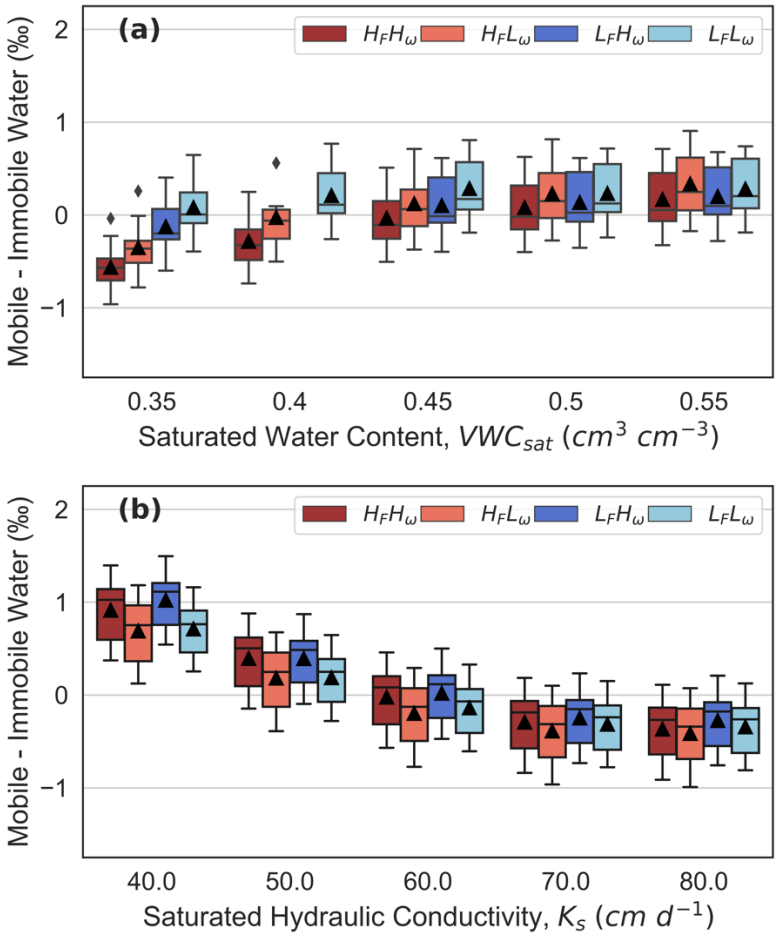

Figure 3.S1 The influence of modeled soil hydraulic parameters on average δ^2H difference between mobile and immobile soil water. Each boxplot represents flux and volumetrically weighted averaged differences and the black triangles indicate the mean calculated from 10 simulations. The missing boxplot at 0.40 cm^3cm^{-3} indicates where Hydrus model configurations failed to converge.

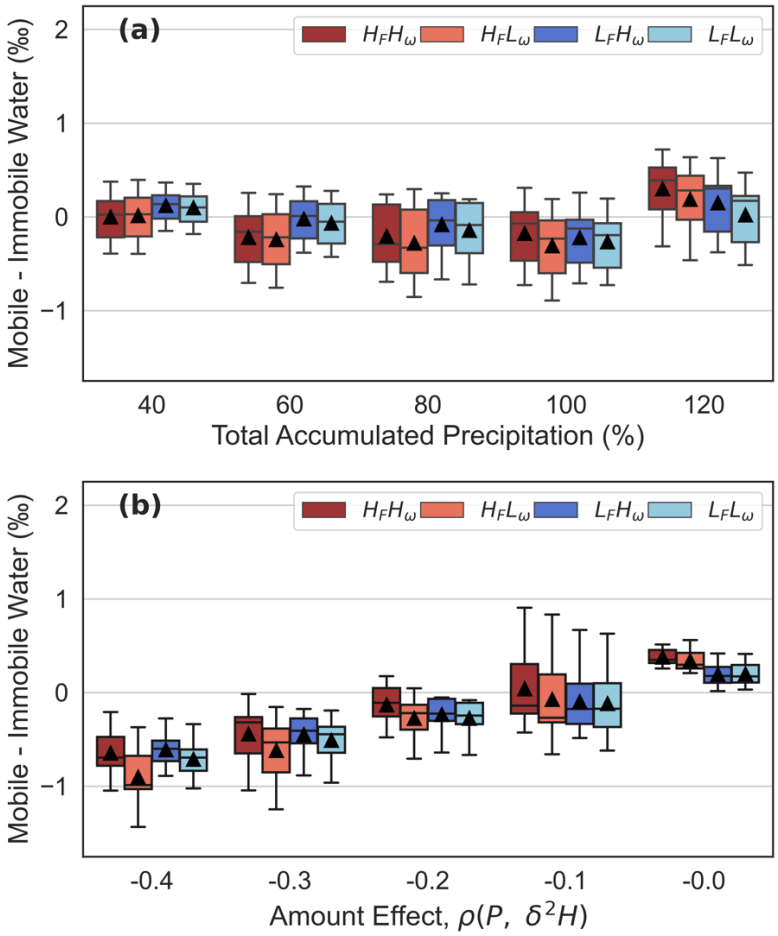

Figure 3.S2 The influence of modeled climate parameters on average δ^2H difference between mobile and immobile soil water. (a) illustrates the effects of increasing or decreasing the total input precipitation and (b) demonstrates the influence of adjusting the strength of the Pearson correlation coefficient between precipitation amount and its δ^2H concentration. Each boxplot represents flux and volumetrically weighted averaged differences and the black triangles indicate the mean calculated from 10 simulations.

3.9.4 References for the Supplemental Materials

van Genuchten, M.T. A closed-form equation for predicting the hydraulic conductivity of unsaturated soils. *Soil Science Society of America Journal* 44, 892-898 (1980). https://doi.org/10.2136/sssaj1980.03615995004400050002x

Brooks, J. R., Barnard, H., Coulombe, R. et al. Ecohydrologic separation of water between trees and streams in a Mediterranean climate. *Nature Geosci* 3, 100–104 (2010). https://doi.org/10.1038/ngeo722

Finkenbiner, C.E., Good, S.P., Allen, S.T., Fiorella, R.P., and Bowen, G.J. A statistical method for generating temporally downscaled geochemical tracers in precipitation. *J Hydrometerol* 22, 1473-1486 (2021). https://doi.org/10.1175/JHM-D-20-0142.1

Daly, C. and McKee, W.A. Meteorological data from benchmark stations at the Andrews Experimental Forest, 1957 to present ver 36. Environmental Data Initiative (2019). https://doi.org/10.6073/pasta/c021a2ebf1f91adf0ba3b5e53189c84f (Accessed 2021-04-21).

Chapter 4. Datasets of Daily Water and Carbon Stable Isotope Ratios for Precipitation, Evapotranspiration, and Net Ecosystem Exchange Fluxes at NEON Sites

4.1 Abstract

The National Ecological Observatory Network (NEON) provides open-access measurements of stable isotope ratios in atmospheric water vapor (δ^2H, $\delta^{18}O$) and carbon dioxide ($\delta^{13}C$) at different tower heights, as well as aggregated biweekly precipitation collections (δ^2H, $\delta^{18}O$) across the United States. Based on these NEON measurements, daily estimates of isotope ratios of precipitation (P; δ^2H, $\delta^{18}O$), evapotranspiration (ET; δ^2H, $\delta^{18}O$), and net ecosystem exchange (NEE; $\delta^{13}C$) fluxes have been quantified. Statistically downscaled precipitation datasets were generated to be consistent with the estimated covariance between isotope ratios and precipitation amounts at daily time scales. Isotope ratios in ET and NEE fluxes were estimated using a mixing model approach with NEON tower measurements and site-specific isotope calibrations. The datasets are publicly available on HydroShare and can be reproduced or modified to fit user specific applications or include additional NEON data records as they become available. The daily flux isotope ratios can facilitate understanding of terrestrial ecosystem processes through their incorporation into environmental investigations that require daily δ^2H, $\delta^{18}O$, and $\delta^{13}C$ flux data.

4.2 Background & Summary

The stable isotope ratios of carbon and water fluxes are natural environmental tracers that can be used to provide new insights into hydrological, ecological, and meteorological processes, as well as provide supportive metrics for understanding the complex feedbacks between the land surface and atmosphere (Chai et al., 2015; Brooks et al., 2014; Good et al., 2015; Gupta et al., 2020; Kanner et al., 2014; Remondi et al., 2018). These tracers are informative in ecohydrologic modeling applications because

they provide additional points of comparison between observed and modeled environmental pools and fluxes (Abbott et al., 2016), as well as to evaluate the performance and efficiency of modeling approaches (Krause et al., 2005).

Tracers commonly used in studies of land surface processes from global to local scales include the stable isotope ratios of hydrogen ($^{2}H/^{1}H$), oxygen ($^{18}O/^{16}O$), and carbon ($^{13}C/^{12}C$), found in water and carbon dioxide, hereafter expressed as $\delta^{2}H$, $\delta^{18}O$ and $\delta^{13}C$ values (Krause et al., 2005; Bowen & Good, 2015; McGuire & McDonnell, 2006; Sprenger et al., 2019; Turnadge & Smerdon, 2014; Fiorella et al., 2021). Water isotope ratios provide useful information for partitioning evapotranspiration (ET) into evaporation and transpiration at the ecosystem scales (Good et al., 2015; Xiao et al., 2018), as well as understanding water use efficiency in forests, agricultural, and other ecosystems (Wu et al., 2018; Al-Qaili et al., 2020). Carbon isotope ratios provide valuable information about the component fluxes that determine net exchange of carbon dioxide between ecosystems and the atmosphere (Fiorella et al., 2021; Bowen et al., 2019). Insights into such processes support the understanding of plant water uptake strategies and the underlying principles of water, carbon, and energy cycling in the soil-vegetation-atmosphere continuum (Good et al., 2015; Xiao et al., 2018; Lu et al., 2017; Wieser et al., 2016).

The United States National Ecological Observatory Network (NEON) collects long-term ecological data in eco-climatologically diverse field sites across the United States and provisions these data through an open access data portal (https://data.neonscience.org/). These publicly available isotope datasets are part of an important network documenting hydrometeorological tracer patterns throughout North America. The NEON atmospheric gas stable-isotope measurements are collected at approximately hourly intervals (varying by site), enabling robust daily calculations of net-ecosystem-exchange (NEE) and evapotranspiration flux (ET) isotope ratios (e.g., via mass balance approaches developed by Keeling (Pataki et al., 2003) and Miller-Tans (Miller & Tans, 2003)). The precipitation isotope data are collected at biweekly intervals, but they can be downscaled to a daily resolution using a validated approach (Finkenbiner

et al., 2021a). By conducting those pre-processing steps, we can facilitate subsequent applications using these published daily flux data products.

We generated daily records of a) δ^2H and $\delta^{18}O$ in precipitation fluxes (F_P) at 16 NEON core sites and 16 NEON relocatable sites, b) δ^2H and $\delta^{18}O$ of ET fluxes (F_{ET}) at 19 NEON core sites and 2 NEON relocatable sites, and c) $\delta^{13}C$ of NEE fluxes (F_{NEE}) at 19 NEON core sites and 28 NEON relocatable sites. These products form daily flux isotope datasets across diverse ecosystems over a multi-year span created using consistent instrumentation and methodology. The dataset analyzed here are reproducible with the published python and R scripts. The methods can easily be modified to fit a user's specific application or as additional NEON data records become available in the future. The subsequent sections detail the methods used to derive isotope ratios associated with the F_P, F_{ET} and F_{NEE} fluxes, the validation of each method, and a description of the associated metadata.

4.3 Methods

4.3.1 Precipitation Flux Data Products

We acquired 30-minute precipitation data and stable water isotopes in precipitation collected in biweekly intervals from the NEON Data Portal (NEON, 2021) using the neonUtilities R package (Lunch & Laney, 2020). A wet deposition collector at each site opens during rain events to collect samples, which are then retrieved, filtered, and analyzed approximately every two weeks (Lee & Weintraub, 2021). All datasets with stable water isotopes in precipitation (as of Spring 2021) were downloaded, as well as the corresponding precipitation amount data. There were 44 sites across the NEON network with water isotope data, 38 of which contained sufficient data to perform the downscaling methodology (refer to the NEON data product number 1.00006.001 for precipitation amounts and 1.00038.001 for precipitation stable isotope concentrations). At the time of this publication, NEON's "primary" precipitation data had a known issue where the weighing gauge had recorded spurious small precipitation amounts. Consequently, we used the "secondary" collector data (from a tipping bucket rain gauge) when available,

and the primary data was only used at sites that did not have secondary data. As a further quality check, we removed trace precipitation events, defined here as less than 0.25 mm of accumulated precipitation in one day. This threshold can be changed within the code to generate new data products.

The NEON precipitation samples for isotope analysis are collected at an approximately biweekly resolution. This temporal resolution is shorter relative to past network collections (e.g., the Global Network of Isotopes in Precipitation (GNIP) contains data mostly at monthly resolutions (IAEA, 2020)), but is still coarser than what is required for land modelling applications. Consequently, by downscaling from biweekly to daily resolution a fine-scale product is available for future studies. The daily stable water isotopes associated with the F_P were generated at each NEON site with sufficient observation data to conduct a statistical downscaling method (Finkenbiner et al., 2021a), which translated the observed biweekly water isotope samples to a daily estimate correlating with known precipitation amounts. The statistical downscaling method was described in detail and validated by Finkenbiner et al. (2021a), here we provide a summary of the method applied to the NEON datasets.

At each NEON site, the 30-minute precipitation amounts were aggregated to daily and biweekly totals to correspond with the biweekly tracer observations and provide a daily time series on which to condition the generated daily tracer values. The seasonal component of each δ^2H and $\delta^{18}O$ time series was characterized using a combination of sinusoidal functions through Fourier decomposition, following the methods from Allen et al. (2018), and removed. The remaining values were assumed to be drawn from a purely stochastic process with a mean of zero. The daily covariance statistics were predicted based on trends in the means, standard deviations, and Pearson correlation coefficients as each time series was aggregated from biweekly to coarser resolutions. Some NEON sites had few biweekly observations and were unable to be aggregated to the 12-week resolution required for the downscaling method. We anticipate as NEON continues to collect observations and the site data represents longer seasonal time scales, this downscaling method can be applied at additional sites. δ^2H and $\delta^{18}O$ stable water isotopes are strongly correlated with each other (Craig, 1961) and often share a weaker, but

significant, relationship with precipitation amount (Dansgaard, 1964). A Gaussian copula (Sklar, 1959) conditioned on daily precipitation amounts was used to generate pseudo-random values from the predicted de-seasonalized daily statistics of δ^2H and $\delta^{18}O$ from the stochastic signal. A copula is a multivariate cumulative distribution function used to model the dependence between random variables (Sklar, 1959), here the random variables were precipitation amount and its isotopic ratios. Lastly, the pre-defined seasonal component was added to each stochastic isotope series and a residual correction was performed. The residual correction adjusts the downscaled daily δ^2H and $\delta^{18}O$ values by forcing the biweekly precipitation weighted means of the downscaled data to match those of the observed biweekly dataset. At each NEON site with sufficient observation data, we generated a final synthetic daily time series which corresponded with daily precipitation amounts, seasonal signals, and stochastic variability.

4.3.2 Gas Flux Data Products

The NEON atmospheric isotope measurements provide continental-scale ongoing measurements of $\delta^{13}C\text{-}CO_2$, $\delta^{18}O\text{-}H_2O_{vapor}$, and $\delta^2H\text{-}H_2O_{vapor}$ at established eddy covariance towers. The NEON eddy covariance bundled product (refer to NEON data product number DP4.00200.001) provides δ^2H, $\delta^{18}O$, and $\delta^{13}C$ values of the atmospheric gases at different tower heights with a typical averaging interval of 9-minutes (the return interval varies and can be up to 90-minutes). Gases are sampled at each height for ten minutes, with the first minute discarded, and then cycled to the next height; thus, the sampling interval depends on the number of heights sampled per tower. These measurements were integrated (i.e., averaged) to daily stable water and carbon isotopes associated with the F_{ET} and F_{NEE} fluxes.

The estimation of the daily carbon and water isotope composition of the F_{ET} and F_{NEE} fluxes requires two procedures: 1) calibration of NEON's measured carbon and water isotope ratios to known standards and 2) translation of those values to the Vienna Pee Dee Belemnite (VPDB) and Vienna Standard Mean Ocean (VSMOW) scales. The measured carbon and water isotope ratios frequently diverge from the VPDB and VSMOW scales due to the instrumentation drift, poor instrument calibration, or bias that

has not yet been removed from the calibration routines. Fiorella et al. (2021) provided a calibration strategy to correct the measured $\delta^{13}C$ values to the VPDB scale as part of the NEONiso R package (Lunch & Laney, 2020). Since that publication, NEONiso has been expanded to include calibrations for $\delta^{2}H$ and $\delta^{18}O$ values. We estimated the isotopic composition of the surface relative to the calibrated atmosphere fluxes by employing the Miller-Tans (Miller & Tans, 2003) mixing model approach, which regresses the product of H_2O or CO_2 mixing ratios and the isotope composition of each atmospheric gases at each of the measurement heights against the respective mixing ratio for that gas (Good et al., 2012). The slope of the simple regression from this procedure estimated the isotope composition of the water and carbon fluxes. To estimate the daily isotopic value of each flux, we used the 9-minute calibrated isotope datasets across all measurement heights as the predictor of a Miller-Tans mixing model and the response was the product of the 9-minute atmospheric gas concentrations and the calibrated isotope data. We only used isotope ratios of the atmospheric gases which occurred during time periods where the incoming shortwave radiation was ≥ 10 Wm^{-2}. Importantly, this threshold constrained most of the isotope measurements to represent diurnal fluxes. This threshold can be updated in future versions of this product.

While we achieved reasonable results with the Miller-Tans approach, other mass balance mixing methods can be explored in future work to estimate the isotope composition of the water and carbon fluxes (e.g., Zobitz et al., 2006; Wehr & Saleska, 2015). At the time of this publication, the water isotope measurements were not corrected for low humidity deviations and the data corrected for low humidity was not available. Fortunately, here we were not focused on estimating isotope ratios at low humidity, but future work could apply these corrections to the data.

4.4 Data Records

All associated data, code and metadata are available in a public repository on HydroShare (Finkenbiner et al., 2021b). HydroShare, developed and maintained by the

Consortium of Universities for the Advancement of Hydrologic Science, Inc. (CUAHSI) and supported by the U.S. National Science Foundation, is a web-based hydrologic information system that allows users to publish and share data repositories in a citable manner.

4.4.1 Precipitation Flux Data Products

For the daily F_P, there are two data files containing time series of modeled δ^2H and $\delta^{18}O$ values corresponding to observed precipitation and a metadata file describing the quality of each data point. Each row in these files represents one calendar date and the columns are labeled with the NEON site abbreviation codes. Each column contains a daily time series of water isotope values where applicable. Days with no precipitation contain values of -9999. The precipitation flux metadata file contains quality flags for each value in a site's time series. A "0" indicates daily isotope value was associated with observed precipitation that was larger than the defined value for trace events (here 0.25 mm), a "1" indicates there was no precipitation data on that day, and a "2" indicates the observed precipitation was less than the defined value for trace events.

The precipitation downscaling techniques were successfully applied to sites with low (e.g., Onaqui in Utah (ONAQ)) and high (e.g., Wind River in Washington (WREF)) annual precipitation (Fig. 4.1a-d). Across all sites which could be statistically downscaled, an average of 23 biweekly observations were used in the downscaling method. The means and standard deviations of the downscaled precipitation isotope values varied depending on site-specific characteristics (e.g., seasonality, climate) accounted for within the downscaling methodology (Fig. 4.2a-d). Recorded in the metadata document, the sites with sufficient isotope observations had a minimum number of simulated daily isotope ratios of 70 days (0.05% of total days) and a maximum number of 531 days (0.39% of total days).

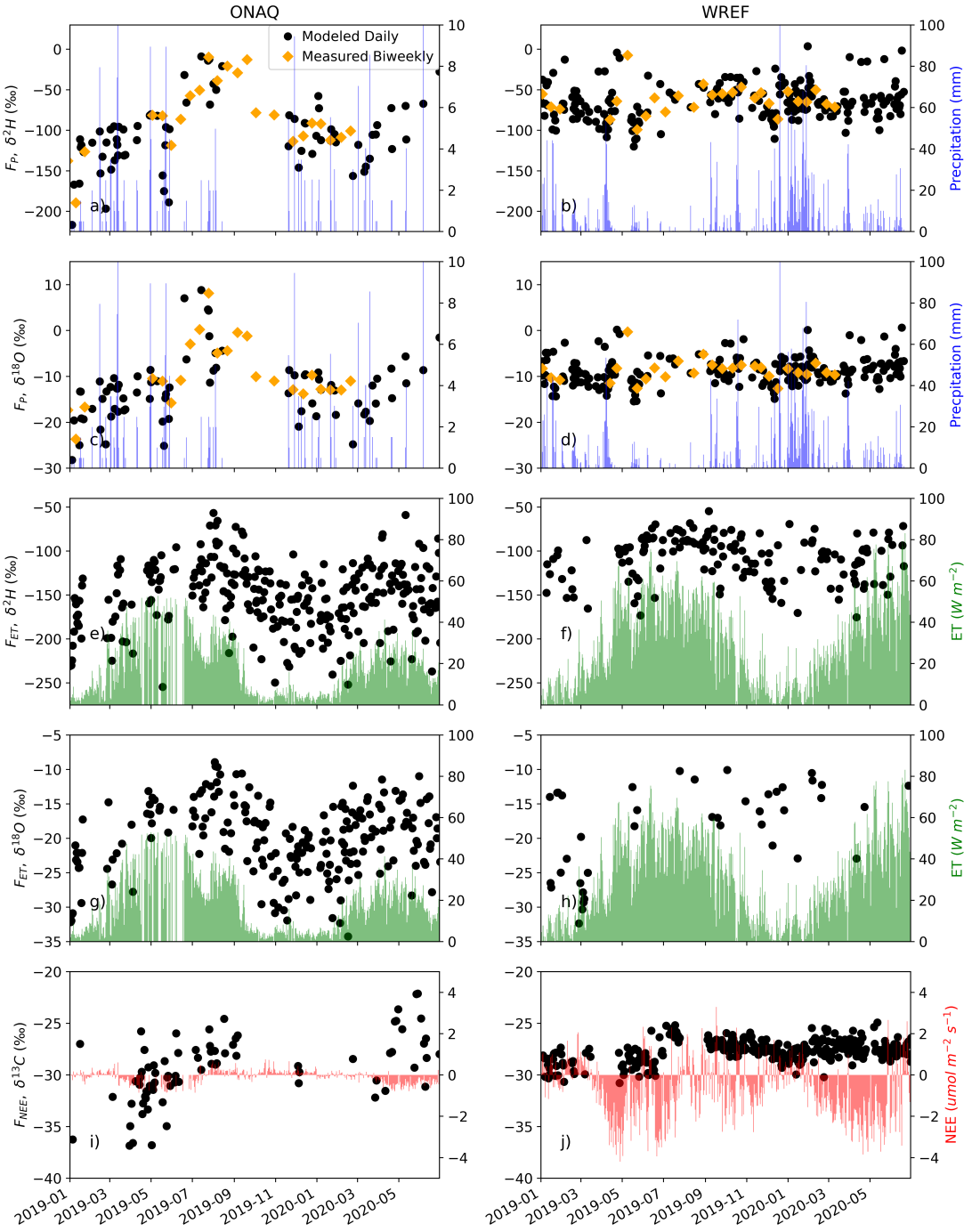

Figure 4.1. Time series at NEON sites Onaqui, UT (ONAQ - arid climate) and Wind River, WA (WREF - wet climate) of the a-d) downscaled daily and observed biweekly ratio of the flux in precipitation (F_P) and precipitation amount and e-j) daily isotope ratios of the ET and NEE water and carbon fluxes, along with Evapotranspiration (F_{ET}), and Net Ecosystem Exchange (F_{NEE}) fluxes for January 1, 2019 - June 30, 2020.

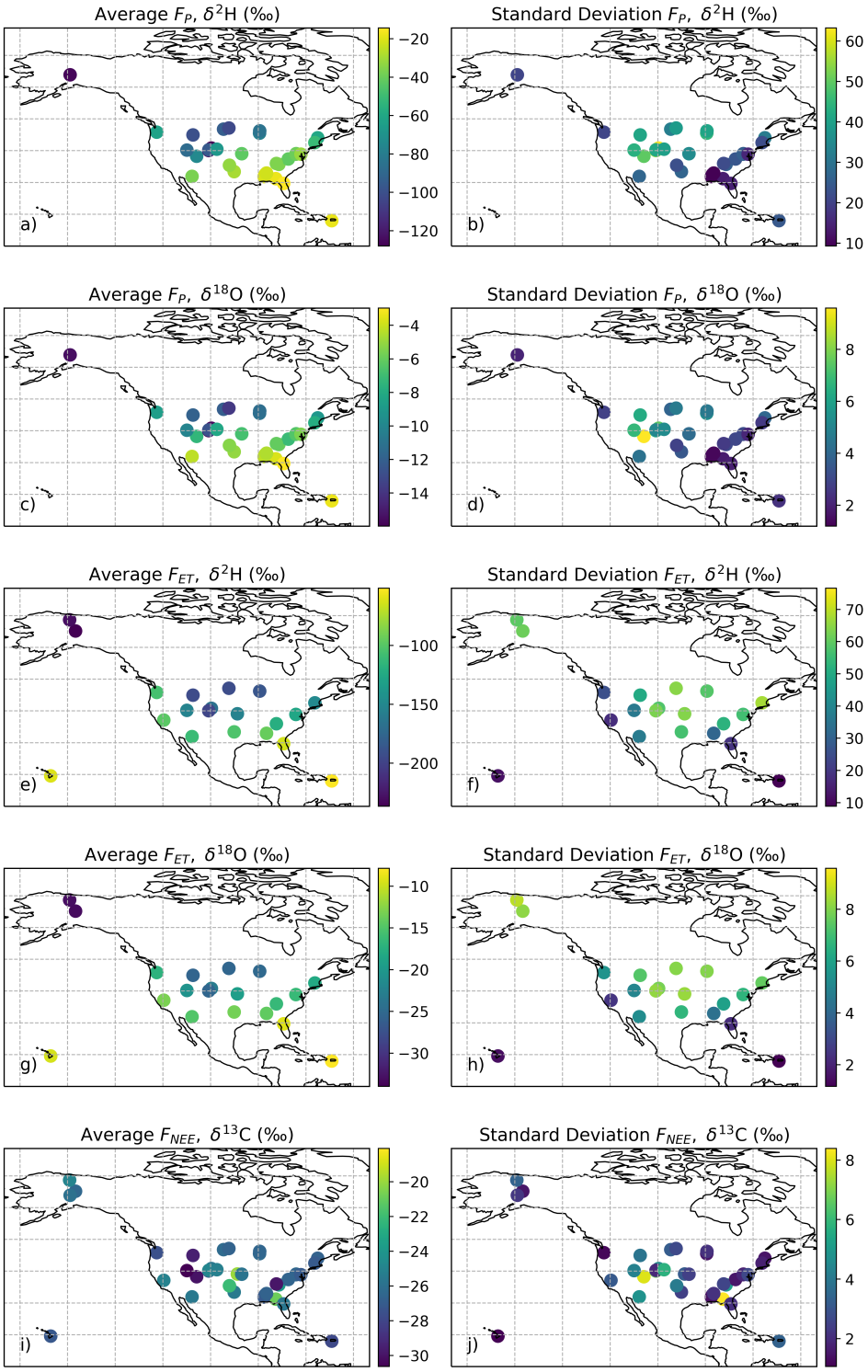

Figure 4.2. Average and standard deviation of each of the daily time series from each of the NEON site locations with a-d) precipitation flux (F_P) water isotopes, d-h) flux tower ET (F_{ET}) estimates of water isotopes, and i-j) NEE (F_{NEE}) of carbon isotopes.

4.4.2 Gas Flux Data Products

Water isotope ratios of the F_{ET} and carbon isotope ratios of the F_{NEE} are contained in three data files with row names consisting of the calendar date and column names corresponding to the four-letter abbreviation of each NEON site location (same as the F_P file format described above). The included F_{ET} and F_{NEE} metadata files contain data quality flags for each flux measurement. For each stable isotope time series, a value of -9999 was used to fill days when no calibrated isotope ratios were available, and this was marked with a "1" quality flag in the metadata file. A flag value of "2" was used if there was a low number ($n \leq 5$) of calibrated isotope values used to generate the daily flux values. A quality flag value of "3" was assigned when the Miller-Trans mixing model r-squared (R^2) was below 0.9. To identify cases where the interred point falls outside the range of observations, an interquartile (IQR) range flag was applied to each time series meeting the above criteria ($n \geq 5$, $R^2 \geq 0.9$); if the inferred isotope value of the flux was beyond the 1.5 times IQR of the 25th percentile (Q_1-1.5 IQR) and 75th percentile (Q_3+1.5 IQR) of the observation data, then a flag of "4" was assigned to those data points. A "0" quality flag was used to indicate a good isotope value of the flux estimated from the isotope ratios of the gases where $n \geq 5$ from the regression analysis, $R^2 \geq 0.9$, and the isotope value was within the desired interquartile. Users of these data products are encouraged to use the isotope values in the time series with a quality flag value of "0". The isotope ratios of the ET and NEE fluxes which passed all quality flags at ONAQ and WREF were shown in Fig. 4.1e-j, along with the fluxes themselves.

The site averaged (± standard deviation) isotope flux values ranged from -236.56 (61.31) ‰ to -51.40 (8.88) ‰ for δ^2H_{ET}, -33.97 (9.58) ‰ to -7.86 (1.17) ‰ for $\delta^{18}O_{ET}$, and -30.64 (4.26) ‰ to -18.08 (1.64) ‰ for $\delta^{13}C_{NEE}$ (Fig. 4.2e-j). Across all NEON sites, the number of $\delta^{18}O_{ET}$ and δ^2H_{ET} flux values that passed all quality flags ranged from 82 to 741 days (5 to 48% of total days) and 92 to 678 days (6 to 42% of total days), respectively. The number of $\delta^{13}C_{NEE}$ data points that passed all quality flags ranged from 37 to 861 days (2% to 58% of total days). However, calculated flux isotope ratios that did not pass quality flags might not necessarily be low quality. For example, atmospheric

conditions could be such that a two-member mixing model does not work. In this case, the raw data would be of high quality, but the Miller-Tans mixing model method would fail. Future work could investigate other methods besides the Miller-Tans method as to increase the number of data points that pass imposed quality flags.

4.5 Technical Validation

4.5.1 Precipitation Flux Data Products

The implemented statistical downscaling method was previously validated (Finkenbiner et al., 2021a) at 27 globally distributed sites from the International Atomic Energy (IAEA) Global Network of Isotopes in Precipitation (GNIP) database (IAEA, 2020). Downscaling biweekly observations to daily estimates cannot produce the true value (as these are unknown) but only statistically representative realizations. We quantified the uncertainty associated with the average of the daily precipitation estimates by calculating the standard deviation of each precipitation event across an ensemble of 10 precipitation time series at each site (Fig. 4.3). The average standard deviations ranged from 2.4 to 9.5 ‰ for δ^2H values and 0.3 to 1.6 ‰ for $\delta^{18}O$ values across sites. Sites with larger seasonal variability have larger standard deviations. The dataset provided here contains a single realization of the estimated daily precipitation's isotopic composition based on the statistics of a coarser resolution observation time series (here biweekly observations). Depending on the application of the daily isotope ratios, generating an ensemble of daily time series may be advantageous to capture impacts of the standard error as a function of time or space. To generate ensemble sets, the published python script, which generates a single random realization of the daily precipitation water isotope data product, can be run numerous times.

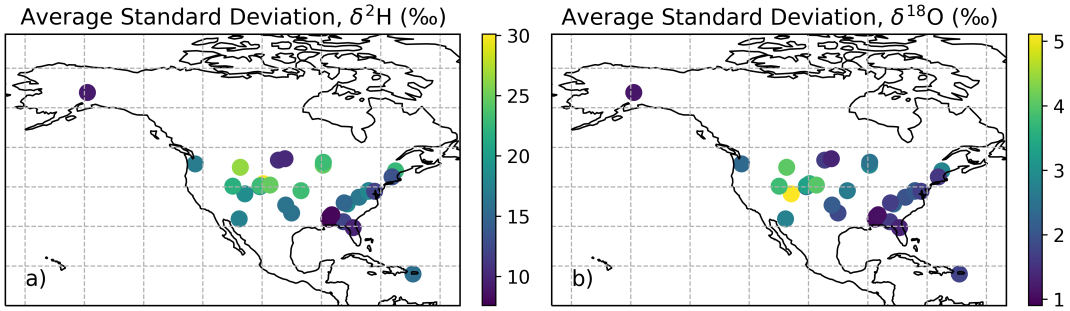

Figure 4.3. Standard deviation of the daily precipitation flux's (F_P) isotope ratio averaged across 10 daily time series generated at each of the NEON site locations. Each point represents the expected variance for each day in the time series across 10 downscaled realizations.

4.5.2 Gas Flux Data Products

The generation of calibrated isotope ratios associated with the atmospheric carbon dioxide flux were validated by Fiorella et al. (2021; with an accuracy of 0.11‰ and precision of ~0.4‰) and here similar procedures were used for the atmospheric water vapor ratios. Within the context of a simplified mixing model source estimation approach, uncertainty in the estimation of the isotope composition of surface-atmosphere fluxes is associated with accuracy of isotope measurements themselves and the range of atmospheric carbon dioxide and water vapor concentrations observed during the averaging interval (Good et al., 2012). The average of the daily standard error in the mixing model regression slope is shown in Fig. 4.4 for the F_{ET} and Fig. 4.5 for the F_{NEE}. These standard errors represent the uncertainty associated with estimation of the isotope ratio of the F_{ET} and F_{NEE} within the mixing model framework. The mean of the standard error of the Miller-Tans model slope across all sites ranged from 1.27 (+/- 0.63) to 5.33 (+/- 3.50) for δ^2H, from 0.19 (+/- 0.09) to 0.84 (+/- 0.56) for δ^{18}O, and from 0.14 (+/- 0.07) to 0.62 (+/- 0.22) for δ^{13}C.

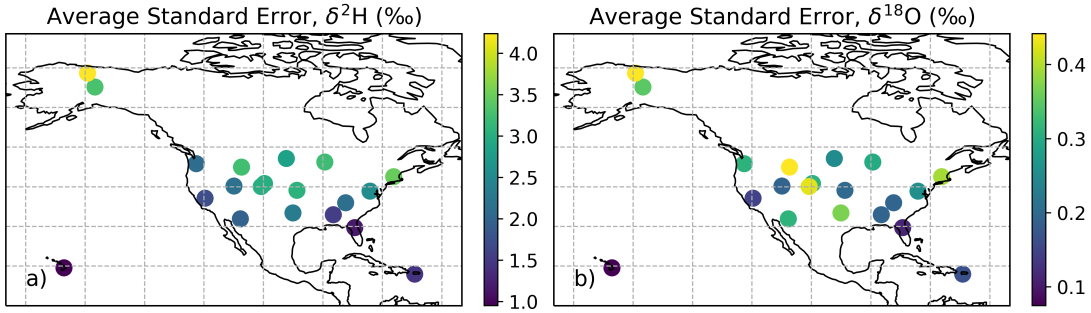

Figure 4.4. Standard error of the flux tower ET (F_{ET}) estimates of water isotopes averaged across time at each NEON site.

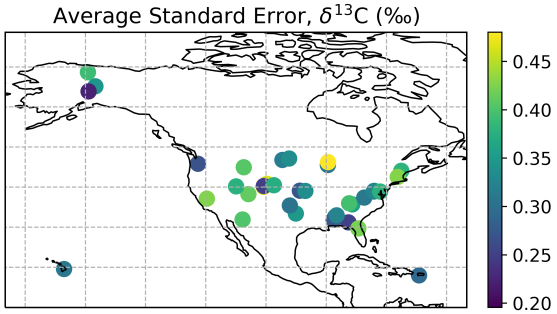

Figure 4.5. Standard error of the flux tower NEE (F_{NEE}) estimates of carbon isotopes across time at each NEON site.

4.6 Usage Notes

Water isotope ratios of F_P are contained in two CSV files containing time series of δ^2H ("daily_p_flux_d2H.csv") and δ^{18}O ("daily_p_flux_d18O.csv") ratios corresponding to observed precipitation. Both correspond to the same metadata file ("daily_p_flux_metadata.csv") describing the quality of each data point. The script "Estimate_daily_p_flux_iso.py" will implement the complete statistical downscaling method[22] and save daily water isotope time series which correspond to observed daily precipitation amounts at each NEON site to comma-separated values (CSV) files. The user can change which site data are analyzed and how many ensembles are generated. Additionally, the user can change the "precip_filter" variable to change the magnitude of

the precipitation events which will be filtered out of the downscaling method and consequently update the output time series and metadata files.

Water isotope ratios of the F_{ET} and carbon isotope ratios of the F_{NEE} are contained in three CSV files ("daily_et_flux_d2h.csv", "daily_et_flux_d18o.csv", and "daily_nee_flux_d13c.csv"). Each correspond to a metadata file ("daily_et_flux_d2h_metadata.csv", "daily_et_flux_d18o_metadata.csv", and "daily_nee_flux_d13c_metadata.csv") describing the quality of each data point. The script "Estimate_daily_et_nee_flux_iso.py" will implement all the calibration procedures for water and carbon isotope ratios and save the daily isotope time at each NEON site to CSV files. For the F_{ET} and F_{NEE} fluxes, the user can adjust the minimum number of the data points used in the Miller-Tans mixing model, adjust the threshold value of the R^2 regression, and implement other filters besides the IQR filtering. The F_{ET} and F_{NEE} flux isotope composition estimation procedure for $\delta^{13}C$, $\delta^{2}H$, and $\delta^{18}O$ were done by leveraging the R scripts "mixing_model_d13c_by_month.R", "mixing_model_d2h_by_site.R", and "mixing_model_d18o_by_site.R", respectively.

4.7 Code Availability

Python and R code and generated CSV files are available on HydroShare (Finkenbiner et al., 2021b). For the NEON data processing packages, refer to the NEONiso package (Lunch & Laney, 2020) found at https://github.com/SPATIAL-Lab/NEONiso/tree/0.4.0.

4.8 Acknowledgements

The authors acknowledge the support of the United States National Science Foundation (DEB-1802885, DEB-1802880, NSF-1954660). This project was partially funded by E.R. Jackman Alumni and Friends and the Beginning Undergraduate Researcher Support Program, College of Agricultural Sciences, Oregon State University.

4.9 References

Abbott, B. W. et al. Using multi-tracer inference to move beyond single catchment ecohydrology. *Earth-Sci. Rev.* **160**, 19-42 (2016).

Allen, S. T., Kirchner, J. W., & Goldsmith, G. R. Predicting spatial patterns in precipitation isotope (δ2H and δ18O) seasonality using sinusoidal isoscapes. *Geophys. Res.*, **45**, 4859–4868 (2018).

Al-Oqaili, F., Good, S. P., Frost, K., & Higgins, C.W. Differences in soil evaporation between row and interrow positions in furrowed agricultural fields. *Vadose Zone J.* 19:e20086 (2020).

Bowen G. J., Cai, Z., Fiorella, R. P., & Putman, A. L. Isotopes in the water cycle: Regional- to global-scale patterns and applications. *Annu. Rev. Earth Planet. Sci.* **47**, 453–479 (2019).

Bowen, G. J. & Good, S. P. Incorporating water isotopes in hydrological and water resource investigations. *Wiley Interdiscip. Rev.: Water*, **2**, 107–119 (2015).

Brooks et al. Stable isotope estimates of evaporation: Inflow and water residence time for lakes across the United States as a tool for national lake water quality assessments. *Limnol. Oceanogr.,* **59**, 2150–2165 (2014).

Chai et al. Stable water isotope and surface heat flux simulation using ISOLSM: Evaluation against *in-situ* measurements. *J. Hydrol.* **523**, 67-78 (2015).

Craig, H. Isotopic variations in meteoric waters. *Science* **133**, 1702–1703, (1961).

Dansgaard, W. Stable isotopes in precipitation. *Tellus*, **16**, 436–468 (1964).

Finkenbiner, C. E., Good, S. P., Allen, S. T., Fiorella, R. P., & Bowen, G. J. A statistical method for generating temporally downscaled geochemical tracers in precipitation. *J. Hydrometeorol.* **22,** (2021a).

Finkenbiner, C. et al. (2021b). Datasets of Daily Water and Carbon Stable Isotope Ratios for Precipitation, Evapotranspiration, and Net Ecosystem Exchange Fluxes at NEON Sites, HydroShare, http://www.hydroshare.org/resource/e74edc35d45441579d51286ea01b519f

Fiorella, R. et al. Calibration Strategies for Detecting Macroscale Patterns in NEON Atmospheric Carbon Isotope Observations. *J. Geophys. Res. Biogeosci.* **126**, (2021).

Good, S. P., Noone, D., & Bowen, G. Hydrologic connectivity constrains partitioning of global terrestrial water fluxes. *Science* **349**, 175–177 (2015).

Good, S. P., Soderberg, K., Wang, L., & Caylor, K. K. Uncertainties in the assessment of the isotopic composition of surface fluxes: A direct comparison of techniques using laser-based water vapor isotope analyzers. *J. Geophys. Res. Atmos.* **177** (2012).

Gupta, A., Gerber, E. P., & Lauritzen, P. H. Numerical impacts on tracer transport: A proposed intercomparison test of atmospheric general circulation models. *Quart. J. Roy. Meteor. Soc.* **146**, 3937–3964 (2020).

IAEA, 2020: Global network of isotopes in precipitation. https://www.iaea.org/services/networks/gnip.

Kanner, L. C., Buenning, N. H., Stott, L. D., Timmermann, A., & Noone, D. The role of soil processes in d18O. *Global Biogeochem. Cycles* **28,** 239–252 (2014).

Krause, P., Boyle, D. P., & Bäse, F. Comparison of different efficiency criteria for hydrological model assessment. *Adv. in Geosci.* **5***,* 89-97 (2005).

Lee, R. and S. Weintraub. NEON User Guide to Stable Isotopes in Precipitation (NEON.DPI.00038) Version B. NEON (National Ecological Observatory Network). (2021).

Lu, X. et al. Partitioning of evapotranspiration using a stable isotope technique in an arid and high temperature agricultural production system. *Agric. Water Manag.* **179** 103-109 (2017).

Lunch, C. K. & Laney, C. M. NEON (National Ecological Observatory Network). neonUtilities: Utilities for working with NEON data. R package version 1.3.4. https://github.com/NEONScience/NEON-utilities (2020).

McGuire, K. J. & McDonnell, J. J. A review and evaluation of catchment transit time modeling. *J. Hydrol.* **330,** 543–563 (2006).

Miller, J. B., & Tans, P. P., Calculating isotopic fractionation from atmospheric measurements at various scales. *Tellus,* **55**, (2003).

NEON (National Ecological Observatory Network). Precipitation (DP1.00006.001). https://data.neonscience.org (2021).

NEON (National Ecological Observatory Network). Stable isotopes in precipitation (DP1.00038.001). https://data.neonscience.org (2021).

NEON (National Ecological Observatory Network). Bundled data products - eddy covariance (DP4.00200.001). https://data.neonscience.org (2021).

Pataki, D. E. et al., The application and interpretation of Keeling plots in terrestrial carbon cycle research. *Global Biogeochem. Cycles*, 17 (2003).

Remondi, F., Kircher, J. W., Burlando, P., & Fatichi, S. Water flux tracking with a distributed hydrologic model to quantify controls on the spatio-temporal variability of transit time distributions. *Water Resour. Res.* **54**, 3081–3099 (2018).

Sklar, A. Fonctions de répartition à n dimensions et leurs marges. *Publ. Inst. Stat. Univ. Paris.* **8**, 229–231 (1959).

Sprenger, M. et al. The demographics of water: A review of water ages in the critical zone. *Rev. Geophys.* **57**, 800–834 (2019).

Turnadge, C. & Smerdon , B. D. A review of methods for modelling environmental tracers in groundwater: Advantages of tracer concentration simulation. *J. Hydrol.* **519**, 3674–3689 (2014).

Wieser G. et al. Stable water use efficiency under climate change of three sympatric conifer species at the alpine treeline. *Front. Plant Sci.* **7**, 799 (2016).

Wehr, R., & Saleska, S. R. An improved isotopic method for partitioning net ecosystem-atmosphere CO2 exchange. *Agric For Meteorol.* **214**, 515– 531 (2015).

Wu, Y. et al. Stable isotope measurements show increases in corn water use efficiency under deficit irrigation. *Sci Rep* **8**, 14113 (2018).

Xiao, W., Wei, Z., & Wen, X. Evapotranspiration partitioning at the ecosystem scale using the stable isotope method—A review. *Agric For Meteorol.* **263**, 346-361 (2018).

Zobitz, J. M., Keener, J.P., Schnyder, H., & Bowling, D. R. Sensitivity analysis and quantification of uncertainty for isotopic mixing relationships in carbon cycle research. *Agric For Meteorol.* **136** ,56-75 (2006).

Chapter 5. Leveraging New Water Isotope Datasets to Constrain Uncertainties in Modeled Evapotranspiration Estimates

5.1 Abstract

Estimates of the component fluxes of the hydrologic cycle (plant transpiration, soil evaporation, overland flow, subsurface percolation, etc.) inform approaches to agriculture, water resources, and ecological issues; yet calibration of models representing these fluxes is principally based on bulk evapotranspiration and discharge measurements. Recent studies have noted significant disparities exist amongst estimates of component fluxes. While geochemical tracers such as stable water isotope ratios (δ^2H, δ^{18}O) have been used to constrain estimates, lack of data has hindered inter-model assessment at large scales and across ecosystems. Here we investigated hydrologic fluxes for three leading land surface models (LSMs) using observation datasets of isotope ratios in precipitation and atmospheric water vapor at 14 sites across the United States from the National Ecological Observatory Network (NEON). Statistically downscaled precipitation δ^2H and δ^{18}O values were used as conservative tracers within a mass balance model built from LSM specified output fluxes that tracked δ values for different components. Simulated δET was aggregated from flux components and directly compared to daily δET observations created from calibrated NEON tower measurements of atmospheric water vapor. An inter-model comparison suggested distinct differences exist amongst simulated δET across North American ecosystems and this can be associated with disparities in the relative contributions of interception, plant transpiration, and soil evaporation to the total ET. Our results indicate conservative tracers allow for better tracking of the uncertainties associated with inferences drawn from LSM outputs and provide additional validation metrics on which to evaluate model performance. LSM representations of the ET can greatly impact water and energy balance simulations used in large-scale hydrologic and global climate modeling. We predict our findings can improve the general understanding of land-surface processes influencing the water and carbon cycle from regional to global scales.

Chapter 5.2 Introduction

The earth science community has developed countless models representing various components of the water and energy balance (Overgaard et al., 2006). Many different model structures and parameter sets can yield reasonable results when validated against a predefined objective function (often bulk fluxes). This leads to model equifinality in space (Wagener et al., 2009; Herman et al., 2013; Moreau et al., 2013) and time (Franks et al., 1998; Ghasemizade et al., 2017; Guse et al., 2016; Kelleher et al., 2015; van Werkhoven et al., 2008; Zhang et al., 2013) and poses serious challenges for model improvement (Kelleher et al., 2017; Beven, 2000). Land-Surface Models (LSMs) are based on a solution of the energy balance equation at the land surface and offer an effective way to generate spatially and temporally continuous estimates of evapotranspiration (*ET*) and its partitions (Kumar et al., 2018; Miralles et al., 2016; Overgaard et al., 2006). However, large uncertainties exist in LSM *ET* estimates. Identifying and constraining these uncertainties is difficult due to deficiencies in model structures (e.g., representations of the subsurface), input and output measurements a model is validated against (e.g., precipitation and stream discharge; Moradkhani et al., 2005, Renard et al., 2010), and physically unrealistic calibration parameters resulting in low model error (Muñoz et al., 2015). A recent study by Kumar et al. (2018) compared a suite of state-of-the-art LSMs and exposed large disagreements in partitions of various water balance components across the contiguous United States. Across LSMs, large uncertainties were calculated in modeled partitions of the total *ET* with transpiration accounting for 29.9 to 83.0 % of total *ET* (Kumar et al., 2018).

We postulated a new dataset with stable isotope ratios of water fluxes across the United States could be used to provide novel constraints on LSM estimates of hydrologic components, as well as provide supportive metrics for understanding modelled feedbacks between the land surface and atmosphere (Chai et al., 2015; Brooks et al., 2014; Good et al., 2015; Gupta et al., 2020; Kanner et al., 2014; Remondi et al., 2018). Natural tracers, like stable water isotopes, provide additional points of comparison between observed and modelled environmental pools and fluxes (Abbott et al., 2016) and aid in the evaluating

the performance and efficiency of a modelling approach (Krause et al., 2005). The stable water isotope ratios of hydrogen ($^{2}H/^{1}H$) and oxygen ($^{18}O/^{16}O$), hereafter expressed as $\delta^{2}H$ and $\delta^{18}O$ (Krause et al., 2005; Bowen et al., 2015; McGuire and McDonnell, 2006; Sprenger et al., 2019; Turnadge and Smerdon, 2014; Fiorella et al., 2021), are commonly used to study land surface processes from local to global scales and provide useful information for partitioning ET into evaporation and transpiration at the ecosystem scales (Good et al., 2015; Xiao et al., 2018).

In this study, we leveraged observation datasets of stable water isotopes to evaluate the uncertainties in hydrologic partitioning the three operational land surface models: Noah (version 2.8; Chen et al., 1996; Ek et al., 2003; Xia et al., 2012), Mosaic (Koster and Suarez, 1992, 1996), and Variable Infiltration Capacity (VIC; Liang et al., 1994) as implemented in the operational North American Land Data Assimilation System Phase 2 (NLDAS-2) configuration (Xia et al., 2012). Noah, Mosaic, and VIC are all validated against observation-based meteorological data (Xia et al., 2012) and provide reasonable estimates of the bulk ET and discharge fluxes (Zhang et al., 2020). Yet, all have striking differences in their ET partitions of evaporation, transpiration, and interception (Kumar et al., 2018) and discharge estimates of subsurface and overland flow. We hypothesized that incorporating stable water isotopes as tracers into a mass balance model built from Noah, Mosaic, and VIC output fluxes would allow us to constrain the uncertainty in ET and provide guidance toward model selection. Stable water isotope ($\delta^{2}H,\ \delta^{18}O$) observation datasets of precipitation and ET fluxes were leveraged from 14 sites across the United States from the National Ecological Observatory Network (NEON) within a tracer mass balance that simulated stable water isotope concentrations (δ) for input precipitation and outputs of hydrologic flux component: evaporation from the bare soil, transpiration, interception loss, sublimation, subsurface drainage, surface runoff, and storage. Simulated δET was directly compared to daily δET observations, which were calibrated from NEON tower measurements of atmospheric water vapor. Specific research questions included: 1) Do the different ET partitions assumed by Noah, Mosaic, and VIC LSMs result in distinct differences amongst simulated δET? 2) Can stable water isotopes add additional metrics to evaluate

and constrain uncertainties in δET compared to bulk fluxes? 3) Can we use simulations of δET to move toward improved model selection for representing land-surface fluxes from a site-level to global scale?

5.3 Stable Water Isotope Observation Datasets

We utilized all datasets from National Ecological Observatory Network (NEON) sites (https://data.neonscience.org) with long-term records of stable water isotope measurements for precipitation and atmospheric water vapor, resulting in the 14 sites used in this analysis to evaluate our δET flux simulations (refer to *Supplemental Materials* Table 5.S1). The NEON provides open-access measurements of stable isotope ratios (δ^2H, $\delta^{18}O$) in atmospheric water vapor (refer to NEON product number DP4.00200.001) at different tower heights, as well as aggregated biweekly precipitation collections (refer to NEON product number 1.00038.001) across the United States. These 14 sites were included in a new data product (Finkenbiner et al., 2021b) which calibrates, validates, and translates the raw NEON data products to daily estimates of δ^2H and $\delta^{18}O$ associated with the precipitation and evapotranspiration fluxes. An associated data descriptor to Finkenbiner et al. (2021b) is in review with *Scientific Data*. A brief description of the methods used by Finkenbiner et al. (2021b) is provided below.

5.3.1 Stable Water Isotopes of the Precipitation Flux

The NEON biweekly precipitation collections were statistically downscaled to daily resolutions to simulate stable water isotope ratios representative of the observed precipitation's mean, standard deviation, and correlation structures following a method detailed and validated by Finkenbiner et al. (2021b). Python scripts from Finkenbiner et al. (2021b) were written based on the methods from Finkenbiner et al. (2021a) and we adapted those Python scripts to generate daily stable water isotope values associated with each daily NLDAS precipitation amount (δP). One-hundred precipitation stable water isotope time series were generated at each NEON site and served as input representative of the site's natural seasonal and stochastic variability. Additionally, by generating 100

representative time series the presented results are not tied to one input time series and we effectively simulated a representative precipitation tracer signal at each site.

5.3.2 Stable Water Isotopes of the Evapotranspiration Flux

The NEON atmospheric isotope measurements represent the stable water isotope composition of the gases at specific measurement layers and therefore must be manipulated to reflect the isotope composition of the latent heat flux at ecosystem scales. We calibrated atmospheric isotope measurements following Fiorella et al. (2021) and then estimated the daily isotopic composition of the evapotranspiration flux (δET) based on a Keeling plot approach, which uses the isotope composition of the mole fractions of H_2O (Pataki et al., 2003). Specifically, we applied a commonly used Miller-Tans mixing model (variant of the Keeling plot approach; Miller and Tans, 2003) using python and R scripts from Finkenbiner et al. (2021b). The Miller-Tans mixing model estimates the isotope ratio of ecosystem scale fluxes by fitting a linear regression between the product of the mole fraction and the isotopic ratio of the atmospheric gases at all measurement heights (Miller and Tans, 2003). The slopes of these regression lines are the estimates of the isotopic composition of the latent heat fluxes. Refer to Finkenbiner et al. (2021b) for more details on the calibration and estimation of the δP and δET flux datasets used in the subsequent analysis.

5.4 Materials and Methods

5.4.1 Isotope-enabled Mass Balance Model (isoMB) Description

NLDAS-2 Noah-2.8, Mosaic, and VIC-4.0.3 LSM hourly forcing and output files (downloaded from https://ldas.gsfc.nasa.gov/nldas) were aggregated to represent daily fluxes from January 1, 2018 to December 31, 2020, a total of three full years. All three LSMs employ similar physics components with different parameterizations for soil hydrology, canopy interception, soil thermodynamics, and snowpack physics (Kumar et al., 2017; Xia et al., 2012). A mass balance model was built from daily Noah, Mosaic,

and VIC LSM fluxes to represent a water balance with the storage (S) at the next timestep defined as:

$$S_{i+1} = S_i + P_i - Q_i - L_i - E_{cw_i} - E_{sub_i} - E_{bs_i} - T_i \quad (1)$$

where i is the current time step, P is incoming precipitation as rainfall and snow, Q is surface runoff (i.e., overland flow), L is subsurface drainage, E_{cw} is evaporation from canopy water interception, E_{sub} is evaporation from sublimation, E_{bs} is evaporation from the bare soil, and T is evaporation from transpiration. The mass balance model (1) was validated against Noah, Mosaic, or VIC storage outputs, where S_{i+1} was confirmed to be equal to the LSM storage output at i+1.

The Isotope-enabled Mass Balance Model (isoMB) associated stable water isotope concentrations (δ) with incoming precipitation (P), each ET partition (E_{cw}, E_{sub}, E_{bs}, T), subsurface drainage (L), surface runoff (Q), and storage (S) flux in (1). The simulated daily stable water isotope concentrations (refer to Section 2) were conditioned on NLDAS-2 Forcing precipitation amounts and served as input to the isoMB. Storage was isotope ratios at the next timestep were defined as:

$$\delta S_{i+1} \cdot S_{i+1} = \delta S_i \cdot S_i + \delta P_i \cdot P_i - \delta P_{i'} \cdot Q_i - \delta S_i \cdot L_i - \delta P_{i'} \cdot E_{cw_i} - \delta S_i \cdot E_{sub_i} - \delta E_{bs_i} \cdot E_{bs_i} - \delta S_i \cdot T_i \quad (2)$$

where i' references the isotope concentration of the most recent precipitation event for days when no precipitation occurred. The isoMB calculated stable water isotope concentrations for each mass balance component (storage and fluxes) at every time step.

5.4.2 isoMB Model Initial Conditions and Parameter Assumptions

We ran isoMB at each of the 14 NEON sites with 100 simulations of stable water isotopes in precipitation on the National Center for Atmospheric Research (NCAR) high-performance system (Computational and Information Systems Laboratory, 2019). The initial stable water isotope concentration of the storage term (S_0) was unknown, so we assumed δS_0 was equal to the weighted average isotope concentration of a NEON site's observed precipitation. isoMB was ran three times for 2018-2020 (9 years total) and only the isoMB outputs for the last 3 years (after the 6-year warm-up period) were analyzed

for the subsequent analyses. For days with Q or E_{cw} fluxes but no input precipitation, we assumed each flux had the isotopic concentration of the most recent precipitation event (*i'* in (2)). We assumed that fractionation during sublimation was negligible (Noone and Sturm, 2010) and that kinetic fractionation from the soil surface does not occur when the skin temperature was below freezing (Dee et al., 2015). Hydrologic connectivity of the subsurface was randomly varied among model runs, similar to Good et al. (2015), thus simulating heterogenous landscape porosities and variable mixing in the subsurface. We defined hydrologic connectivity as Fractionation effects on the evaporative flux from the bare soil (E_{bs}) were quantified using the Craig-Gordon equations (Gat, 2008) and followed methods from numerous studies who have employed these techniques in other hydrologic modeling frameworks (Good et al., 2015; Soderberg et al., 2012; Horita et al., 2008; Dee et al., 2015). The kinetic fractionation parameter was randomly generated from a uniform normal distribution, similar to Good et al. (2015), to simulate varying degrees of fractionation between δS and δE_{bs} at each site. δT is assumed to be equal to δS and this is consistent with a steady-state assumption of the transpiration flux. The isoMB captured a breath of mass balance scenarios at each NEON site, as it was run with 100 unique δP time series, variable degrees of kinetic fractionation, and variable subsurface mixing.

5.4.3 isoMB Model Evaluation

We calculated a δET value at each time step from the isoMB outputs as the flux weighted combination of the component fluxes as:

$$\delta ET_i = \frac{\delta E_{cw_i} \cdot E_{cw_i} + \delta E_{sub_i} \cdot E_{sub_i} + \delta E_{bs_i} \cdot E_{bs_i} + \delta T_i \cdot T_i}{E_{cw_i} + E_{sub_i} + E_{bs_i} + T_i}. \quad (3)$$

The 100 isoMB outputs of δET were compared to the δET modeled fluxes from each NEON site's flux tower observations (refer to Section 2.1). We calculated the absolute error (E, ‰) in the mean (μ) and standard deviations (σ) relative to observed δET as:

$$E_\mu = | \mu_{obs} - \mu_{isoMB} | \quad (4a)$$

$$E_\sigma = | \sigma_{obs} - \sigma_{isoMB} |. \quad (4b)$$

The cross correlation between the isoMB outputs and observed time series of δET was calculated using a Pearson correlation coefficient (ρ), this assumed a 0-day lag. A high ρ indicated the time series were highly correlated and the LSM flux partitions in the isoMB better represented the observed mean, standard deviation, and seasonality in the δET flux. Lastly, E_μ and E_σ were compared against the average transpiration divided by total *ET* flux (*T/ET*), subsurface drainage divided by total runoff (i.e., subsurface and surface runoff; *L/(L+Q)*), and ρ to provide guidance toward model selection at each NEON site.

5 Results and Discussion

5.5.1 Evaluation of Spatial and Temporal Patterns from isoMB Outputs

Noah, Mosaic, and VIC assume different model structures and forms. The partitions of the hydrologic fluxes at any given time step are calculated using (2), thus resulting in different expected δET values from the isoMB. Figure 5.1 shows example time-series estimates of δET at Onaqui, UT (ONAQ), Wind River Experimental Range, WA (WREF), Harvard Forest, MA (HARV), and Smithsonian Conservation Biology Institute, VA (SCBI). Of the three LSMs investigated, VIC assumes the most transpiration (Kumar et al., 2018). Fractionation only occurred in the isoMB on water isotopes in the evaporative component from the bare soil (E_{bs}) where we assumed lighter (more negative) water isotopes preferentially evaporated and left behind heavier (less negative) water isotopes in the storage term (refer to *Section 5.4.2* for more details). Thus, VIC partitioned fluxes produce the least fractionated δET flux and this δET most closely represents δS. At any given time step in the isoMB, δET was only more negative than δS if the evaporative component from interception loss (E_{cw}) was more negative than δS (i.e., the last input precipitation was more negative than δS) or if E_{bs} occurred resulting in a fractioned component of the ET flux. At these 14 NEON sites, VIC performed best at sites like WREF (Figure 5.1b, refer to *Supplemental Materials* Table 5.S1 for site descriptions and characteristics) with high biomass, high leaf-area indexes, and large pant canopies, as well as a relatively weak seasonal signal in the isotopic

composition (Figure 5.1b). Across sites, Noah assumed the most bare soil evaporation. The Noah isoMB simulated δET had the largest standard deviation and best represented the seasonality in the δET flux at sites like ONAQ, HARV, and SCBI (Figure 5.1a,c,d).

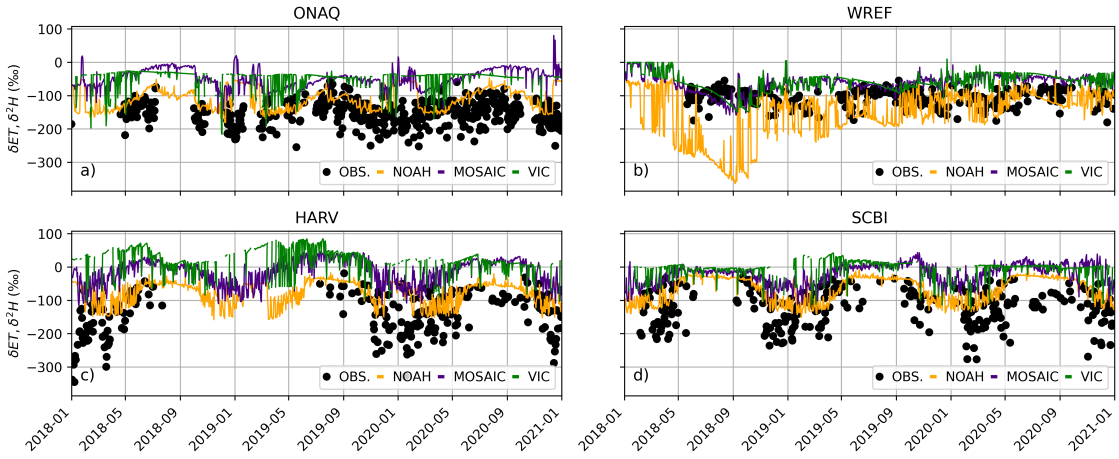

Figure 5.1. Time series of flux tower estimates of δET (black circles) and isoMB simulations of δET for NOAH (orange), MOSAIC (indigo), and VIC (green) for the NEON sites a) Onaqui, UT (ONAQ), b) Wind River Experimental Range, WA (WREF), c) Harvard Forest, MA (HARV), and d) Smithsonian Conservation Biology Institute, VA (SCBI). Refer to *Supplemental Materials* Table S1 for more details on each NEON site.

Across LSMs, sites closer to the coast have lower errors in the mean (E_μ) δET and Noah has the lowest E_μ (Figure 5.2a-c). Compared to Noah, both Mosaic and VIC had lower E_μ at WREF, the site with the most annual precipitation (= 2225 mm) and the highest plant canopy height (= 50 m; refer to *Supplemental Materials* Table S1). None of the LSMs best captured the standard deviation of the δET flux across sites (Figure 5.2d-f). Sites with high errors in the standard deviation of δET have either over or underestimated the fractionation associated with the E_{bs} flux or interception loss. Furthermore, means and standard deviations further from the average δS were simulated by at sites with more soil evaporation. At WREF, the errors in the standard deviation were highest for Noah because Noah assumed higher E_{bs}. Across sites, simulated and observed δET usually had higher cross correlations (ρ) with Noah isoMB outputs. This suggests the seasonality in the isotope signal was best captured by Noah (Figure 5.2g-i).

NEON sites located on the east coast had the highest ρ across LSMs and sites in the western US located in mountainous or snowy regions were more poorly correlated to the flux tower estimates of δET (Figure 5.2g-i).

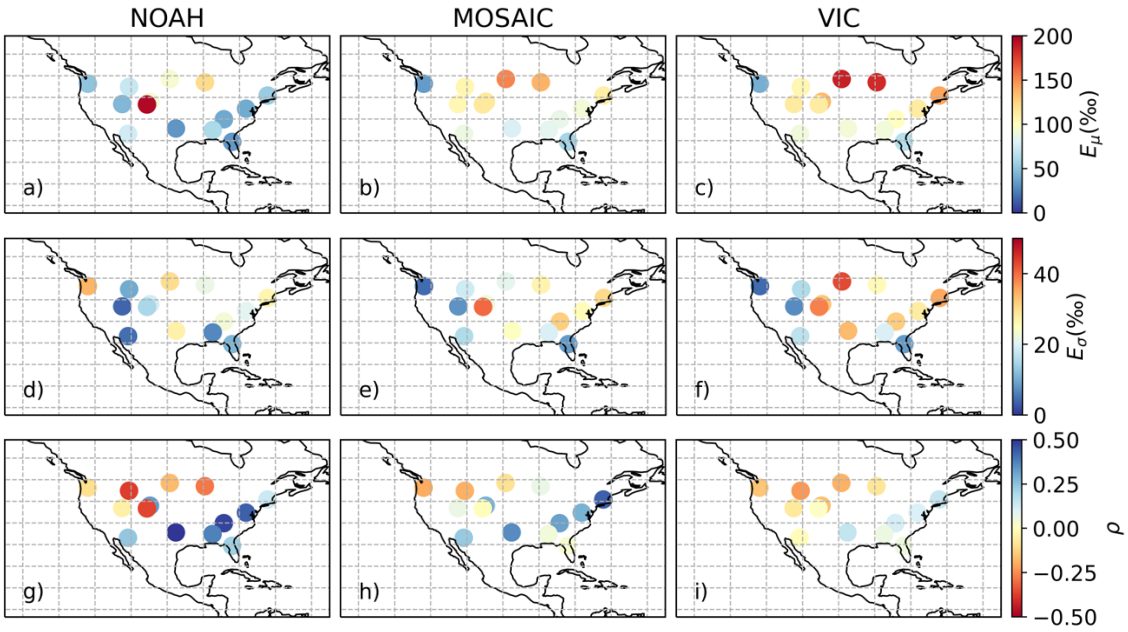

Figure 5.2. Average Absolute Error (E) in the a-c) mean (μ), d-f) standard deviation (σ), and g-i) cross-correlation coefficient (ρ) between the observed and isoMB simulated δET from a,d,g) Noah, b,e,h) Mosaic, and c,f,i) VIC across the 14 NEON sites.

5.5.2 Moving Toward Improved Hydrologic Modeling

Total site incoming precipitation drives LSM components representing overland runoff, subsurface flow dynamics, and each component of the ET flux (Figure 5.3). For each of the 100 simulations the same unique time series of generated δP inputs, kinetic fractionation parameters, and hydrologic connectivity was specified for the isoMB with Noah, Mosiac, and VIC outputs. So, differences in variance in δEToutputs across models are directly traced back to how each model partitions its mass balance components. Sites with less precipitation had less variance in the errors in the mean (E_μ) δET across the 100 simulations of Noah, Mosaic, and VIC isoMB (Figure 5.3a). This could indicate that at sites which experience more precipitation the larger, more negative precipitation events

drive larger variances in the evaporative flux. Across sites, Noah isoMB δET simulations had the lowest E_μ and error in the standard deviation (E_σ; Figure 5.3a,b). Noah Mosaic, and VIC are better at capturing the standard deviation of the δET flux than the mean, since $E_\sigma$was significantly lower than E_μ across models (Figure 5.3a,b). ρ was variable across LSMs. The highest ρ was calculated at sites with moderate precipitation and Noah usually had the highest ρ of the three LSMs (Figure 5.3c). ρ was relatively low at the two sites with the most precipitation (YELL and WREF). We acknowledge some of our reported errors may be a result of how the isoMB represents evaporation from canopy interception or sublimation, since δE_{cw} is not exactly equal to δP and δE_{sub} is not exactly equal to δS. However, this method offers unique insights and provides an additional metric on which to evaluate LSM outputs by employing natural tracers to evaluate flux partitions.

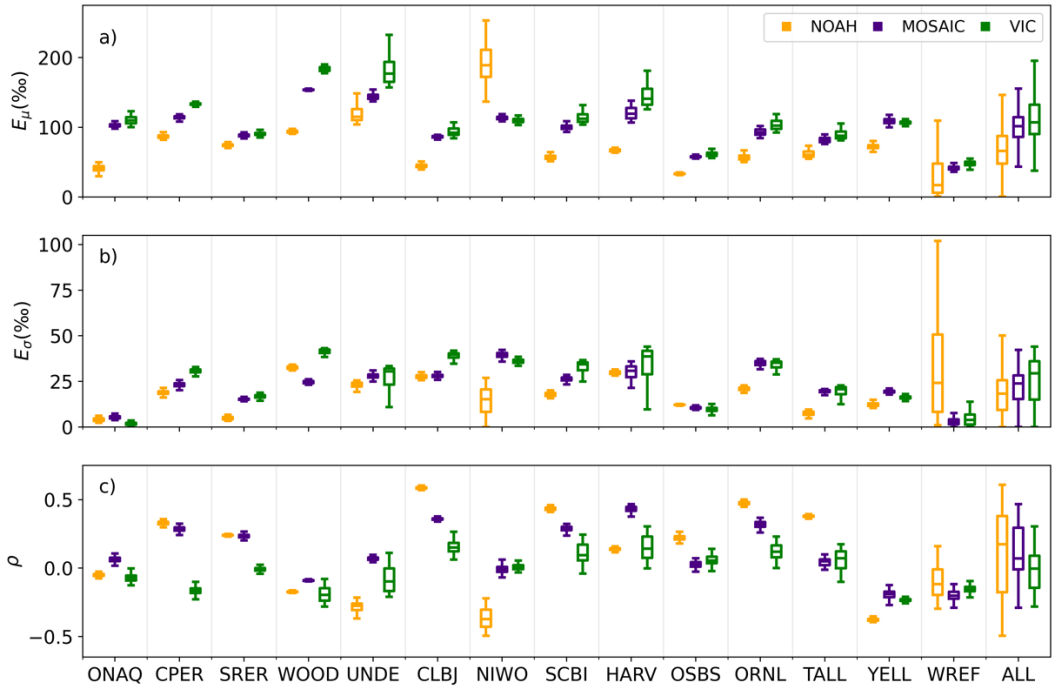

Figure 5.3. Boxplots representing the absolute Error (E) of the a) mean (μ) and b) standard deviation (σ) and the c) cross-correlation (ρ) between the observed and 100 simulated time series from Noah (orange), Mosaic (indigo), and VIC (green) isoMB

estimates of δET. The NEON site order along the x-axis is from least (= 288 mm) to most (= 2225 mm) average annual precipitation. The final column is all sites (ALL).

LSM development should be based on how hydrologic components are partitioned within the model and reflect observed fluxes. We fit a simple linear regression through the average E_μ from the 100 Noah, Mosaic, and VIC isoMB outputs compared to the fraction of transpiration in total ET (*T/ET*) (Figure 5.4a). Most sites have a positive slope, indicating LSMs that assume a larger transpiration flux within the bulk ET flux (*T/ET*) will be less likely to accurately represent expected fluxes and their partitions at a given site. However, at NIWO, a site with high elevation and significant snowpack, we saw an increase in *T/ET* decreased E_μ because Noah assumed almost no transpiration (Figure 5.4a). LSMs with larger evaporative fluxes from the bare soil, canopy interception, or sublimation simulated values are more likely to simulate observed values. Changing the *ET* flux partitions also influenced the standard deviation of the isoMB outputs. LSMs with lower transpiration generally had lower errors in the standard deviation (E_σ; Figure 5.4b). This suggests models assuming a lower transpiration component of the *ET* flux will better represent a site's variance in *ET* through time. Selecting a model with lower *T/ET* is more likely to represent the mean and standard deviation of the δET flux, and consequently better represent a site's transpiration and evaporation rates. LSMs with lower *T/ET* had higher cross-correlation (ρ). By effectively capturing temporal characteristics of the tracer time series (i.e., high ρ), the *ET* flux appropriately partitions transpiration and evaporation components in time and is responsive to seasonality at the site. Some sites experience a stronger seasonal signal than others (e.g., HARV versus WREF, Figure 5.1b,c). If seasonality is the most important feature of modeled *ET* to capture, selecting model physics with high ρ would be most appropriate. Refer to *Supplemental Materials* Tables 5.S2a-c for the slope, y-intercept, R^2, and p-values of the linear regressions.

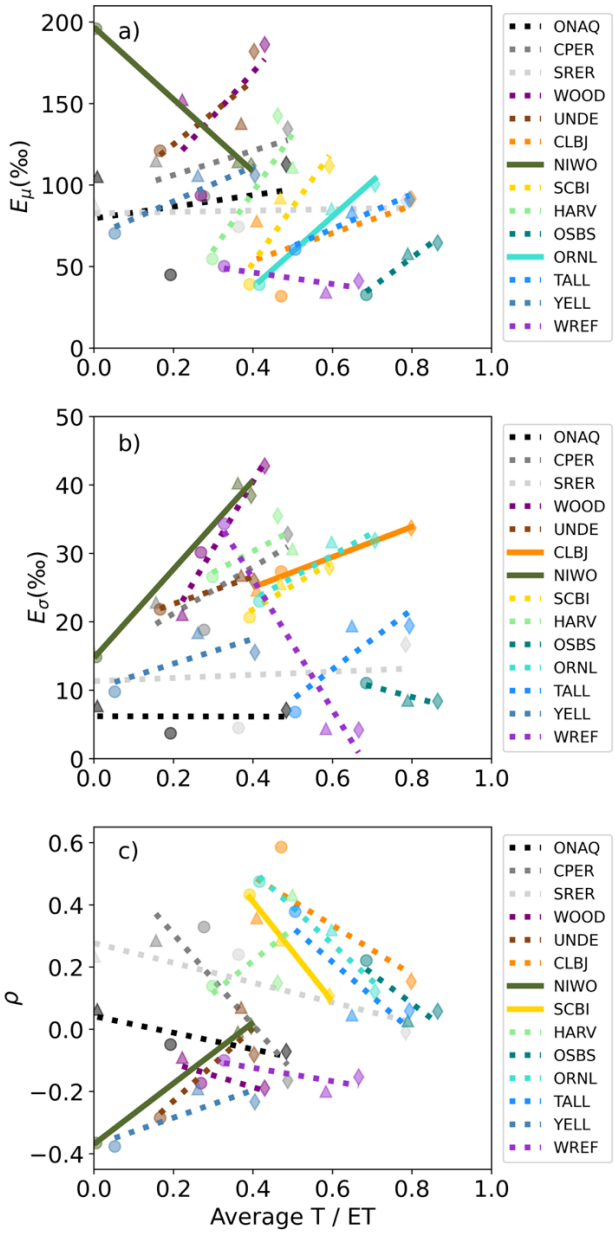

Figure 5.4. Linear regressions representing the average absolute Error (E) of the a) mean (μ) and b) standard deviation (σ) and the c) average cross-correlation (ρ) between the observed and 100 simulated time series from Noah (circles), Mosaic (triangles), and VIC (diamonds) isoMB estimates of δET v. the LSM average T/ET at each NEON site. A linear regression was fit between the three LSM at each site. A solid line was used for a p-value ≤ 0.1 and a dotted line was used for a p-value > 0.1. The NEON site order in the legend is from least (= 288 mm) to most (= 2225 mm) average annual precipitation. Refer to *Supplemental Materials* Table 5.S2a-c for the slope, y-intercept, R^2, and p-values of the linear regressions.

Selecting a model with more or less subsurface drainage (L) relative to total runoff ($L+Q$) has site dependent impacts on estimates of δET (Figure 5.5a,b). At several sites (CPER, SRER, WOOD, YELL), increasing L had little impact on E_μ and at other sites increasing $L/(L+Q)$ beyond 0.80 greatly increased E_μ (Figure 5.5a). When the contribution of subsurface drainage to total runoff was decreased, E_σ was reduced at most sites (Figure 5.5b). Similarly, more overland flow results in less precipitation entering the storage volume, mixing, and contributing to the δET flux. At YELL and SRER, we noticed fewer impacts or large shifts in E_σ across different $L/(L+Q)$ (Figure 5.5b). This suggests model selection based on ET has implications for subsurface flow dynamics and watershed residence times. The cross-correlation (ρ) between the isoMB simulations and observed time series was also compared against $L/(L+Q)$ (Figure 5.5c). At most sites, the LSMs assumed high (> 0.80) $L/(L+Q)$ and subsurface flow clearly plays an integral part in dictating the ET. At each site, it is important to select a LSM which assumes a higher ρ as it relates to capturing seasonal signals in the δET flux.

Future research could move toward LSM development at sites contingent upon minimizing E_μ and E_σ in respect to subsurface drainage or transpiration partitions of water balance components. Additionally, if a multi-model ensemble is applied different weights can be attributed to each model in the averaged based on their E_μ and E_σ.

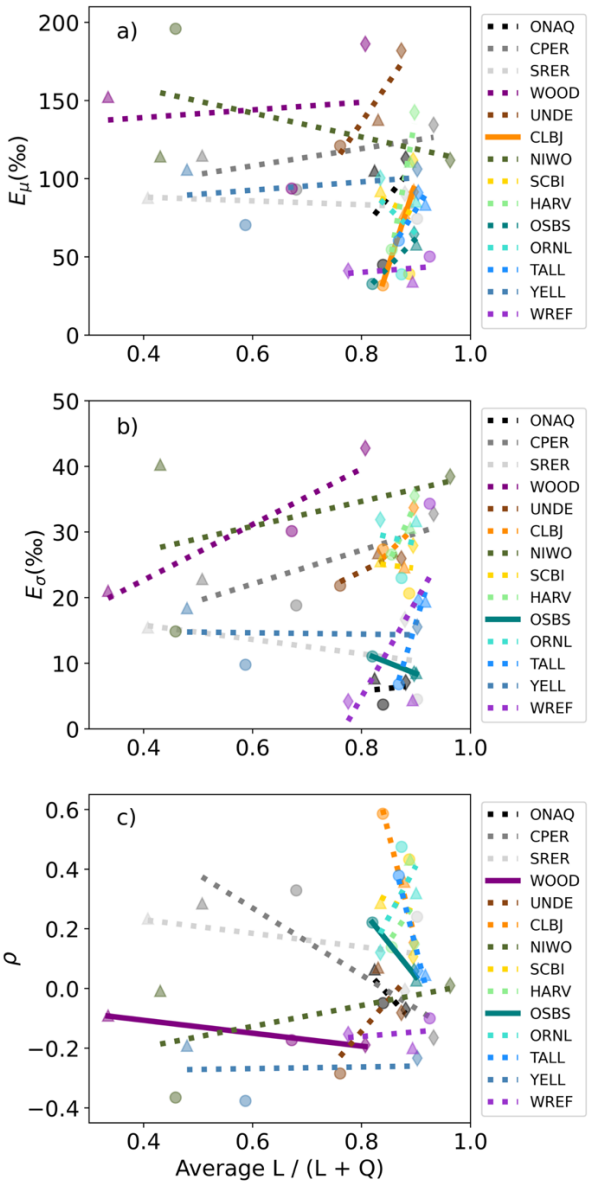

Figure 5.5. Linear regressions representing the average absolute Error (E) of the a) mean (μ) and b) standard deviation (σ) and the c) average cross-correlation (ρ) between the observed and 100 simulated time series from Noah (circles), Mosaic (triangles), and VIC (diamonds) isoMB estimates of δET v. the LSM average L/(L+Q) at each NEON site. A linear regression was fit between the three LSM at each site. A solid line was used for a p-value ≤ 0.1 and a dotted line was used for a p-value > 0.1. The NEON site order in the legend is from least (= 288 mm) to most (= 2225 mm) average annual precipitation. Refer to *Supplemental Materials* Table 5.S3a-c for the slope, y-intercept, R^2, and p-values of the linear regressions.

5.6 Conclusions

An inter-model comparison suggested distinct differences exist amongst observed and simulated δET and this can be associated with disparities in the relative contributions of transpiration and other constituents of evaporation to total *ET*. Our results indicate stable water isotopes as conservative tracers allow for better tracking of the uncertainties associated with inferences drawn from LSM outputs and provide additional validation metrics on which to evaluate model performance. LSM representations of the *ET* flux can greatly impact water and energy balance simulations used in large-scale hydrologic and global climate modeling. We predict our findings can improve the general understanding of land-surface processes influencing the water and carbon cycle from regional to global scales.

5.7 Acknowledgements

The authors acknowledge the support of the United States National Science Foundation (DEB-1802885, DEB-1802880, NSF-1954660). We thank the National Center for Atmospheric Research (NCAR) for allowing us to run our simulations on their high-performance computing system.

5.8 Open Research

The daily datasets and code used in our analysis are available on Hydroshare (Finkenbiner et al., 2021b) and a data descriptor is in review at *Scientific Data*. Observation datasets are available for download directly from the NEON data portal (https://www.neonscience.org/data) with the neonUtilities R package (Lunch and Laney, 2020). NLDAS-2 model forcings and outputs are available for download from NASA databases (https://ldas.gsfc.nasa.gov/nldas/nldas-get-data). Additional materials can be made available upon request.

5.9 References

Abbott et al., (2016), Using multi-tracer inference to move beyond single catchment ecohydrology. *Earth-Sci. Rev.* **160**, 19-42. doi:10.1016/j.earscirev.2016.06.014

Ajami, H. (2021), Geohydrology: Global hydrological cycle. *Encyclopedia of Geology (Second Edition)*, 393-398. doi:10.1016/B978-0-12-409548-9.12387-5

Al-Oqaili, F., Good, S. P., Frost, K., & Higgins, C.W. (2020), Differences in soil evaporation between row and interrow positions in furrowed agricultural fields. *Vadose Zone J.* 19:e20086. doi:10.1002/vzj2.20086

Beven, K. J. (2000), Uniqueness of place and process representations in hydrological modelling. *Hydrol. Earth Syst. Sci*., *4*, 203–213. doi:10.5194/hess-4-203-2000

Bowen, G. J. & Good, S. P. (2015), Incorporating water isotopes in hydrological and water resource investigations. *Wiley Interdiscip. Rev.: Water*, *2*, 107–119. doi:10.1002/wat2.1069

Brooks, J. R., Gibson, J. J., Birks, S. J., Weber, M. H., Rodecap, K. D., & Stoddard, J. L., (2014), Stable isotope estimates of evaporation : inflow and water residence time for lakes across the United States as a tool for national lake water quality assessments. *Limnology and Oceanography*, 59. doi: 10.4319/lo.2014.59.6.2150

Chai, M. Y., Wang, L., Parkes, S. D., Strauss, J., McCabe, M. F., Evans, J. P., & Griffiths, A. D. (2015), Stable water isotope and surface heat flux simulation using ISOLSM: Evaluation against in-situ measurements. *J. of Hydrol.*, 523, 67–78. doi:10.1016/j.jhydrol.2015.01.019

Chen, F., Mitchell, K., Schaake, J., Xue, Y., Pan, H.L., Koren, V., Duan, Q.Y., Ek, M., & Betts, A. (1996**),** Modeling of land surface evaporation by four schemes and comparison with FIFE observations. *J. Geophys. Res. Atmos.*, *101*, 7251–7268. doi:10.1029/95JD02165

Computational and Information Systems Laboratory (2019), Cheyenne: HPE/SGI ICE XA System (NCAR Community Computing). Boulder, CO: National Center for Atmospheric Research. doi:10.5065/D6RX99HX.

Dee, S., Noone, D., Buenning, N., Emile-Geay, J., & Zhou, Y. (2015), SPEEDY-IER: A fast atmospheric GCM with water isotope physics, *J. Geophys. Res. Atmos*., 120, 73– 91, doi:10.1002/2014JD022194

Ek, M., Mitchell, K., Yin, L., Rogers, P., Grunmann, P., Koren, V., Gayno, G., Tarpley, J. (2003), Implementation of Noah land-surface model advances in the NCEP operational mesoscale Eta model. *J. Geophys. Res.*, *108*. doi:10.1029/2002JD003296

Feng, Y., Cui, N., Gong, D., Zhang, Q., & Zhao, L. (2017), Evaluation of random forests and generalized regression neutral networks for daily reference evapotranspiration modelling. *Agricultural Water Management*, *193*, 163-173. doi:10.1016/j.agwat.2017.08.003

Finkenbiner, C. E., Good, S. P., Allen, S. T., Fiorella, R. P., & Bowen, G. J. (2021a), A statistical method for generating temporally downscaled geochemical tracers in precipitation. *J. Hydrometeorol. 22*, 1473-1486. doi:10.1175/JHM-D-20-0142.1

Finkenbiner, C., Li, B., Spencer, L., Fiorella, R., Allen, S., Good, S. P., Bowen, G., & Still, C. (2021b), Datasets of Daily Water and Carbon Stable Isotope Ratios for Precipitation, Evapotranspiration, and Net Ecosystem Exchange Fluxes at NEON Sites, HydroShare, http://www.hydroshare.org/resource/e74edc35d45441579d51286ea01b519f

Fiorella, R. et al. (2021), Calibration Strategies for Detecting Macroscale Patterns in NEON Atmospheric Carbon Isotope Observations. *J. Geophys. Res. Biogeosci. 126*. doi:10.1029/2020JG005862

Franks, S. W., Gineste, P., Beven, K. J., & Merot, P. (1998), On constraining the predictions of a distributed model: The incorporation of fuzzy estimates of saturated areas into the calibration process. *Water Resour. Res*., 34, 787–797. doi:10.1029/97WR03041

Gat, J. R. (2008), The isotopic composition of evaporating waters – review of the historical evolution leading up to the Craig–Gordon model. *Isotopes in Environmental and Health Studies*, *44*(1), 5-9, doi:10.1080/10256010801887067

Ghasemizade, M., Baroni, G., Abbaspour, K., & Schirmer, M. (2017), Combined analysis of time-varying sensitivity and identifiability indices to diagnose the response of a complex environmental model. *Environ. Modell. Softw*., *88*, 22–34. doi:10.1016/j.envsoft.2016.10.011

Good, S. P., Noone, D., & Bowen, G. (2015), Hydrologic connectivity constrains partitioning of global terrestrial water fluxes. *Science*, *349*(6244), 175-177. doi:10.1126/science.aaa5931

Gupta, A., Gerber, E. P., & Lauritzen, P. H. (2020), Numerical impacts on tracer transport: A proposed intercomparison test of atmospheric general circulation models. *Quart. J. Roy. Meteor. Soc. 146*, 3937–3964. doi:10.1002/qj.3881

Guse, B., Pfannerstill, M., Strauch, M., Reusser, D. E., Lüdtke, S., Volk, M., Gupta, H., & Fohrer, N. (2016), On characterizing the temporal dominance patterns of model parameters and processes. *Hydrol. Process.*, *30*, 2255–2270. doi:10.1002/hyp.10764

Herman, J. D., Kollat, J. B., Reed, P. M., & Wagener, T. (2013), From mapstomovies:high-resolution time-varying sensitivity analysis for spatially distributed watershed models. *Hydrol. Earth Syst. Sci.*, *17*, 5109–5125. doi:10.5194/hess-17-5109-2013

Horita, J., Rozanski, K., & Cohen, S. (2008), Isotope effects in the evaporation of water: a status report of the Craig–Gordon model. *Isotopes in Environmental and Health Studies*, *44*(1), 23-49, doi:10.1080/10256010801887174

IAEA, 2021: Global network of isotopes in precipitation. https://www.iaea.org/services/networks/gnip.

Irmak, S. (2008), Evapotranspiration. In: *Encyclopedia of Ecology*. Manuscript No. 270. Sven Erik Jorgensen & Brian D. Fath, (eds). *Encyclopedia of Ecology*, 1st Edition, Elsevier B.V., Oxford. Elsevier. pp. 1432-1439. Journal Series No. 1037.

Jung, M., Reichstein, M., Ciais, P., Seneviratne, S. I., Sheffield, J., Goulden, M. L., Bonan, G., Cescatti, A., Chen, J., & de Jeu, R. (2010), Recent decline in the global land evapotranspiration trend due to limited moisture supply, Nature, 467, 951–954. doi: 10.1038/nature09396

Kanner, L. C., Buenning, N. H., Stott, L. D., Timmermann, A., & Noone, D (2014), The role of soil processes in d18O. *Global Biogeochem. Cycles* **28,** 239–252. doi:10.1002/2013GB004742

Katul, G. & Novick, K. (2009), Evapotranspiration. In: Gene E. Likens, (Editor) *Encyclopedia of Inland Waters*. volume 1, pp. 661-667. Oxford: Elsevier.

Kelleher, C., McGlynn, B., & Wagener, T. (2017), Characterizing and reducing equifinality by constraining a distributed catchment model with regional signatures, local observations, and process understanding, *Hydrol. Earth Syst. Sci*., 21, 3325–3352. doi:10.5194/hess-21-3325-2017

Kelleher, C., Wagener, T., & McGlynn, B. (2015), Model-based analysis of the influence of catchment properties on hydrologic partitioning across five mountain headwater subcatchments, *Water Resour. Res.*, *51*, 4109–4136, doi:10.1002/2014WR016147

Koster, R. & Suarez, M. (1996), *Energy and Water Balance Calculations in the Mosaic LSM*; Technical Report 104606; NASA: Washington, DC, USA.

Koster, R. D. & Suarez, M. J. (1992) Modeling the land surface boundary in climate models as a composite of independent vegetation stands. *J. Geophys. Res. Atmos. 97*, 2697–2715. doi:10.1029/91JD01696

Krause, P., Boyle, D. P., & Bäse, F (2005), Comparison of different efficiency criteria for hydrological model assessment. *Adv. in Geosci.* **5***,* 89-97. doi:10.5194/adgeo-5-89-2005

Kumar, S., Holmes, T., Mocko, D. M., Wang, S., & Peters-Lidard C. (2018), Attribution of Flux Partitioning Variations between Land Surface Models over the Continental U.S. *Remote Sensing*. *10*(5):751. doi:10.3390/rs10050751

Kumar, S. V., Wang, S., Mocko, D. M., Peters-Lidard, C. D., & Xia, Y. (2017), Similarity assessment of land surface model outputs in the North American Land Data Assimilation System. *Water Resour. Res.*, 53, 8941– 8965. doi:10.1002/2017WR020635

Liang, X., Lettenmaier, D., Wood, E., & Burges, S. (1994), A simple hydrologically based model of land surface water and energy fluxes for general circulation models. *J. Geophys. Res. 99*, 14415–14428. doi:10.1029/94JD00483

Long, D., & Singh, V. P. (2012), A modified surface energy balance algorithm for land (M-SEBAL) based on a trapezoidal framework, *Water Resour. Res., 48*, W02528, doi:10.1029/2011WR010607

Lu, X. et al. (2017), Partitioning of evapotranspiration using a stable isotope technique in an arid and high temperature agricultural production system. *Agric. Water Manag.*, *179*, 103-109. doi:10.1016/j.agwat.2016.08.012

Lunch, C. K. & Laney, C. M. (2020), NEON (National Ecological Observatory Network), neonUtilities: Utilities for working with NEON data. R package version 1.3.4. https://github.com/NEONScience/NEON-utilities.

Maxwell, R. M., & Condon, L. E. (2016), Connections between groundwater flow and transpiration partitioning. Science, 353(6297), 377–380. doi:10.1126/science.aaf7891

McGuire, K. J. & McDonnell, J. J. (2006), A review and evaluation of catchment transit time modeling. *J. Hydrol.* **330,** 543–563. doi:10.1016/j.jhydrol.2006.04.020

Miller, J. B., & Tans, P. P. (2003), Calculating isotopic fractionation from atmospheric measurements at various scales. *Tellus*, 55. doi: 10.1034/j.1600-0889.2003.00020.x

Miralles, D. G., Jiménez, C., Jung, M., Michel, D., Ershadi, A., McCabe, M. F., Hirschi, M., Martens, B., Dolman, A. J., Fisher, J. B., Mu, Q., Seneviratne, S. I., Wood, E. F., & Fernández-Prieto, D. (2016), The WACMOS-ET project - Part 2: Evaluation of global terrestrial evaporation data sets. *Hydrol. Earth Syst. Sci*., *20*, 823–842. doi:10.5194/hess-20-823-2016

Moradkhani, H., Hsu, K.-L., Gupta, H., & Sorooshian, S. (2005), Uncertainty assessment of hydrologic model states and parameters: Sequential data assimilation using the particle filter, *Water Resour. Res.*, 41, W05012, doi:10.1029/2004WR003604

Moreau, P., Viaud, V., Parnaudeau, V., Salmon-Monviola, J., & Durand, P. (2013), An approach for global sensitivity analysis of a complex environmental model to spatial inputs and parameters: A case study of an agro-hydrological model. *Environ. Modell. Softw.*, *47*, 74–87, doi:10.1016/j.envsoft.2013.04.006

Muñoz, E., Rivera, D., Vergara, F., Tume, P., & Arumí J. L. (2014), Identifiability analysis: towards constrained equifinality and reduced uncertainty in a conceptual model, *Hydrological Sciences Journal*, 59:9, 1690-1703, doi:10.1080/02626667.2014.892205

NEON (National Ecological Observatory Network), (2021), Bundled data products - eddy covariance (DP4.00200.001). https://data.neonscience.org

NEON (National Ecological Observatory Network), (2021), Stable isotopes in precipitation (DP1.00038.001). https://data.neonscience.org

Noone, D. & Sturm C. (2010), Comprehensive dynamical models of global and regional water isotope distributions. In: West J., Bowen G., Dawson T., Tu K. (eds) Isoscapes. Springer, Dordrecht. doi:10.1007/978-90-481-3354-3_10

Overgaard, J., Rosbjerg, D., & Butts, M. B. (2006), Land-surface modelling in hydrological perspective – a review, *Biogeosciences*, 3, 229–241, doi:10.5194/bg-3-229-2006

Pataki, D. E., Ehleringer, J. R., Flanagan, L. B., Yakir, D., Bowling, D. R., Still, C. J., Buchmann, N., Kaplan, O., & Berry J. A. (2003), The application and interpretation of Keeling plots in terrestrial carbon cycle research. *Global Biogeochem. Cycles*, 17. doi: 10.1029/2001GB001850

Remondi, F., Kircher, J. W., Burlando, P., & Fatichi, S. (2018), Water flux tracking with a distributed hydrologic model to quantify controls on the spatio-temporal variability of transit time distributions. *Water Resour. Res. 54*, 3081–3099. doi: 10.1002/2017WR021689

Renard, B., D. Kavetski, M. Thyer, G. Kuczera, & S. W. Franks (2010), Understanding predictive uncertainty in hydrologic modeling: The challenge of identifying input and structural errors, *Water Resour. Res.*, 46. doi:10.1029/2009WR008328

Soderberg, K., Good, S.P., Wang, L. & Caylor, K. (2012), Stable isotopes of water vapor in the vadose zone: A review of measurement and modeling techniques. *Vadose Zone Journal*, 11: vzj2011.0165. doi:10.2136/vzj2011.0165

Sprenger, M. et al. (2019), The demographics of water: A review of water ages in the critical zone. *Rev. Geophys.* **57**, 800–834. doi:10.1029/2018RG000633

Turnadge, C. & Smerdon , B. D. (2014), A review of methods for modelling environmental tracers in groundwater: Advantages of tracer concentration simulation. *J. Hydrol. 519*, 3674–3689. doi:10.1016/j.jhydrol.2014.10.056

Wagener, T., van Werkhoven, K., Reed, P., & Tang, Y. (2009), Multiobjective sensitivity analysis to understand the information content in streamflow observations for distributed watershed modeling. *Water Resour. Res*., 45, W02501, doi:10.1029/2008WR007347

van Werkhoven, K., Wagener, T., Reed, P., & Tang, Y. (2008), Characterization of watershed model behaviour across a hydroclimatic gradient. *Water Resour. Res., 44*, W01429, doi:10.1029/2007WR006271

Wieser G. et al. (2016), Stable water use efficiency under climate change of three sympatric conifer species at the alpine treeline. *Front. Plant Sci.* **7**, 799. doi:10.3389/fpls.2016.00799

Wild, M. & Liepert, B. (2010), The Earth radiation balance as driver of the global hydrological cycle, *Environ. Res. Lett.*, 5, 025203, doi:10.1088/1748-9326/5/2/025003

Wu, Y. et al. (2018), Stable isotope measurements show increases in corn water use efficiency under deficit irrigation. *Sci Rep, 8*, 14113. doi:10.1038/s41598-018-32368-4

Xia, Y., Mitchell, K., Ek, M., Sheffield, J., Cosgrove, B., Wood, E., Luo, L., Alonge, C., Wei, H., Meng, J., et al. (2012), Continental-scale water and energy flux analysis

and validation for the North American Land Data Assimilation System Project Phase 2 (NLDAS-2), Part 1: Comparison Analysis and Application of Model Products. *J. Geophys. Res. Atmos.,* 117. doi:10.1029/2011JD016048

Zhang, C., Chu, J., & Fu, G. (2013), Sobol's sensitivity analysis for a distributed hydrological model of Yichun River Basin, China. 480, 58–68, doi:10.1016/j.jhydrol.2012.12.005

Zhang, B., Xia, Y., Long, B., Hobbins, M., Zhao, X., Hain, C., Li, Y., & Anderson, M. C. (2020), Evaluation and comparison of multiple evapotranspiration data models over the contiguous United States: Implications for the next phase of NLDAS (NLDAS-Testbed) development. *Agricultural and Forest Meteorology*, 280, 107810. doi: 10.1016/j.agrformet.2019.107810

5.10 Supplemental Materials

Table 5.S1. Characteristics for the 14 NEON sites including the official site name and location, latitude, longitude, mean annual precipitation, mean elevation, mean annual temperature, and mean canopy height.

Site ID	Site Name/ Location	Latitude (°)	Longitude (°)	Mean Annual Precipitation (mm)	Mean Elevation (m)	Mean Annual Temperature (C)	Mean Canopy Height (m)
ONAQ	Tooele County, UT	40.178	-112.452	288	1662	9	1.2
CPER	Central Plains Experimental Range, CO	40.816	-104.746	344	1654	8.6	0.4
SRER	Santa Rita Experimental Range, AZ	31.911	-110.835	346	997	19.3	2
WOOD	Woodworth, WI	47.128	-99.241	494	591	4.9	1
UNDE	University of Notre Dame Environmental Research Center, MI/WI	46.234	-89.537	802	521	4.3	24
CLBJ	LBJ National Grassland, TX	33.401	-97.570	926	272	17.5	13
NIWO	Niwot Ridge Mountain Research Station, CO	40.054	-105.582	1005	3490	0.3	0.2
SCBI	Smithsonian Conservation	38.893	-78.140	1126	352	11.6	35

	Biology Institute, VA						
HARV	Harvard Forest, MA	42.537	-72.173	1199	348	7.4	26
OSBS	Ordway-Swisher Biological Station, FL	29.689	-81.993	1302	46	20.9	23
ORNL	Oak Ridge National Laboratory, TN	35.964	-84.283	1340	344	14.4	28
TALL	Talladega National Forest, AL	32.950	-87.393	1383	166	17.2	25
YELL	Yellowstone National Park, MT	44.953	-110.539	2133	2133	3.4	14
WREF	Wind River Experimental Forest, WA	45.820	-121.952	2225	351	9.2	50

Table 5.S2a. The slope, y-intercept, R^2, and p-value from the linear regression calculated between the average error in the mean (E_μ) from Noah, Mosaic, and VIC isoMB δET values and the average transpiration (T) divided by total evapotranspiration (ET) from each LSM. Underlined p-values are represented as solid lines in Figure 5.4a.

	Average E_μ v. Average T / ET			
Site	**Slope**	**y-intercept**	**R^2**	**p-value**
ONAQ	35.70	79.55	0.05	0.85
CPER	74.67	91.23	0.37	0.59
SRER	4.30	82.61	0.04	0.87
WOOD	268.80	61.73	0.39	0.57
UNDE	195.23	85.95	0.63	0.42
CLBJ	84.01	20.15	0.31	0.62
NIWO	-220.99	196.86	1.00	<u>0.03</u>
SCBI	343.43	-85.16	0.86	0.25
HARV	357.54	-47.30	0.74	0.34
OSBS	182.00	-90.07	0.95	0.15
ORNL	216.70	-49.25	0.98	<u>0.09</u>
TALL	106.48	9.23	0.92	0.18
YELL	106.52	68.70	0.84	0.26
WREF	-35.22	60.42	0.60	0.43

Table 5.S2b. The slope, y-intercept, R^2, and p-value from the linear regression calculated between the average error in the mean (E_σ) from Noah, Mosaic, and VIC isoMB δET values and the average transpiration (T) divided by total evapotranspiration (ET) from each LSM. Underlined p-values are represented as solid lines in Figure 5.4b.

	Average E_σ v. Average T / ET			
Site	**Slope**	**y-intercept**	**R^2**	**p-value**
ONAQ	-0.11	6.20	0.00	0.99
CPER	34.01	14.40	0.63	0.42
SRER	2.30	11.33	0.02	0.91
WOOD	98.13	1.23	0.96	0.13
UNDE	19.89	18.63	0.92	0.18
CLBJ	22.08	16.22	0.98	0.09
NIWO	64.81	14.73	0.98	0.09
SCBI	34.73	7.92	0.90	0.21
HARV	30.66	18.04	0.54	0.47
OSBS	-15.33	21.28	0.85	0.25
ORNL	32.37	10.29	0.88	0.23
TALL	43.70	-13.16	0.75	0.33
YELL	18.13	10.25	0.54	0.48
WREF	-95.57	64.48	0.95	0.15

Table 5.S2c. The slope, y-intercept, R^2, and p-value from the linear regression calculated from the average cross-correlations (ρ) of outputs from Noah, Mosaic, and VIC isoMB δET values and the average transpiration (T) divided by total evapotranspiration (ET) from each LSM. Underlined p-values are represented as solid lines in Figure 5.4c.

	Average Cross-correlation (ρ) v. Average T / ET			
Site	**Slope**	**y-intercept**	**R^2**	**p-value**
ONAQ	-0.27	0.04	0.77	0.32
CPER	-1.47	0.60	0.81	0.29
SRER	-0.32	0.28	0.77	0.32
WOOD	-0.38	-0.03	0.61	0.43
UNDE	1.17	-0.46	0.71	0.36
CLBJ	-0.79	0.81	0.58	0.45
NIWO	0.98	-0.37	1.00	0.02
SCBI	-1.61	1.05	1.00	0.04
HARV	1.03	-0.19	0.44	0.54
OSBS	-0.97	0.85	0.70	0.37
ORNL	-1.18	0.98	0.96	0.14
TALL	-1.11	0.88	0.71	0.36
YELL	0.44	-0.37	0.65	0.40
WREF	-0.21	-0.04	0.57	0.45

Table 5.S3a. The slope, y-intercept, R^2, and p-value from the linear regression calculated between the average error in the mean (E_μ) from Noah, Mosaic, and VIC isoMB δET values and the average subsurface drainage (L) divided by total runoff ($L + Q$) from each LSM. Underlined p-values are represented as solid lines in Figure 5.5a.

	Average E_μ v. Average L / (L + Q)			
Site	**Slope**	**y-intercept**	**R^2**	**p-value**
ONAQ	440.55	-285.90	0.12	0.77
CPER	54.93	75.31	0.32	0.62
SRER	-12.12	93.10	0.16	0.74
WOOD	24.48	129.36	0.02	0.92
UNDE	512.43	-273.83	0.85	0.25
CLBJ	1071.79	-866.22	0.99	0.05
NIWO	-76.78	188.11	0.23	0.68
SCBI	-173.44	232.29	0.02	0.90
HARV	1967.01	-1629.10	0.97	0.12
OSBS	359.26	-261.60	0.94	0.16
ORNL	-328.54	360.55	0.11	0.78
TALL	550.26	-414.85	0.77	0.32
YELL	26.46	76.82	0.08	0.82
WREF	27.93	17.77	0.08	0.82

Table 5.S3b. The slope, y-intercept, R^2, and p-value from the linear regression calculated between the average error in the mean (E_σ) from Noah, Mosaic, and VIC isoMB δET values and the average subsurface drainage (L) divided by total runoff ($L + Q$) from each LSM. Underlined p-values are represented as solid lines in Figure 5.5b.

	Average E_σ v. Average L / (L + Q)			
Site	**Slope**	**y-intercept**	**R^2**	**p-value**
ONAQ	8.22	-0.80	0.01	0.93
CPER	25.71	6.65	0.58	0.45
SRER	-10.92	20.18	0.21	0.70
WOOD	42.37	5.72	0.89	0.21
UNDE	40.15	-8.12	0.74	0.34
CLBJ	81.43	-42.35	0.26	0.66
NIWO	18.96	19.49	0.16	0.74
SCBI	-9.83	33.29	0.01	0.94
HARV	185.37	-132.30	0.85	0.25
OSBS	-32.82	37.95	0.99	<u>0.05</u>
ORNL	-19.84	46.10	0.02	0.92
TALL	276.82	-232.90	0.93	0.17
YELL	-1.03	15.26	0.00	0.97
WREF	146.63	-112.47	0.45	0.53

Table 5.S3c. The slope, y-intercept, R^2, and p-value from the linear regression calculated from the cross-correlations (ρ) of outputs from Noah, Mosaic, and VIC isoMB δET values and the average subsurface drainage (L) divided by total runoff ($L + Q$) from each LSM. Underlined p-values are represented as solid lines in Figure 5.5c.

	Average Cross-correlation (ρ) v. Average L / (L + Q)			
Site	**Slope**	**y-intercept**	**R^2**	**p-value**
ONAQ	-1.99	1.67	0.66	0.40
CPER	-1.12	0.94	0.77	0.32
SRER	-0.23	0.32	0.20	0.71
WOOD	-0.22	-0.02	0.98	0.08
UNDE	2.13	-1.85	0.46	0.52
CLBJ	-7.29	6.71	0.97	0.12
NIWO	0.35	-0.34	0.25	0.67
SCBI	-0.83	1.00	0.03	0.89
HARV	2.75	-2.18	0.13	0.76
OSBS	-2.27	2.09	0.99	0.07
ORNL	3.47	-2.71	0.41	0.55
TALL	-7.25	6.66	0.95	0.14
YELL	0.03	-0.29	0.00	0.96
WREF	0.16	-0.29	0.06	0.84

Chapter 6. Conclusion

Changes to the hydrologic cycle will impact water resources for billions of people worldwide and we need appropriate models to represent past, present, and current drivers of the hydrologic cycle. The results and conclusions presented in this dissertation provide new insights and applications of stable water isotopes as natural tracers when evaluating hydrologic modeling frameworks and investigating pressing research questions in hydrology. Natural tracers were effectively applied to various hydrologic modeling applications and provided additional points of comparison between observed and modeled environmental pools and fluxes.

I developed a new statistical downscaling method which can generate synthetic geochemical time series at higher temporal resolutions, when fine-scale *in-situ* data is not available (see Chapter 2). The generated high-resolution time series maintain informative site-specific correlation structures between covariates and the geochemical tracer and retain the statistical properties of underlying processes (e.g., *d*-excess, amount effects). Daily tracer concentrations downscaled from a biweekly series had average (+/- standard deviation) absolute errors of 1.69‰ (1.61‰) for δ^2H and 0.23‰ (0.24‰) for $\delta^{18}O$ relative to observations. The results suggest coarsely sampled precipitation tracers can be accurately downscaled to daily values. The method is sufficiently general and was applied to investigate subsurface transport processing using a state-of-the-art soil physics model and evaluate LSM estimates and partitions of evapotranspiration at ecosystem scales.

I provided the first comprehensive evaluation of transport in the subsurface under different soil porosity heterogeneities across a range of fine to coarse soils and wet, dry, and seasonally varying climate conditions (see Chapter 3). This work contributes to an ongoing debate in the scientific community regarding the degree of mixing within the critical zone. Field measurements of isotope ratios indicate varying degrees of separation between pools of water that supply streams and vegetation. The exact physical mechanisms behind ecohydrologic separation are unknown, but local conditions such as soil heterogeneities likely influence the extent of mixing and separation of subsurface

water pools. I demonstrated that separations can be explained by heterogeneous mixing in soils alone and how these separations are expected to vary with local ecohydrologic characteristics. Thus, any models aiming to realistically represent transport processes, especially those characterized through tracer observations, must represent the heterogeneity of soil pores within a soil column and the exchanges among them. This analysis demonstrated that the coexistence of both finer and coarser pores within a single soil profile by itself can manifest in real, complex tracer phenomena that have otherwise been attributed to myriad ecophysiological and hydrological processes.

In Chapter 4, I presented a new data product with generated daily records of a) δ^2H and $\delta^{18}O$ in precipitation fluxes (F_P) at 16 National Ecological Observatory Network (NEON) core sites and 16 NEON relocatable sites, b) δ^2H and $\delta^{18}O$ of ET fluxes (F_{ET}) at 19 NEON core sites and 2 NEON relocatable sites, and c) $\delta^{13}C$ of NEE fluxes (F_{NEE}) at 19 NEON core sites and 28 NEON relocatable sites. Statistically downscaled precipitation datasets were generated to be consistent with the estimated covariance between isotope ratios and precipitation amounts at daily time scales. Isotope ratios in ET and NEE fluxes were estimated using a mixing model approach with NEON tower measurements and site-specific isotope calibrations. These products form a unique daily flux isotope dataset spanning across diverse ecosystems over a multi-year span created using consistent instrumentation and methodology. This dataset is open-source and available on Hydroshare (Finkenbiner et al., 2021b). Future work can modify the to fit a user's specific application or as additional NEON data records become available in the future.

I investigated the uncertainty in total ET for three LSMs in the NLDAS-2 configuration using observation datasets of precipitation and ET at 14 sites across the United States from the NEON (see Chapter 5). Accurate quantification of the terrestrial evapotranspiration flux (ET) into its partitions of interception, plant transpiration, and soil evaporation is critical for understanding the water and carbon cycle and associated ecohydrologic processes. Recent studies have noted significant disparities exist amongst modeled estimates of the relative contributions of interception, plant transpiration, and soil evaporation to the total ET. The statistically downscaled stable water isotope ratios

corresponded with daily NLDAS forcings and were used as conservative tracers within a mass balance model built from LSM outputs. The mass balance model (isoMB) simulated stable water isotope concentrations (δ) for each ET partition, subsurface drainage, surface runoff, and storage. Simulated δET was directly compared to daily δET observations, which were calibrated from NEON tower measurements of atmospheric water vapor. An inter-model comparison suggested distinct differences exist amongst simulated δET and this can be associated with disparities in the relative contributions of interception, plant transpiration, and soil evaporation to the total ET. LSMs that assume a larger transpiration flux within the bulk ET flux (T/ET) are less likely to accurately represent expected fluxes and their partitions. A LSM which effectively captures the temporal characteristics of the tracer time series better partitions the ET flux into its transpiration and evaporation components in time and has high temporal correlation structures between observed and simulated time series. The results indicate conservative tracers allow for better tracking of the uncertainties associated with inferences drawn from LSM outputs and provide additional validation metrics on which to evaluate model performance. LSM representations of the ET can greatly impact water and energy balance simulations used in large-scale hydrologic and global climate modeling. These findings can improve the general understanding of land-surface processes influencing the water and carbon cycle from regional to global scales.

Bibliography

Abbott, B. W., V. Baranov, C. Mendoza-Lera, M. Nikolakopoulou, A. Harjung, T. Kolbe, M. N. Balasubramanian, T. N. Vaessen, F. Ciocca, A. Campeau, M. B. Wallin, P. Romeijn, M. Antonelli, J. Gonçalves, T. Datry, A. M. Laverman, J. de Dreuzy, D. M. Hannah, S. Krause, C. Oldham, and G. Pinay, 2016: Using multi-tracer inference to move beyond single catchment ecohydrology. *Earth-Sci. Rev.*, **160**, 19-42, https://doi.org/10.1016/j.earscirev.2016.06.014.

Ajami, H. (2021), Geohydrology: Global hydrological cycle. *Encyclopedia of Geology (Second Edition)*, 393-398. doi:10.1016/B978-0-12-409548-9.12387-5

Allen, S. T. and Kirchner, J. W. Potential effects of cryogenic extraction biases on inferences drawn from xylem water deuterium isotope ratios: case studies using stable isotopes to infer plant water sources. *Hydrol Earth Syst Sci Discuss* [preprint] https://doi.org/10.5194/hess-2020-683, in review (2021).

Al-Oqaili, F., Good, S. P., Frost, K., & Higgins, C.W. Differences in soil evaporation between row and interrow positions in furrowed agricultural fields. *Vadose Zone J.* 19:e20086 (2020).

Aggarwal, P. K., O. A. Alduchov, K. O. Froehlich, L. J. Araguas-Araguas, N. C. Sturchio, and N. Kurita, 2012: Stable isotopes in global precipitation: a unified interpretation based on atmospheric moisture residence time. *Geophys. Res. Lett.,* **39***,* 1-6, https://doi.org/10.1029/2012GL051937.

Aggarwal, P. K., U. Romatschke, L. Araguas-Araguas, D. Belachew, F. J. Longstaffe, P. Berg, C. Schumacher, and A. Funk, 2016: Proportions of convective and stratiform precipitation revealed in water isotope ratios. *Nat. Geosci.*, **9**, 624-629, https://doi.org/10.1038/ngeo2739.

Allen, S. T., Jasechko, S., Berghuijs, W. R., Welker, J. M., Goldsmith, G. R., and Kirchner, J. W., 2019: Global sinusoidal seasonality in precipitation isotopes, *Hydrol. Earth Syst. Sci.*, **23**, 3423–3436, https://doi.org/10.5194/hess-23-3423-2019.

Allen, S. T., Kirchner, J. W., & Goldsmith, G. R., 2018. Predicting spatial patterns in precipitation isotope (δ2H and δ18O) seasonality using sinusoidal isoscapes. *Geophys. Res.*, **45**, 4859–4868, https://doi.org/10.1029/2018GL077458.

Bailey, A., E. Posmentier, and X. Feng, 2018: Patterns of Evaporation and Precipitation Drive Global Isotopic Changes in Atmospheric Moisture. *Geophy. Res. Lett.*, **45**, 7093-7101, https://doi.org/10.1029/2018GL078254.

Barbeta, A., Gimeno, T.E., Clavé, L., et al. An explanation for the isotopic offset between soil and stem water in a temperate tree species. *New Phytol* 227, 766-779 (2020). https://doi.org/10.1111/nph.16564

Bárdossy, A. and G. G. S. Pegram, 2009: Copula based multisite model for daily precipitation simulation. *Hydrol. Earth Syst. Sci.,* **13***,* 2299-2314.

Benetti, M., G. Reverdin, C. Pierre, L. Merlivat, C. Risi, H. C. Steen-Larsen, and F. Vimeux, 2014: Deuterium excess in marine water vapor: Dependency on relative humidity and surface wind speed during evaporation. *J. Geophys. Res-Atmos.*, **119**, 583-593, https://doi.org/10.1002/2013JD020535.

Berghuijs, W.R. and Kirchner, J.W. The relationship between contrasting ages of groundwater and streamflow. *Geophys Res Lett* 44, 8925-8935 (2017). https://doi.org/10.1002/2017GL074962.

Berry, Z.C., Evaristo, J., Moore, G., et al. The two water worlds hypothesis: Addressing multiple working hypotheses and proposing a way forward. *Ecohydrology* 11, e1843 (2018). https://doi.org/10.1002/eco.1843

Beven, K. J. (2000), Uniqueness of place and process representations in hydrological modelling. *Hydrol. Earth Syst. Sci*., *4*, 203–213. doi:10.5194/hess-4-203-2000

Brady, E., Stevenson, S., Bailey, D., Liu, Z., Noone, D., Nusbaumer, J., Otto-Bliesner, B. L., Tabor, C., Tomas, R., Wong, T., et al., 2019: The Connected Isotopic Water Cycle in the Community Earth System Model Version 1. *J. Adv. Model. Earth Syst.*, **11**, 2547– 2566, https://doi.org/10.1029/2019MS001663.

Brooks, J. R., Barnard, H., Coulombe, R. et al. Ecohydrologic separation of water between trees and streams in a Mediterranean climate. *Nature Geosci* 3, 100–104 (2010). https://doi.org/10.1038/ngeo722

Brooks, J. R., J. J. Gibson, S. J. Birks, M. H. Weber, K. D. Rodecap, and J. L. Stoddard, 2014: Stable isotope estimates of evaporation: inflow and water residence time for lakes across the United States as a tool for national lake water quality assessments. *Limnol. Oceanogr.,* **59**, 2150-2165, https://doi.org/10.4319/lo.2014.59.6.2150.

Bordoy, R. and P. Burlando, 2013: Stochastic downscaling of climate model precipitation outputs in orographically complex regions: 2. Downscaling methodology. *Water Resour. Res.,* **50***,* 562-579, https://doi.org/10.1002/wrcr.20443.

Bowen, G. J., Z. Cai, R. P. Fiorella, and A. L. Putman, 2019: Isotopes in the water cycle: Regional- to global-scale patterns and applications. *Annu. Rev. Earth Planet Sci.*, **47**, 453-479, https://doi.org/10.1146/annurev-earth-053018-060220.

Bowen, G. J. and S. P. Good, 2015: Incorporating water isotopes in hydrological and water resource investigations. *WIREs. Water*, **2**, *2*, 107-119. https://doi.org/10.1002/wat2.1069.

Cain, M.R., Ward, A.S., and Hrachowitz, M. Ecohydrologic separation alters interpreted hydrologic stores and fluxes in a headwater mountain catchment. *Hydrol Process* 33, 2658-2675 (2019). https://doi.org/10.1002/hyp.13518

Celle-Jeanton, H. Y. Travi, and B. Blavoux, 2001: Isotopic typology of the precipitation in the Western Mediterranean region at three different time scales. *Geophys. Res. Lett.*, **28**, *7*, 1215-1218, https://doi.org/10.1029/2000GL012407.

Chai, M. Y., Wang, L., Parkes, S. D., Strauss, J., McCabe, M. F., Evans, J. P., & Griffiths, A. D. (2015), Stable water isotope and surface heat flux simulation using ISOLSM: Evaluation against in-situ measurements. *J. of Hydrol.*, 523, 67–78. doi:10.1016/j.jhydrol.2015.01.019

Chen, F., Mitchell, K., Schaake, J., Xue, Y., Pan, H.L., Koren, V., Duan, Q.Y., Ek, M., & Betts, A. (1996**),** Modeling of land surface evaporation by four schemes and comparison with FIFE observations. *J. Geophys. Res. Atmos.*, *101*, 7251–7268. doi:10.1029/95JD02165

Chen, Y., Helliker, B.R., Tang, X., Li, F., Zhou, Y., and Song, X. Stem water cryogenic extraction biases estimation in deuterium isotope composition of plant source water. *Proc Natl Acad Sci USA* 52, 33345-33350 (2020). https://doi.org/10.1073/pnas.2014422117

Clow, D. W., M. A. Mast, and J. O. Sickman, 2018: Linking transit times to catchment sensitivity to atmospheric deposition of acidity and nitrogen in mountains of the western United States, *Hydrol. Process*, **32**, *16*, 2456–2470, https://doi.org/10.1002/hyp.13183.

Computational and Information Systems Laboratory (2019), Cheyenne: HPE/SGI ICE XA System (NCAR Community Computing). Boulder, CO: National Center for Atmospheric Research. doi:10.5065/D6RX99HX.

Cong, R. and M. Brady, 2012: The interdependence between rainfall and temperature: copula analysis. *The Scientific World Journal,* **2012**, 1-11, https://doi.org/10.1100/2012/405675.

Conroy, J. L., Noone, D., Cobb, K. M., Moerman, J. W., and Konecky, B. L. (2016), Paired stable isotopologues in precipitation and vapor: A case study of

the amount effect within western tropical Pacific storms, *J. Geophys. Res. Atmos.*, **121**, 3290– 3303, https://doi.org/10.1002/2015JD023844.

Coulibaly, P., Y. B. Dibike, and F. Anctil, 2005: Downscaling precipitation and temperature with temporal neutral networks. *J. Hydrometeor.,* **6***,* 483-496, https://doi.org/10.1175/JHM409.1.

Craig, H., 1961: Isotopic variations in meteoric waters. *Science*, **133**, 1702-1703.

Craig, H. and L. I. Gordon, 1965: Deuterium and oxygen-18 variations in the ocean and the marine atmosphere. *In E. Tongiorgi, ed*, Proceedings of a Conference on Stable Isotopes in Oceanographic Studies and Paleotemperatures, Spoleto, Italy, pp 9-130.

Daly, C. and McKee, W.A. Meteorological data from benchmark stations at the Andrews Experimental Forest, 1957 to present ver 36. Environmental Data Initiative (2019). https://doi.org/10.6073/pasta/c021a2ebf1f91adf0ba3b5e53189c84f (Accessed 2021-04-21).

Dansgaard, W., 1964: Stable isotopes in precipitation. *Tellus*, **16**, 436–468, https://doi.org/10.1111/j.2153-3490.1964.tb00181.x.

Dee, S., Noone, D., Buenning, N., Emile-Geay, J., & Zhou, Y. (2015), SPEEDY-IER: A fast atmospheric GCM with water isotope physics, *J. Geophys. Res. Atmos*., 120, 73– 91, doi:10.1002/2014JD022194

D'Onofrio, D. 2014: Stochastic rainfall downscaling of climate models. *J. Hydrometeor.,***15**, 830-843, https://doi.org/10.1175/JHM-D-13-096.1.

Dubbert, M., Caldeira, M.C., Dubbert, D. and Werner, C. A pool-weighted perspective on the two-water-worlds hypothesis. *New Phytol* 222, 1271-1283 (2019). https://doi.org/10.1111/nph.15670

Dutton, A., B. H. Wilkinson, J. M. Welker, G. J. Bowen, and K. C. Lohmann, 2005: Spatial distribution and seasonal variation in 18O/16O of modern precipitation and river water across the conterminous USA, *Hydrol. Process.*, **19**, *20*, 4121–4146, https://doi.org/10.1002/hyp.5876.

Ebtehaj, A. M., and E. Foufoula-Georgiou, 2013: On variational downscaling, fusion, and assimilation of hydrometeorological states: A unified framework via regularization. *Water Resour. Res.*, **49**, 5944– 5963, https://doi.org/10.1002/wrcr.20424.

Ellsworth, P.Z., and Williams, D.G. Hydrogen isotope fractionation during water uptake by woody xerophytes. *Plant Soil* 291, 93-107 (2007). https://doi.org/10.1007/s11104-006-9177-1

Evaristo, J., Jasechko, S. and McDonnell, J. Global separation of plant transpiration from groundwater and streamflow. *Nature* 525, 91-94 (2015). https://doi.org/10.1038/nature14983

Ek, M., Mitchell, K., Yin, L., Rogers, P., Grunmann, P., Koren, V., Gayno, G., Tarpley, J. (2003), Implementation of Noah land-surface model advances in the NCEP operational mesoscale Eta model. *J. Geophys. Res.*, *108*. doi:10.1029/2002JD003296

Feng, Y., Cui, N., Gong, D., Zhang, Q., & Zhao, L. (2017), Evaluation of random forests and generalized regression neutral networks for daily reference evapotranspiration modelling. *Agricultural Water Management*, *193*, 163-173. doi:10.1016/j.agwat.2017.08.003

Finkenbiner, C.E., Good, S.P., Allen, S.T., Fiorella, R.P., and Bowen, G.J. A statistical method for generating temporally downscaled geochemical tracers in precipitation. *J Hydrometerol* 22, 1473-1486 (2021). https://doi.org/10.1175/JHM-D-20-0142.1

Finkenbiner, C. et al. (2021). Datasets of Daily Water and Carbon Stable Isotope Ratios for Precipitation, Evapotranspiration, and Net Ecosystem Exchange Fluxes at NEON Sites, HydroShare, http://www.hydroshare.org/resource/e74edc35d45441579d51286ea01b519f

Fiorella, R. et al. (2021), Calibration Strategies for Detecting Macroscale Patterns in NEON Atmospheric Carbon Isotope Observations. *J. Geophys. Res. Biogeosci. 126*. doi:10.1029/2020JG005862

Fekete, B. M., J. J. Gibson, P. Aggarwal, C. J. Vörösmarty, 2006: Application of isotopic tracers in continental scale hydrological modeling. *J. Hydrol.*, **330**, *3-4*, 444-456, https://doi.org/10.1016/j.jhydrol.2006.04.029.

Feng, X., A. M. Faiia, and E. S. Posmentier, 2009: Seasonality of isotopes in precipitation: A global perspective. *J. Geophys. Res-Atmos*, **114**, *D8*, https://doi.org/10.1029/2008JD011279.

Franks, S. W., Gineste, P., Beven, K. J., & Merot, P. (1998), On constraining the predictions of a distributed model: The incorporation of fuzzy estimates of saturated areas into the calibration process. *Water Resour. Res*., 34, 787–797. doi:10.1029/97WR03041

v. Freyberg, J., S. T. Allen, S. Seeger, M. Weiler, and J. W. Kirchner, 2018: Sensitivity of young water fractions to hydroclimatic forcing and landscape properties across 22

Swiss catchments, *Hydrol. Earth Syst. Sci.*, 22, *7*, 3841–3861, https://doi.org/10.5194/hess-22-3841-2018.

Fröehlich K., J. J. Gibson, and P. K. Aggarwal, 2002: Deuterium excess in precipitation and its climatological significance. Study of environmental change using isotope techniques. *C&S Papers Series*, **13**, 54-65. International Atomic Energy Agency: Vienna, Austria.

Gallart, F., M. Valiente, P. Llorens, C. Cayuela, M. Sprenger, and J. Latron, 2020: Investigating young water fractions in a small Mediterranean mountain catchment: both precipitation forcing and sampling frequency matter. *Hydrol. Processes*, https://doi.org/10.1002/hyp.13806.

Gao, C., Y. Xu, Q. Zhu, Z. Bai, and L. Liu, 2018: Stochastic generation of daily rainfall events: a single-site rainfall model with copula-based joint simulation of rainfall characteristics and classification and simulation of rainfall patterns. *J. Hydrol,* **564**, 41-58, https://doi.org/10.1016/j.jhydrol.2018.06.073.

Gat, J. R. (2008), The isotopic composition of evaporating waters – review of the historical evolution leading up to the Craig–Gordon model. *Isotopes in Environmental and Health Studies*, *44*(1), 5-9, doi:10.1080/10256010801887067

Gat, J. R., 1996: Oxygen and hydrogen isotopes in the hydrologic cycle. *Annu. Rev. Earth Planet Sci.*, **24**, 225-262, https://doi.org/10.1146/annurev.earth.24.1.225.

van Genuchten, M.T. A closed-form equation for predicting the hydraulic conductivity of unsaturated soils. *Soil Science Society of America Journal* 44, 892-898 (1980). https://doi.org/10.2136/sssaj1980.03615995004400050002x

Gibson, J. J., T. W. D. Edwards, S. J. Birks, N. A. St Amour, W. M. Buhay, P. McEachern, B. B. Wolfe, and D. L. Peters, 2005: Progress in isotope tracer hydrology in Canada. *Hydrol. Process.*, **19***, 1*, 303-327, https://doi.org/10.1002/hyp.5766.

Goncu, S., and E. Albek, 2016: Statistical downscaling of meteorological time series and climatic projections in a watershed in Turkey. Theoretical and Applied Climatology, **126,** 1-2, https://link.gale.com/apps/doc/A470736525/AONE?u=s8405248&sid=AONE&xid=e894de9e.

Ghasemizade, M., Baroni, G., Abbaspour, K., & Schirmer, M. (2017), Combined analysis of time-varying sensitivity and identifiability indices to diagnose the response of a complex environmental model. *Environ. Modell. Softw*., *88*, 22–34. doi:10.1016/j.envsoft.2016.10.011

Good S. P., D. V. Mallia, J. C. Lin, and G. J. Bowen, 2014: Stable isotope analysis of precipitation samples obtained via crowdsourcing reveals the spatiotemporal evolution of superstorm sandy. PLOS ONE **9**, *3*, e91117, https://doi.org/10.1371/journal.pone.0091117.

Good, S. P., Noone, D., & Bowen, G. Hydrologic connectivity constrains partitioning of global terrestrial water fluxes. *Science* **349**, 175–177 (2015).

Good, S. P., Soderberg, K., Wang, L., & Caylor, K. K. Uncertainties in the assessment of the isotopic composition of surface fluxes: A direct comparison of techniques using laser-based water vapor isotope analyzers. *J. Geophys. Res. Atmos.* **177** (2012).

Good, S. P., D. Noone, and G. Bowen, 2015: Hydrologic connectivity constrains partitioning of global terrestrial water fluxes. *Science,* **349***,* 175-177, https://doi.org/10.1126/science.aaa5931.

Groh, J., Stumpp, C., Lücke, A., Pütz, T., Vanderborght, J., and Vereecken, H. Inverse estimation of soil hydraulic and transport parameters of layered soils from water stable isotope and lysimeter data. *Vadose Zone J* 17, 170168 (2018). https://doi.org/10.2136/vzj2017.09.0168

Gupta, A., E. P. Gerber, and P. H. Lauritzen, 2020: Numerical impacts on tracer transport: A proposed intercomparison test of Atmospheric General Circulation Models. *Q. J. R. Meteorol. Soc.*, **146**, 3937– 3964, https://doi.org/10.1002/qj.3881.

Guse, B., Pfannerstill, M., Strauch, M., Reusser, D. E., Lüdtke, S., Volk, M., Gupta, H., & Fohrer, N. (2016), On characterizing the temporal dominance patterns of model parameters and processes. *Hydrol. Process.*, *30*, 2255–2270. doi:10.1002/hyp.10764

Gyasi-Agyei, Y., 2011: Copula-based daily rainfall disaggregation model. *Water Resour. Res.,* **47***,* W07535, https://doi.org/10.1029/2011WR010519.

Halder, J., S. Terzer, L. I. Wassenaar, L. J. Araguás-Araguás, and P. K. Aggarwal, 2015: The Global Network of Isotopes in Rivers (GNIR): integration of water isotopes in watershed observation and riverine research. *Hydrol. Earth Syst. Sci.*, **19**, *8*, 3419–3431, https://doi.org/10.5194/hess-19-3419-2015.

Haslauer, C. P., P. Guthke, A. Bádossy, and E. A. Sudicky, 2012: Effects of non-gaussian copula-based hydraulic conductivity fields on macrodispersion. *Water Resour. Res.,* **48***,* 1-18, https://doi.org/10.1029/2011WR011425.

Herman, J. D., Kollat, J. B., Reed, P. M., & Wagener, T. (2013), From mapstomovies:high-resolution time-varying sensitivity analysis for spatially distributed watershed models. *Hydrol. Earth Syst. Sci.*, *17*, 5109–5125. doi:10.5194/hess-17-5109-2013

Hoffmann, G., J. Jouzel and V. Masson, 2000: Stable water isotopes in atmospheric general circulation models. *Hydrol. Processes,* **14**, 1385-1406, https://doi.org/10.1002/1099-1085(20000615)14:8<1385::AID-HYP989>3.0.CO2-1.

Horita, J., Rozanski, K., & Cohen, S. (2008), Isotope effects in the evaporation of water: a status report of the Craig–Gordon model. *Isotopes in Environmental and Health Studies*, *44*(1), 23-49, doi:10.1080/10256010801887174

Hu, H., Dominguez, F., Kumar, P., McDonnell, J., and Gochis, D. A numerical water tracer model for understanding event-scale hydrometeorological phenomena. *J Hydrometeorol* 19, 947-967 (2018). https://doi.org/10.1175/JHM-D-17-0202.1

Huang, J., J. Zhang, Z. Zhang, S. Sun and J. Yao, 2012: Simulation of extreme precipitation indices in the Yangtze River basin by using statistical downscaling method (SDSM). *Theor. Appl. Climatol.* **108**, 325–343, https://doi.org/10.1007/s00704-011-0536-3.

Huntington, T. G., Weiskel, P. K., Wolock, D. M., & McCabe, G. J. (2018). A new indicator framework for quantifying the intensity of the terrestrial water cycle. *Journal of Hydrology*, *559*, 361-372. doi:10.1016/j.jhydrol.2018.02.048

IAEA/WMO (2020). Global Network of Isotopes in Precipitation. The GNIP Database. Accessible at: http://www.iaea.org/water.

Ingraham, N. L., 1998: Isotopic variations in precipitation. In C. Kendall & J. J. McDonnell (Eds.), Isotope Tracers in Catchment Hydrology (pp. 87–118). Amsterdam: Elsevier Science, https://doi.org/10.1016/B978-0-444-81546-0.50010-0.

IPCC, 2021: Climate Change 2021: The Physical Science Basis. Contribution of Working Group I to the Sixth Assessment Report of the Intergovernmental Panel on Climate Change [Masson-Delmotte, V., P. Zhai, A. Pirani, S.L. Connors, C. Péan, S. Berger, N. Caud, Y. Chen, L. Goldfarb, M.I. Gomis, M. Huang, K. Leitzell, E. Lonnoy, J.B.R. Matthews, T.K. Maycock, T. Waterfield, O. Yelekçi, R. Yu, and B. Zhou (eds.)]. Cambridge University Press. In Press.

Irmak, S. (2008), Evapotranspiration. In: *Encyclopedia of Ecology*. Manuscript No. 270. Sven Erik Jorgensen & Brian D. Fath, (eds). *Encyclopedia of Ecology*, 1st Edition, Elsevier B.V., Oxford. Elsevier. pp. 1432-1439. Journal Series No. 1037.

Jacobs, S. R., E. Timbe, B. Weeser, M. C. Rufino, K. Butterbach-Bahl, and L. Breuer, 2018: Assessment of hydrological pathways in East African montane catchments under different land use. *Hydrol. Earth Syst. Sci.*, **22**, 4981-5000, https://doi.org/10.5194/hess-22-4981-2018.

Jasechko, S. and R. Taylor, 2015: Intensive rainfall recharges tropical groundwaters. *Environ. Res. Lett.,* **10***,* https://doi.org/10.1088/1748-9326/10/12/124015.

Jasechko, S., J. W. Kirchner, J. M. Welker, and J. J. McDonnell, 2016: Substantial proportion of global streamflow less than three months old. *Nat. Geosci.*, **9**, *2*, 126–129, https://doi.org/10.1038/ngeo2636.

Jung, M., Reichstein, M., Ciais, P., Seneviratne, S. I., Sheffield, J., Goulden, M. L., Bonan, G., Cescatti, A., Chen, J., & de Jeu, R. (2010), Recent decline in the global land evapotranspiration trend due to limited moisture supply, Nature, 467, 951–954. doi: 10.1038/nature09396

Kanner, L. C., N. H. Buenning, L. D. Stott, A. Timmermann, and D. Noone, 2014: The role of soil processes in $\delta^{18}O$ terrestrial climate proxies. *Global Biogeochem. Cycles,* **28**, 239-252, https://doi.org/10.1002/2013GB004742.

Katul, G. & Novick, K. (2009), Evapotranspiration. In: Gene E. Likens, (Editor) *Encyclopedia of Inland Waters*. volume 1, pp. 661-667. Oxford: Elsevier.

Kelleher, C., McGlynn, B., & Wagener, T. (2017), Characterizing and reducing equifinality by constraining a distributed catchment model with regional signatures, local observations, and process understanding, *Hydrol. Earth Syst. Sci*., 21, 3325–3352. doi:10.5194/hess-21-3325-2017

Kelleher, C., Wagener, T., & McGlynn, B. (2015), Model-based analysis of the influence of catchment properties on hydrologic partitioning across five mountain headwater subcatchments, *Water Resour. Res.*, *51*, 4109–4136, doi:10.1002/2014WR016147

Kendall, C. and J. J. McDonnell, 2012: *Isotope tracers in catchment hydrology*. Elsevier, 870pp.

Khedun, C. P., A. K. Mishra, V. P. Singh and J. R. Giardino, 2014: A copula-based precipitation forecasting model: investigating the interdecadal modulation of ENSO's impacts on monthly precipitation. *Water Resour. Res.,* **50***,* 580-600, https://doi.org/10.1002/2013WR013763.

Kirchner, J. W., 2016a: Aggregation in environmental systems—Part 1: Seasonal tracer cycles quantify young water fractions, but not mean transit times, in spatially heterogeneous catchments. *Hydrol. Earth Syst. Sci.*, 20, *1*, 279–297, https://doi.org/10.5194/hess-20-279-2016.

Kirchner, J. W., 2016b: Aggregation in environmental systems—Part 2: Catchment mean transit times and young water fractions under hydrologic nonstationarity. *Hydrol. Earth Syst. Sci.*, **20**, *1*, 299–328, https://doi.org/10.5194/hess-20-299-2016.

Knighton, J., Kuppel, S., Smith, A., et al. Using isotopes to incorporate tree water storage and mixing dynamics into a distributed ecohydrologic modelling framework. *Ecohydrol* 13, e2201 (2020). https://doi.org/10.1002/eco.2201

Konecky, B. L., D. C. Noone, and K. M. Cobb, 2019: The influence of competing hydroclimate processes on stable isotope ratios in tropical rainfall. *Geophys. Res. Lett.*, **46**, 1622-1633, https://doi.org/10.1029/2018GL080188.

Koster, R. & Suarez, M. (1996), *Energy and Water Balance Calculations in the Mosaic LSM*; Technical Report 104606; NASA: Washington, DC, USA.

Koster, R. D. & Suarez, M. J. (1992) Modeling the land surface boundary in climate models as a composite of independent vegetation stands. *J. Geophys. Res. Atmos. 97*, 2697–2715. doi:10.1029/91JD01696

Krause, P., D. P. Boyle, and F. Bäse, 2005: Comparison of different efficiency criteria for hydrological model assessment. *Adv. in Geosci.,* **5***,* 89-97, https://doi.org/1680-7359/adgeo/2005-5-89.

Kuhn, G., S. Khan, A. R. Ganguly, and M. L. Branstetter, 2007: Geospatial-temporal dependence among weekly precipitation extremes with applications to observations and climate model simulations in South America. *Adv. Water Resour.,* **30***,* 2401-2423, https://doi.org/10.1016/j.advwatres.2007.05.006.

Kumar, S., Holmes, T., Mocko, D. M., Wang, S., & Peters-Lidard C. (2018), Attribution of Flux Partitioning Variations between Land Surface Models over the Continental U.S. *Remote Sensing*. *10*(5):751. doi:10.3390/rs10050751

Kumar, S. V., Wang, S., Mocko, D. M., Peters-Lidard, C. D., & Xia, Y. (2017), Similarity assessment of land surface model outputs in the North American Land Data Assimilation System. *Water Resour. Res.*, 53, 8941– 8965. doi:10.1002/2017WR020635

Laux, P., S. Vogl, W. Qiu, H. R. Knoche, and H. Kunstmann, 2011: Copula-based statistical refinement of precipitation in RCM simulations over complex terrain. *Hydrol. Earth Sys. Sci.,* **15***,* 2401-2419, https://doi.org/10.5194/hess-15-2401-2011.

Laux, P., S. Wagner, A. Wagner, J. Jacobeit, A. Bárdossy, and H. Kunstmann, 2009: Modelling daily precipitation features in the Volta Basin of West Africa. *International Journal of Climatology,* **29***,* 937-954, https://doi.org/10.1002/joc.1852.

Lee, J. E. and I. Fung, 2008: "Amount effect" of water isotopes and quantitative analysis of post-condensation processes. *Hydrol. Process*., **22**, 1-8, https://doi.org/10.1002/hyp.6637.

Lee, R. and S. Weintraub. NEON User Guide to Stable Isotopes in Precipitation (NEON.DPI.00038) Version B. NEON (National Ecological Observatory Network). (2021).

Liang, X., Lettenmaier, D., Wood, E., & Burges, S. (1994), A simple hydrologically based model of land surface water and energy fluxes for general circulation models. *J. Geophys. Res. 99*, 14415–14428. doi:10.1029/94JD00483

Long, D., & Singh, V. P. (2012), A modified surface energy balance algorithm for land (M-SEBAL) based on a trapezoidal framework, *Water Resour. Res., 48*, W02528, doi:10.1029/2011WR010607

Lu, X. et al. Partitioning of evapotranspiration using a stable isotope technique in an arid and high temperature agricultural production system. *Agric. Water Manag.* **179** 103-109 (2017).

Lunch, C. K. & Laney, C. M. NEON (National Ecological Observatory Network). neonUtilities: Utilities for working with NEON data. R package version 1.3.4. https://github.com/NEONScience/NEON-utilities (2020).

Lutz, S. R., R. Krieg, C. Müller, M. Zink, K. Knöller, L. Samaniego, and R. Merz, 2018: Spatial patterns of water age: Using young water fractions to improve the characterization of transit times in contrasting catchments. *Water Resour. Res.*, **54**, *7*, 4767–4784, https://doi.org/10.1029/2017WR022216.

Małoszewski, P., Maciejewski, S., Stumpp, C., Stichler, W., Trimborn, P., and Klotz, D. Modelling of water flow through typical Bavarian soils: 2. Environmental deuterium transport. *Hydrol Sci J* 51, 298-313 (2006). https://doi.org/10.1623/hysj.51.2.298

Maxwell, R. M., & Condon, L. E. (2016), Connections between groundwater flow and transpiration partitioning. Science, 353(6297), 377–380. doi:10.1126/science.aaf7891

McDonnell, J.J. The two water worlds hypothesis: ecohydrological separation of water between streams and trees? *WIREs Water* 1, 323-329 (2014). https://doi.org/10.1002/wat2.1027

McGuire, K. J. and J. J. McDonnell, 2006: A review and evaluation of catchment transit time modeling. *J. Hydrol.,* **330***,* 543-563, https://doi.org/10.1016/j.jhydrol.2006.04.020.

McGuire, K. J. & McDonnell, J. J. (2006), A review and evaluation of catchment transit time modeling. *J. Hydrol.* **330,** 543–563. doi:10.1016/j.jhydrol.2006.04.020

Miller, J. B., & Tans, P. P. (2003), Calculating isotopic fractionation from atmospheric measurements at various scales. *Tellus*, 55. doi: 10.1034/j.1600-0889.2003.00020.x

Mitchell, D., AchutaRao, K., Allen, M., Bethke, I., Beyerle, U., Ciavarella, A., Forster, P. M., Fuglestvedt, J., Gillett, N., Haustein, K., Ingram, W., Iversen, T., Kharin, V., Klingaman, N., Massey, N., Fischer, E., Schleussner, C.-F., Scinocca, J., Seland, Ø., Shiogama, H., Shuckburgh, E., Sparrow, S., Stone, D., Uhe, P., Wallom, D., Wehner, M., and Zaaboul, R. (2017). Half a degree additional warming, prognosis and projected impacts (HAPPI): background and experimental design, Geosci. Model Dev., 10, 571–583, https://doi.org/10.5194/gmd-10-571-2017.

Miralles, D. G., Jiménez, C., Jung, M., Michel, D., Ershadi, A., McCabe, M. F., Hirschi, M., Martens, B., Dolman, A. J., Fisher, J. B., Mu, Q., Seneviratne, S. I., Wood, E. F., & Fernández-Prieto, D. (2016), The WACMOS-ET project - Part 2: Evaluation of global terrestrial evaporation data sets. *Hydrol. Earth Syst. Sci*., *20*, 823–842. doi:10.5194/hess-20-823-2016

Moerman, J. W., K. M. Cobb, J. F., Adkins, H. Sodemann, B. Clark, and A. A. Tuen, 2013: Diurnal to interannual rainfall $\delta^{18}O$ variations in northern Borneo driven by regional hydrology. *Earth Planet. Sci. Lett.,* **369-370***,* 108-109, https://doi.org/10.1016/j.epsl.2013.03.014.

Moore, M., P. N. Blossey, A. Muhlbauer, and Z. Kuang, 2016: Microphysical controls on the isotopic composition of wintertime orographic precipitation. *J. Geophys. Res. Atmos.*, **121**, 7235- 7253, https://doi.org/10.1002/2015JD023763.

Moore, M., Kuang, Z., and Blossey, P. N., 2014: A moisture budget perspective of the amount effect, *Geophys. Res. Lett*., **41**, 1329– 1335, https://doi.org/10.1002/2013GL058302.

Moradkhani, H., Hsu, K.-L., Gupta, H., & Sorooshian, S. (2005), Uncertainty assessment of hydrologic model states and parameters: Sequential data assimilation using the particle filter, *Water Resour. Res.*, 41, W05012, doi:10.1029/2004WR003604

Moreau, P., Viaud, V., Parnaudeau, V., Salmon-Monviola, J., & Durand, P. (2013), An approach for global sensitivity analysis of a complex environmental model to spatial inputs and parameters: A case study of an agro-hydrological model. *Environ. Modell. Softw.*, *47*, 74–87, doi:10.1016/j.envsoft.2013.04.006

Mueller, M.H., Alaoui, A., Kuells, C. et al. Tracking water pathways in steep hillslopes by $\delta^{18}O$ depth profiles of soil water. *J Hydrol* 519, 340-352 (2014). https://doi.org/10.1016/j.jhydrol.2014.07.031

Muñoz, E., Rivera, D., Vergara, F., Tume, P., & Arumí J. L. (2014), Identifiability analysis: towards constrained equifinality and reduced uncertainty in a conceptual model, *Hydrological Sciences Journal*, 59:9, 1690-1703, doi:10.1080/02626667.2014.892205

Noone, D. & Sturm C. (2010), Comprehensive dynamical models of global and regional water isotope distributions. In: West J., Bowen G., Dawson T., Tu K. (eds) Isoscapes. Springer, Dordrecht. doi:10.1007/978-90-481-3354-3_10

Nusbaumer, J., T. E. Wong, C. Bardeen, and D. Noone, 2017: Evaluating hydrological processes in the Community Atmosphere Model Version 5 (CAM5) using stable isotope ratios of water. *J. Adv. Model Earth Sy.*, **9**, *2*, 949-977, https://doi.org/10.1002/2016MS000839.

Orbe, C., D. Rind, J. Jonas, L. Nazarenko, G. Faluvegi, L. T. Murray, D. T. Shindell, K. Tsigaridis, T. Zhou, M. Kelley, and G. A. Schmidt, 2020: GISS Model E2.2: A climate model optimized for the middle atmosphere—2. Validation of large-scale transport and evaluation of climate response. *J. Geophys. Res. Atmos*., **125**, https://doi-org.ezproxy.proxy.library.oregonstate.edu/10.1029/2020JD033151.

Overgaard, J., Rosbjerg, D., & Butts, M. B. (2006), Land-surface modelling in hydrological perspective – a review, *Biogeosciences*, 3, 229–241, doi:10.5194/bg-3-229-2006

Pataki, D. E., Ehleringer, J. R., Flanagan, L. B., Yakir, D., Bowling, D. R., Still, C. J., Buchmann, N., Kaplan, O., & Berry J. A. (2003), The application and

interpretation of Keeling plots in terrestrial carbon cycle research. *Global Biogeochem. Cycles*, 17. doi: 10.1029/2001GB001850

Pfahl, S. and H. Sodemann, 2014: What controls deuterium excess in global precipitation?. *Clim. Past*, **10**, 771–781, https://doi.org/10.5194/cp-10-771-2014.

Poduje, A. C. C. and U. Haberlandt, 2017: Short time step continuous rainfall modeling and simulation of extreme events. *J. Hydrol.,* **552***,* 182-197, https://doi.org/10.1016/j.jhydrol.2017.06.036.

Radolinski, J., Pangle, L., Klaus, J., and Stewart, R.D. Testing the 'two water worlds' hypothesis under variable preferential flow conditions. *Hydrol Process* 35, e14252 (2021). https://doi.org/10.1002/hyp.14252

Remondi, F., J. W. Kircher, P. Burlando, and S. Fatichi, 2018: Water flux tracking with a distributed hydrologic model to quantify controls on the spatio-temporal variability of transit time distributions. *Water Resour. Res.*, **54**, *4*, 3081-3099, https://doi.org/10.1002/2017WR021689.

Renard, B., D. Kavetski, M. Thyer, G. Kuczera, & S. W. Franks (2010), Understanding predictive uncertainty in hydrologic modeling: The challenge of identifying input and structural errors, *Water Resour. Res.*, 46. doi:10.1029/2009WR008328

Risi, C., D. Noone, J. Worden, C. Frankenberg, G. Stiller, M. Kiefer, B. Funke, K. Walker, P. Bernath, M. Schneider, D. Wunch, V. Sherlock, N. Deutscher, D. Griffith, P. O. Wennberg, K. Strong, D. Smale, E. Mahieu, S. Barthlott, F. Hase, O. García, J. Notholt, T. Warneke, G. Toon, D. Sayres, S. Bony, J. Lee, D. Brown, R. Uemura, C. Sturm, 2012: Process-evaluation of tropospheric humidity simulated by general circulation models using water vapor isotopic observations: 2. Using isotopic diagnostics to understand the mid and upper tropospheric moist bias in the tropics and subtropics, *J. Geophys. Res.*, **117**, *D05304*, https://doi.org/10.1029/2011JD016623.

Risi, C., S. Bony, S., and F. Vimeux, 2008: Influence of convective processes on the isotopic composition (δ18O and δD) of precipitation and water vapor in the tropics: 2. Physical interpretation of the amount effect. *J. Geophys. Res.*, **113**, D19306, https://doi.org/10.1029/2008JD009943.

Rodriguez, N. B., McGuire, K. J., & Klaus, J. Time-varying storage–Water age relationships in a catchment with a Mediterranean climate. *Water Resour. Res.* 54, 3988–4008 (2018). https://doi.org/10.1029/2017WR021964

Rosa, D., Lamarque, J. F., and Collins, W. D. 2012: Global transport of passive tracers in conventional and superparameterized climate models: Evaluation of multi-scale methods, *J. Adv. Model. Earth Syst.*, **4**, https://doi.org/10.1029/2012MS000206.

Rozanski, K., Araguás-Araguás, L. and Gonfiantini, R. 1993: Isotopic Patterns in Modern Global Precipitation. *In Climate Change in Continental Isotopic Records* (eds P.K. Swart, K.C. Lohmann, J. Mckenzie and S. Savin). https://doi.org/10.1029/GM078p0001.

Schölzel, C. and P. Friederichs, 2008: Multivariate non-normally distributed random variables in climate research- introduction to the copula approach. *Nonlinear Processes in Geophysics,* **15***,* 761-772. https://doi.org/10.5194/npg-15-761-2008.

Schneider, M. and F. Ramos, 2014: Transductive learning for multi-task copula processes. *Technical Report*, 1-8, http://www-personal.usyd.edu.au/~framos/Publications_files/TransductiveCopulas.pdf.

Sklar, A., 1959: Fonctions de répartition à n dimensions et leurs marges. *Publ. Inst. Stat. Univ. Paris,* **8**, 229–231.

Šimünek, J., Šejna, M., Saito, H., Sakai, M., and van Genuchten, M.Th. The HYDRUS-1D software package for simulating the one-dimensional movement of water, heat, and multiple solutes in variably-saturated media – version 4.17, HYDRUS software series 1. Department of Environmental Sciences, University of California Riverside, Riverside, CA, 2013, pp. 308 pp.

So, B., J. Kim, H. Kwon, and C. H. R. Lima, 2017: Stochastic extreme downscaling model for an assessment of changes in rainfall intensity-duration-frequency curves over South Korea using multiple regional climate models. *J. Hydrol.,* **553**, 321-337, https://doi.org/10.1016/j.hydrol.2017.07.061.

Soderberg, K., S. P. Good, L. Wang, and K. Caylor, 2012: Stable isotopes of water vapor in the vadose zone: a review of measurement and modeling techniques. *Vadose Zone J*, https://doi.org/10.2136/vzj2011.0165.

Song, C., G. Wang, G. Liu, T. Mao, X. Sun, and X. Chen, 2016: Stable isotope variations of precipitation and streamflow reveal the young water fraction of a permafrost watershed. *Hydrol. Processes*, **31**, *4*, 935–947, doi:10.1002/hyp.11077.

Sprenger, M., and Allen, S. T. Commentary: What ecohydrologic separation is and where we can go with it. *Water Resour Res* 56, e2020WR027238 (2020). https://doi.org/10.1029/2020WR027238

Sprenger, M., Leistert, H., Gimbel, K., and Weiler, M. Illuminating hydrological processes at the soil-vegetation-atmosphere interface with water stable isotopes. *Rev Geophys* 54, 674– 704 (2016). https://doi.org/10.1002/2015RG000515

Sprenger, M., Llorens, P., Cayuela, C., Gallart, F., and Latron, J. Mechanisms of consistently disjunct soil water pools over (pore) space and time, *Hydrol Earth Syst Sci* 23, 2751–2762 (2019). https://doi.org/10.5194/hess-23-2751-2019

Sprenger, M., Seeger, S., Blume, T., and Weiler, M. Travel times in the vadose zone: Variability in space and time. *Water Resour Res* 52, 5727-5754 (2016). https://doi.org/10.1002/2015WR018077

Sprenger, M., C. Stumpp, M. Weiler, W. Aeschbach, S. T. Allen, P. Benettin, M. Dubbert, A. Hartmann, M. Hrachowitz, J. W. Kirchner, J. J. McDonnell, N. Orlowski, D. Penna, S. Pfahl, M. Rinderer, N. Rodriquez, M. Schmidt, and C. Werner, 2019: The demographics of water: A review of water ages in the critical zone. *Rev. of Geophysics*, **57**, 800-834, https://doi.org/10.1029/2018RG000633.

Sprenger, M., Tetzlaff, D., Buttle, J., et al. Measuring and modeling stable isotopes of mobile and bulk soil water. *Vadose Zone J* 17,170149 (2018). https://doi.org/10.2136/vzj2017.08.0149

Sprenger, M., Tetzlaff, D., and Soulsby, C. Soil water stable isotopes reveal evaporation dynamics at the soil–plant–atmosphere interface of the critical zone. *Hydrol Earth Syst Sci* 21, 3839–3858 (2017). https://doi.org/10.5194/hess-21-3839-2017

Sprenger, M., Volkmann, T.H.M., Blume, T., and Weiler, M. Estimating flow and transport parameters in the unsaturated zone with pore water stable isotopes. *Hydrol Earth Syst Sci* 19, 2617–2635 (2015). https://doi.org/10.5194/hess-19-2617-2015

Steen-Larsen, H. C., C. Risi, M. Werner, K. Yoshimura, and V. Masson-Delmotte, 2017: Evaluating the skills of isotope-enabled general circulation models against in situ atmospheric water vapor isotope observations, *J. Geophys. Res. Atmos.*, **122**, 246–263, https://doi.org/10.1002/2016JD025443.

Stumpp, C. and Hendry, M.J. Spatial and temporal dynamics of water flow and solute transport in a heterogeneous glacial till: The application of high-resolution profiles of $\delta^{18}O$ and $\delta^{2}H$ in pore waters. *J Hydrol* 438-439, 203-214 (2012). https://doi.org/10.1016/j.jhydrol.2012.03.024

Stumpp, C., J. Klaus, and W. Stichler, 2014: Analysis of long-term stable isotopic composition in German precipitation. *J. Hydrol.,* **517**, 351-361, https://doi.org/10.1016/j.jhydrol.2014.05.034.

Stumpp, C. and Maloszewski, P. Quantification of preferential flow and flow heterogeneities in an unsaturated soil planted with different crops using the environmental isotope $\delta^{18}O$. *J Hydrol* 394, 407-415 (2010). https://doi.org/10.1016/j.jhydrol.2010.09.014

Stumpp, C., Nützmann, G., Maciejewski, S., and Maloszewski, P. A comparative modeling study of a dual tracer experiment in a large lysimeter under atmospheric conditions. *J Hydrol* 375, 566-577 (2009). https://doi.org/10.1016/j.jhydrol.2009.07.010

Stumpp, C., Stichler, W., Kandolf, M., and Šimůnek, J. Effects of land cover and fertilization method on water flow and solute transport in five lysimeters: A long-term study using stable water isotopes. *Vadose Zone J* 11, vzj2011.0075 (2012). https://doi.org/10.2136/vzj2011.0075

Tharammal, T., Bala, G., and Noone, D., 2017: Impact of deep convection on the isotopic amount effect in tropical precipitation, *J. Geophys. Res. Atmos.*, **122**, 1505– 1523, http://dx.doi.org/10.1002/2016JD025555.

Turnadge, C. and B. D. Smerdon, 2014: A review of methods for modelling environmental tracers in groundwater: Advantages of tracer concentration simulation. *J. Hydrol.*, **519**, http://dx.doi.org/10.1016/j.jhydrol.2014.10.056.

Vachon, R. W., J. W. C. White, E. Gutmann, and J. M. Welker, 2007: Amount-weighted annual isotopic (δ18O) values are affected by the seasonality of precipitation: A sensitivity study. *Geophys. Res. Lett.*, **34**, *21*, L21707, doi:10.1029/2007GL030547.

Vargas, A.I., Schaffer, B., Yuhong, L., and Sternberg, L.D.S.L. Testing plant use of mobile vs immobile soil water sources using stable isotope experiments. *New Phytol* 215, 582-594 (2017). https://doi.org/10.1111/nph.14616. Epub 2017 May 30. PMID: 28556977

Wagener, T., van Werkhoven, K., Reed, P., & Tang, Y. (2009), Multiobjective sensitivity analysis to understand the information content in streamflow observations for distributed watershed modeling. *Water Resour. Res*., 45, W02501, doi:10.1029/2008WR007347

Wehr, R., & Saleska, S. R. An improved isotopic method for partitioning net ecosystem-atmosphere CO2 exchange. *Agric For Meteorol.* **214**, 515– 531 (2015).

van Werkhoven, K., Wagener, T., Reed, P., & Tang, Y. (2008), Characterization of watershed model behaviour across a hydroclimatic gradient. *Water Resour. Res., 44*, W01429, doi:10.1029/2007WR006271

West, J. B., G. J. Bowen, T. E. Dawson, and K. P. Tu, 2010: *Isoscapes: Understanding movement, pattern, and process on Earth through isotope mapping*. Springer, 487pp.

Wiederhold, J. G., 2015: Metal stable isotope signatures as tracers in environmental geochemistry. *Environ. Sci. Technol.*, **49**, 2606-2624, https://doi.org/10.1021/es504683e.

Wieser G. et al. (2016), Stable water use efficiency under climate change of three sympatric conifer species at the alpine treeline. *Front. Plant Sci.* **7**, 799. doi:10.3389/fpls.2016.00799

Wild, M. & Liepert, B. (2010), The Earth radiation balance as driver of the global hydrological cycle, *Environ. Res. Lett.*, 5, 025203, doi:10.1088/1748-9326/5/2/025003

Wilkinson, B. H. and L. C. Ivany, 2002: Paleoclimatic inference from stable isotope profiles of accretionary biogenic hardparts – a quantitative approach to the evaluation of incomplete data, *Palaeogeogr. Palaeoclimatol. Palaeoecol.*, **185**, *1*, 95–114, https://doi.org/10.1016/S0031-0182(02)00279-1.

Wong, T. E., J. Nusbaumer, and D. C. Noone, 2017: Evaluation of modeled land-atmosphere exchanges with a comprehensive water isotope fractionation scheme in version 4 of the Community Land Model. *J. Adv. Model Earth Sy.*, **9**, *2*, 978-1001, https://doi.org/10.1002/2016MS000842.

Wu, Y. et al. (2018), Stable isotope measurements show increases in corn water use efficiency under deficit irrigation. *Sci Rep, 8*, 14113. doi:10.1038/s41598-018-32368-4

Xia, Y., Mitchell, K., Ek, M., Sheffield, J., Cosgrove, B., Wood, E., Luo, L., Alonge, C., Wei, H., Meng, J., et al. (2012), Continental-scale water and energy flux analysis and validation for the North American Land Data Assimilation System Project Phase 2 (NLDAS-2), Part 1: Comparison Analysis and Application of Model Products. *J. Geophys. Res. Atmos.,* 117. doi:10.1029/2011JD016048

Xiao, W., Wei, Z., & Wen, X. Evapotranspiration partitioning at the ecosystem scale using the stable isotope method—A review. *Agric For Meteorol.* **263**, 346-361 (2018).

Yang, W., A. Bárdossy, and H. J. Caspary, 2010: Downscaling daily precipitation time series using a combined circulation- and regression-based approach. *Theor. Appl. Climatol*, **102**, 439-454, https://doi.org/10.1007/s00704-010-0272-0.

Zhang, C., Chu, J., & Fu, G. (2013), Sobol's sensitivity analysis for a distributed hydrological model of Yichun River Basin, China. 480, 58–68, doi:10.1016/j.jhydrol.2012.12.005

Zhang, B., Xia, Y., Long, B., Hobbins, M., Zhao, X., Hain, C., Li, Y., & Anderson, M. C. (2020), Evaluation and comparison of multiple evapotranspiration data models over the contiguous United States: Implications for the next phase of NLDAS (NLDAS-Testbed) development. *Agricultural and Forest Meteorology*, 280, 107810. doi: 10.1016/j.agrformet.2019.107810

Zhou, T., Simunek, J., and Braund I Adapting HYDRUS-1D to simulate the transport of soil water isotopes with evaporation fractionation. *Environ Model Softw* 143, 105118 (2021). https://doi.org/10.1016/j.envsoft.2021.105118

Zobitz, J. M., Keener, J.P., Schnyder, H., & Bowling, D. R. Sensitivity analysis and quantification of uncertainty for isotopic mixing relationships in carbon cycle research. *Agric For Meteorol.* **136** ,56-75 (2006).